UNIVERSITÀ
DEGLI STUDI
DI TRIESTE

UNIVERSITÀ DEGLI STUDI DI TRIESTE

XXXVIII CICLO DEL DOTTORATO DI RICERCA IN
FISICA

SPECTRAL PHASE-CONTRAST X-RAY IMAGING: METHODS AND DEVELOPMENT WITH SYNCHROTRON AND LABORATORY SOURCES

Settore scientifico-disciplinare: **PHYS-06/A**

DOTTORANDO / A
PAOLA PERION

COORDINATORE
PROF. FRANCESCO LONGO

SUPERVISORE DI TESI
PROF. FULVIA ARFELLI

CO-SUPERVISORE DI TESI
PROF. RALF HENDRIK MENK

ANNO ACCADEMICO 2024/2025

UNIVERSITÀ DEGLI STUDI DI TRIESTE

XXXVIII CYCLE OF THE PHD PROGRAM IN

PHYSICS

SPECTRAL PHASE-CONTRAST X-RAY IMAGING: METHODS AND DEVELOPMENT WITH SYNCHROTRON AND LABORATORY SOURCES

Disciplinary Scientific Sector: PHYS-06/A

Ph.D. Student

Paola Perion

Ph.D. Program Coordinator

Prof. Francesco Longo

Thesis Supervisor

Prof. Fulvia Arfelli

Thesis Co-supervisor

Prof. Ralf Hendrik Menk

ACADEMIC YEAR 2024/2025

Abstract

X-ray imaging is routinely used in medicine and scientific research, yet conventional techniques, based solely on absorption contrast, fail to provide sufficient soft tissue contrast or material specificity. Spectral and phase-contrast X-ray methods address these limitations by exploiting the energy-dependent attenuation and the wave nature of X-rays, delivering material quantification and enhanced image quality.

This thesis explores spectral and phase-contrast X-ray imaging in laboratory and synchrotron environments, with a particular focus on crystal-based spectral imaging and beam tracking phase-contrast methods. The work is organized into two main sections: *X-ray imaging* and *Methods and Development*.

X-ray imaging introduces the theoretical and mathematical framework underlying X-ray imaging and describes in detail spectral and phase-contrast imaging principles and techniques implemented throughout this research.

Methods and Development presents the experimental and methodological studies using laboratory and synchrotron sources. Laboratory experiments include spectral micro-computed tomography using an energy resolving photon-counting detector for multiple material discrimination, as well as the development of a novel membrane-stepping approach for phase-contrast imaging which enhances image quality.

Synchrotron-based studies include source-based spectral phase-contrast imaging with beam tracking, applied to thyroid tissue samples for the localization and quantification of iodine and calcium. The final, but central, part of this thesis focuses on crystal-based spectral imaging with beam tracking, supported by simulation studies, crystal and mask optimization, and algorithm development. The optimization studies enhanced the performance and robustness of the spectral and phase-contrast techniques, which were then implemented in imaging experiments, using two distinct setups, demonstrating successful material detection and quantification, as well as effective spectral-phase decomposition that enabled simultaneous structural and elemental characterization of samples.

Overall, these findings establish a framework for integrating spectral and phase-contrast information in X-ray imaging. The developed methods lay a foundation for quantitative, high-resolution, and material-specific imaging, paving the way toward more accurate X-ray imaging approaches for biomedical and materials applications.

Acknowledgements

This work was supported by the University of Trieste and the Istituto Nazionale di Fisica Nucleare (INFN). I acknowledge the Erasmus+ Programme for funding my research stay at University of Grenoble Alpes. I also thank Elettra Sincrotrone Trieste for providing office space and an excellent research environment during my work.

Before actually starting this thesis, I would like to express my gratitude to the people who supported me throughout this three-year journey.

First, I would like to thank my supervisor, Fulvia Arfelli, for giving me the opportunity to pursue this research and for the trust and independence she granted me along the way. I am also sincerely thankful to my co-supervisor, Ralf Hendrik Menk, for his invaluable insights and helpful discussions, which have been an important guide during this work.

My heartfelt thanks goes to Luca Brombal, who taught me so much and set a high standard for what it means to be a researcher. His guidance has truly shaped my growth. I am also very grateful to Luca Sbuelz, with whom I shared the first part of this PhD journey; his support and humor have been essential during many moments.

I would also like to warmly thank Emmanuel Brun and all of his group for welcoming me into the Strobe lab, for his mentorship, and for the opportunity to grow not only scientifically, but also personally.

I wanted to keep these acknowledgements academic, but they felt incomplete. To my friends and family, you know who you are, you have been the pillars upon which I was able to build this. Thank you for staying by my side unconditionally.

Introduction

Since its discovery, X-ray imaging has evolved into a fundamental tool in fields ranging from medicine to materials science, with its applications continuing to broaden and advance over the years. Conventional X-ray imaging is based on absorption contrast, where contrast is generated based on the density of materials. While this approach is effective for imaging materials with large density differences, it faces limitations in distinguishing materials with similar attenuation properties and provides low intrinsic contrast in soft biological tissues.

To overcome these limitations, advanced X-ray methods have emerged, such as spectral and phase-contrast imaging techniques.

Spectral imaging exploits the energy dependence of attenuation to separate and quantify materials by acquiring images at two or more different energies. Several approaches exist: source-based methods tune the X-ray beam energy directly, while detector-based approaches, enabled by the advances in photon-counting technology, now provide energy discrimination at the detection level. Another implementation, which will be thoroughly discussed in this thesis, is energy dispersive crystal-based spectral imaging, typically employed in synchrotron facilities, where a crystal diffracts photons on a continuous energy spectrum. These techniques often take advantage of the K-edges of high-Z elements to enhance contrast and improve material specificity.

Phase-contrast imaging, on the other hand, enhances the visibility of weakly-absorbing structures by detecting the phase shifts induced in X-rays as they traverse a sample. Among the various methods, tracking-based methods rely on structured beam illumination to retrieve complementary information about absorption, refraction, and ultra-small angle scattering properties. These methods provide contrast improvement for soft tissues and biological tissues that would otherwise be scarcely visible with conventional X-ray imaging.

The combination of spectral and phase-contrast imaging offers a comprehensive material characterization capability: spectral methods providing elemental specificity and quantification, phase-contrast revealing structural details in weakly-absorbing samples. Both methods are active areas of research, with ongoing efforts to improve their performance. Optimizing them is crucial for expanding their practical applications in both laboratory and synchrotron environments.

This thesis aims to explore and advance spectral and phase-contrast X-ray imaging through experimental and methodological development. Various spectral and phase-contrast techniques have been implemented, refined, and optimized for different setups, with a dedicated focus to crystal-based beam-tracking techniques. Although

the research carried out during this work spanned multiple experimental setups and imaging modalities, two major objectives guided this work. The first was centered on optimization, working on both hardware and software aspects to improve performance of the techniques individually. The second objective involved implementing a unified spectral phase-contrast system, exploring the integration of spectral and phase-contrast information with the aim of enhancing overall imaging capabilities.

These objectives led to several contributions. In laboratory setups, spectral and phase-contrast imaging were studied individually. Spectral imaging experiments using a photon-counting detector demonstrated multi-element discrimination and quantification, including for unconventional contrast elements. Then, a membrane-stepping optimization strategy for phase-contrast imaging showed an improved image quality. At the synchrotron, a first spectral phase-contrast experiment was carried out on human thyroid samples, demonstrating the possibility of simultaneously accessing structural and elemental information. Then, a comprehensive characterization of the crystal for crystal-based spectral imaging was carried out, supported by dedicated simulation tools to predict experimental outcomes and guide the system design. The beam tracking algorithm was optimized, achieving improved robustness and retrieval accuracy. Finally, the first imaging results from both the original and an alternative crystal-based setup were obtained, demonstrating the feasibility and potential of combined crystal-based spectral phase-contrast imaging.

Together, these contributions support the broader goal of enabling more versatile and efficient X-ray imaging systems in both laboratory environments and large-scale synchrotron facilities.

The thesis is organized into four chapters.

Chapter 1 introduces the fundamentals of X-ray imaging, beginning with the mechanisms of X-ray absorption and interaction with matter, and progressing to a description of their wave-like nature. The chapter continues describing the principles of computed tomography and concludes with an overview of laboratory and synchrotron X-ray sources.

Chapter 2 discusses spectral and phase-contrast X-ray imaging. It explains the spectral techniques employed during this PhD, outlining the mathematical formulation of the various material decomposition algorithms used. The chapter also describes the main phase-contrast methods and concludes with a discussion on the combination of spectral and phase-contrast imaging approaches.

Chapter 3 presents the laboratory activities carried out over the course of the PhD. It first details spectral imaging experiments performed using a laboratory source coupled with an energy-resolving photon-counting detector, demonstrating the capability to discrim-

inate among multiple elements within a sample. The second part describes the work carried out during a six-month research period in France, where a membrane-stepping optimization approach for phase-contrast imaging was developed and tested to improve image quality.

Chapter 4 talks about X-ray imaging at synchrotron facilities. It begins with the description of combined source-based spectral phase-contrast imaging performed on thyroid tissue samples and then proceeds to the central part of the thesis, conducted in the context of the Sphere-X project at the Elettra synchrotron of Trieste. This chapter presents comprehensive studies of the experimental setups, including crystal and mask characterization, simulation development for predicting experimental outcomes, optimization of the beam-tracking algorithm, and the final imaging results obtained from both the original and an alternative setup.

Contents

List Of Abbreviations

CT	Computed Tomography
High-Z	High atomic number
BP	Back Projection
FBP	Filtered Back Projection
KES	K-edge Subtraction
SKES	Spectral K-edge Subtraction
XPCDs	X-ray photon-counting detectors
UMPA	Unified Modulated Pattern Analysis
LCS	Low Coherence System
PEPI	Photon-counting Edge-illumination Phase-contrast Imaging
MoBI	Modulation-Based Imaging
PMMA	Polymethyl Methacrylate
CNR	Contrast-to-noise ratio
SPHERE-X	Spectral PHasE REtrieval X-ray imaging
ESRF	European Synchrotron Radiation Facility
RQM	Quasi-Mosaic Radius
CDP	Curved Dispersive Plate
FWHM	Full Width at Half Maximum
RMSE	Root Mean Square Error
PSF	Point Spread Function
SNR	Signal-to-noise Ratio
MTF	Modulation Transfer Function
SYRMEP	SYnchrotron Radiation for MEdical Physics
ROI	Region of Interest
XPCI	X-ray Phase-Contrast Imaging
XSI	X-ray Spectral Imaging
μCT	Micro-Computed Tomography

Part I

X-RAY IMAGING

1

Fundamentals of X-ray imaging

X-rays were discovered by Wilhelm Conrad Röntgen in 1896 [Röntgen 1896a; Röntgen 1896b]. Röntgen observed that these "new kind of rays" had the capability to penetrate almost everything, including the soft tissue of his wife Bertha's hand, but not her bones or metal objects, which instead cast a shadow on a photosensitive plate.

Following this discovery, the use and investigation of X-rays for medical applications began. Diagnostic radiography emerged as an application, based on the understanding that X-rays, just like visible light, were characterized by wavelength and intensity. However, Röntgen noted that despite this similarity, X-rays did not initially appear to exhibit behaviors typically associated with waves, such as diffraction, refraction, and interference, or, if such phenomena did occur, they were too small to be detected. As a result, radiographic imaging focused exclusively on absorption contrast, where differences in X-ray attenuation between tissues produced the diagnostic image.

Figure i: One of the earliest radiographs of the hand of Röntgen's wife, Bertha, with her wedding ring clearly visible.

Over time, radiology established itself as a fundamental component of clinical medicine, eventually achieving recognition as an independent medical specialty in 1918. In the 1970s, the introduction of linear accelerators as X-ray sources and the discovery and development of computerized tomography (CT) began yielding much greater anatomical differentiation of body tissues [Hounsfield 1973].

Despite these advances, the basic principle of radiography-casting a shadow image of the sample with a detector opposite the X-ray source-has remained unchanged. However, there have been major advances in digital imaging and computational analysis. A significant development has been the recognition and utilization of the wave nature of X-rays in phase-contrast imaging [Wilkins et al. 2014; Endrizzi 2018].

X-rays are electromagnetic waves with a wavelength between 0.01 nm to 0.1 nm, about 10000 times smaller than visible light. While conventional radiography relies on absorption contrast, where denser materials attenuate X-rays more strongly, phase-contrast imag-

ing captures the subtle, but measurable, phase shifts that X-rays undergo when passing through materials with different refractive indices. This technique enables visualization of soft tissues and fine structures that would otherwise be invisible using conventional methods.

Today, X-rays are not only used routinely in medicine and in academic and corporate research, but their range of applications has broadened, including security screening, industrial inspection, and art conservation.

This chapter begins by discussing the particle-like behavior of X-rays, followed by an introduction to their wave-like properties and the concept of coherence as relevant to phase-contrast imaging. Next, the mathematical foundations of computed tomography are presented. The chapter concludes with an overview of X-ray sources, with particular focus on laboratory and synchrotron X-ray sources.

1.1 X-RAYS AS PARTICLES

X-rays are a type of electromagnetic radiation, typically having energies ranging from 10 keV to 150 keV within the diagnostic energy range. There are two accurate ways of describing them: as electromagnetic waves or as discrete quanta of energy called photons. In this section, we will focus on the particle-like nature of X-rays to better understand how they interact with matter.
When an X-ray photon encounters matter, several interaction mechanisms can occur. The most significant processes in the diagnostic energy range are:

1. **Photoelectric effect** - responsible for photon absorption
2. **Compton scattering** - an inelastic scattering process involving partial energy and momentum transfer
3. **Rayleigh scattering** - an elastic scattering process where the photon changes direction but its energy remains unchanged.

The total interaction cross section σ is the sum of the individual photon interaction cross sections for the relevant processes occurring within this energy range:

$$\sigma = \sigma_{PE} + \sigma_{CS} + \sigma_{RS} \tag{1.1}$$

where σ_{PE}, σ_{CS}, and σ_{RS} represent the cross sections for the photoelectric effect, Compton scattering, and Rayleigh scattering, respectively. In the context of this thesis, the focus will be mainly on the photoelectric effect, due to its dominance at lower X-ray energies.

1.1.1 *The Photelectric Effect and K-edges*

Photoelectric absorption plays a key role in X-ray interactions at energies relevant to imaging. This process occurs when a photon transfers all its energy to a bound atomic electron, typically from an inner shell, causing the electron to be ejected from the atom.

The K-edge energy corresponds to the binding energy of the innermost electron shell (K-shell). The linear attenuation coefficient indicates photon interaction probability and is proportional to the interaction cross section. Thus, when a photon's energy slightly exceeds the K-shell binding energy, there is a sharp increase in absorption probability, leading to a discontinuity in the linear attenuation coefficient called K-edge (see Figure 1.2b). This process is very significant in elements with a high atomic number (high-Z), such as iodine and barium, for X-rays in the diagnostic energy range. The theoretical non-relativistic cross-section for a single, unscreened K-shell is proportional to Z^5 [Heitler 1984], where Z is the atomic number. However, for real atoms and far from the K-edge, the total photoelectric atomic cross-section is empirically found to be proportional to Z^4/E^3, where E is the photon energy. Consequently, the photoelectric mass attenuation coefficient μ_{PE}/ρ is approximately proportional Z^3/E^3. In contrast, Compton scattering has a minimal dependence on energy. At lower photon energies, the photoelectric effect dominates due to its strong energy dependence, while at higher energies, Compton scattering becomes the primary interaction mechanism.

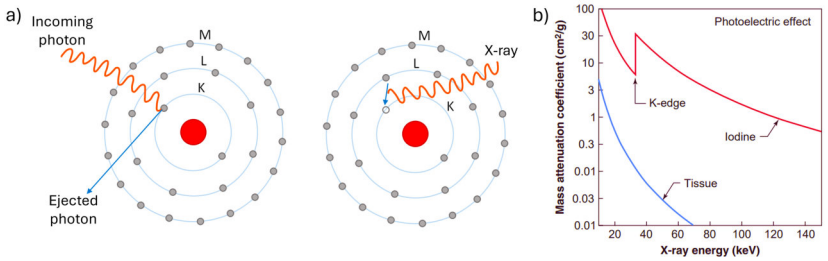

FIGURE 1.1: a) Photoelectric absorption: an incident photon is absorbed and causes the ejection of an electron. An electron of an outer shell then takes its place emitting a fluorescence X-ray. b) Photoelectric mass attenuation coefficients μ/ρ_{PE} for tissue ($Z_{effective} = 7$), and iodine ($Z = 53$) as a function of energy. Atomic absorption edge of iodine at 33.2 keV can be seen. Graph taken from [Bushberg et al. 1994].

1.1.2 *Attenuation of X-rays*

Attenuation is the decrease of the intensity of an X-ray beam as it passes through matter, due to both photon absorption and scattering. The attenuation of a photon beam is quantified by the linear absorption coefficient μ, which represents the probability of photon interaction per unit thickness of the material. It describes the fraction of photons that interact with the material per unit of path length

at a given energy. This quantity is often used when divided by the mass density: this ratio is called the *mass absorption coefficient*. The mass absorption coefficient μ/ρ is independent of the density of the material, and it can be related to the cross section σ through the following formula:

$$\frac{\mu}{\rho} = \frac{N_A}{A}\sigma \tag{1.2}$$

where N_A is the Avogadro number and A is the atomic mass. This implies that, just like cross section, that the total mass attenuation coefficient can be expressed as the sum of the individual mass attenuation coefficients of the relevant interaction processes:

$$\frac{\mu}{\rho} = \frac{\mu_{PE}}{\rho} + \frac{\mu_C}{\rho} + \frac{\mu_R}{\rho} \tag{1.3}$$

In general, across the energies commonly used in diagnostic imaging, which range from a few keV to hundreds of keV, photoelectric and Compton effects are the most dominant interactions that occur.

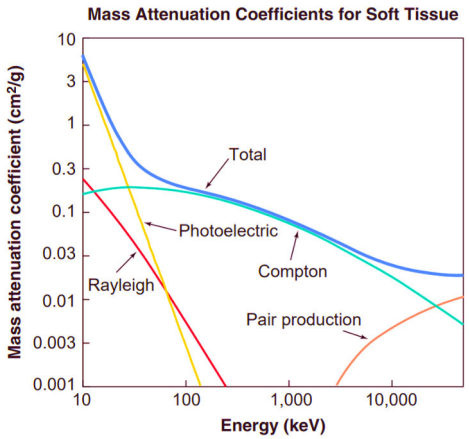

FIGURE 1.2: Graph of the Rayleigh, photoelectric, Compton, pair production, and total mass attenuation coefficients for soft tissue (Z ≈ 7) as a function of photon energy. Pair production is another interaction process which is not mentioned in the text as it occurs at energies >1000 keV. Figure taken from [Bushberg et al. 1994]

The law that calculates photon transmission through a material of thickness z for a monoenergetic beam is called *Lambert-Beer* law and it states:

$$I(x,y) = I_0\, e^{-\int_0^z \mu(x,y,z)\, dz} \tag{1.4}$$

where I_0 is the initial intensity of the beam, I is the intensity after exiting the material of thickness z, and μ is the total attenuation coefficient (cm^{-1}).

1.2 X-RAYS AS WAVES

While the particle-like behavior of X-rays explains discrete interaction mechanisms such as the photoelectric effect, a more complete understanding of X-ray propagation through matter requires considering their wave-like nature. We start from the Helmholtz equation, which is the time-independent form of the wave equation, and can be written, in scalar approximation, as:

$$\nabla^2\psi + n^2k^2\psi = 0 \tag{1.5}$$

where n is the index of refraction, $k = 2\pi/\lambda$ is the wave number, and λ is the wavelength. For X-rays the index of refraction is complex and can be expressed as $n = 1 - \delta + i\beta$, where δ the *refractive index decrement* and β is the *absorption index*. If the energy of X-rays is sufficiently higher than the energy of the absorption edges of the medium, δ can be calculated in classical electrodynamics as:

$$\delta \approx r_0\rho_e\lambda^2/2\pi \tag{1.6}$$

where $r_0 \approx 2.82 \times 10^{-15}$ is the classical electron radius and ρ_e is the electron density. The complex refraction index is very close to unity, which means that both δ and β are very small numbers.

If we consider a parallel, monochromatic X-ray wave traveling in vacuum along the z axis, this corresponds to a plane wave that can be expressed as:

$$\psi = \Psi\ e^{ikz} \tag{1.7}$$

If we insert the equation into the Helmholtz equation and simplify, we obtain the following:

$$\nabla^2\Psi + 2ik\partial_z\Psi + k^2(n^2 - 1)\Psi = 0$$

After adopting the projection approximation, which assumes that the object's refractive index distribution varies slowly along the beam direction, the Laplacian term becomes negligible. Furthermore, the refractive index n is very close to unity, leading to the approximation $1 - n^2 \sim -2\delta n = 2(\delta - i\beta)$. Applying these approximations and integrating the equation yields:

$$\Psi(x,y,z) = \Psi(x,y,z=0)\ exp\left\{\frac{k}{i}\int_0^z (\delta - i\beta)\ dz\right\} =$$

$$= \Psi(x,y,z=0)\ exp\left\{-ik\int_0^z \delta\ dz - k\int_0^z \beta\ dz\right\} \tag{1.8}$$

The wave can therefore be expressed as the sum of two contributions: a phase shift term, which depends on the refractive index decrement δ and an attenuation term, which depends on the absorption index β. These effects are shown in Figure 1.3. The phase shift of the wave is defined as:

$$\Phi = -k \int_0^z \delta \, dz \tag{1.9}$$

and is associated with the passage of an X-ray wave through the object, quantifying the wave-front deformations and associated refractive properties of the object.

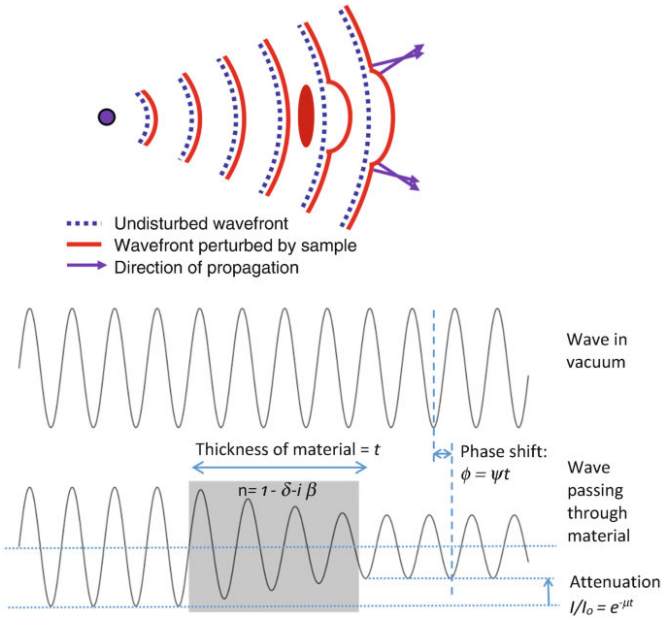

FIGURE 1.3: An X-ray wave that interacts with matter is subject to both amplitude attenuation and phase shift. Figure taken from [Mayo and Endrizzi 2019]

The intensity of the wave is expressed as its squared modulus:

$$I(x,y,z) = |\Psi(x,y,z)|^2 = I(x,y,z=0)\, exp\left\{-2k \int_0^z \beta \, dz\right\} =$$

$$= I(x,y,z=0)\, exp\left\{-\int_0^z \mu \, dz\right\} \tag{1.10}$$

Equation 1.10 is the Lambert-Beer law of attenuation introduced in Section 1.1.2, where $\mu = 2\beta k$ is the linear attenuation coefficient. It is important to note that the phase information in this equation cancels out due to the square modulus. As a result, in conventional X-ray experiments where only the intensity of the wave is measured, the phase information is typically lost and only the absorption is accessible. Nevertheless, X-rays that interact with matter are subject to both amplitude attenuation and phase shift. To access the phase

information in X-ray imaging, phase-contrast imaging techniques have been developed; these will be thoroughly described in the next chapter.

At X-ray energies typical of biomedical imaging, the refractive index decrement δ is typically 1000 times larger than the imaginary part β, making the effects due to phase shift substantially more relevant than those due to absorption. This is particularly relevant when imaging low-Z materials: while absorption scales strongly with atomic number, phase shift is governed by electron density (see Equation 1.6), making phase-based imaging especially advantageous for visualizing soft tissues and other weakly absorbing structures.

However, as mentioned earlier, phase effects were not observed in the early experiments of Rontgen, and do not play any role in conventional X-ray imaging methods where only absorption is taken into account.

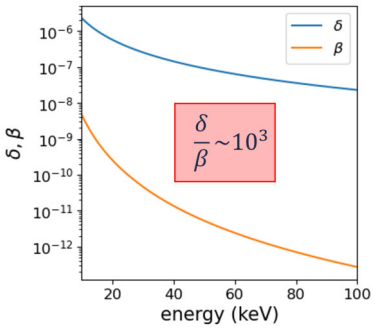

Figure ii: δ and β of water as a function of energy.

1.2.1 *Refraction and scattering of X-rays*

As anticipated in this section, the real part δ of the complex refractive index is related to the refraction of X-rays. The phase shift for an X-ray passing through an object is:

$$\Phi(x,y,z) = -k\int \delta(x,y,z)\,dz = -\frac{2\pi r_0}{k}\int_0^z \rho_e(x,y,z)\,dz \quad (1.11)$$

A phase shift in the wavefront alters the direction of wave propagation (see Figure 1.3). If we assume that the wave propagation does not deviate much from the propagation axis z (i.e. *Paraxial approximation*), then the gradient of the phase $\nabla\Phi << k$. We can therefore express the angular deviation of the wavefront as [Wilkins et al. 1996]:

$$\Delta\alpha \approx \frac{1}{k}\left|\nabla_{x,y}\Phi(x,y,z)\right| = \left|\nabla_{x,y}\int \delta(x,y,z)\,dz\right| \quad (1.12)$$

What is commonly referred to as scattering or dark-field signal arises from the same underlying refraction phenomenon, but occurs when the X-ray beam encounters a large number of interfaces in matter. These interfaces induce multiple small-angle deflections, eventually leading to an overall diffusion of the beam in all directions. When the length scales of these structures are smaller than the spatial resolution of the imaging system, their individual contribution cannot be resolved. The system detects a broadening or blurring effect of the beam profile. The average angular spread of the beam due to this multiple refraction effect is given by [Nardroff 1926; How et al. 2023]:

$$\alpha_{df} = 2\delta\sqrt{N\left(log\frac{2}{\delta}+1\right)} \tag{1.13}$$

This expression quantifies the effective beam divergence α, where δ is the refractive index of the micro-structures, and N is their number, which is given by:

$$N = \frac{3\ p_f\ T}{4R} \tag{1.14}$$

where p_f is the packing fraction of the spheres, R is their radius, and T is the traversed thickness.

Such diffusion is responsible for the contrast in dark-field imaging, which enables sensitivity to sub-resolution structures that would otherwise remain invisible in conventional absorption or phase-contrast modalities. This will be better described in Chapter 2.

1.2.2 *X-ray coherence*

A fundamental concept in X-ray imaging is coherence, which is the ability of a wave to produce interference effects. In imaging systems, coherence refers to how well a wavefield can interfere with itself, which is an essential requirement for advanced phase-contrast imaging techniques. An imaging system has a certain degree of coherence if it is able to produce visible interference patterns [Born and Wolf 2013].

We can define two types of coherence: Longitudinal coherence, which is related to energy spread of the source, and Transverse coherence, which depends on the source size. An ideal imaging system, composed of a monochromatic point-like source, would be perfectly coherent. Real sources will obviously not be ideal, and their degree of coherence will depend on how well they approximate these conditions.

Longitudinal coherence - polychromaticity

X-ray sources are typically polychromatic, meaning that they emit a range of wavelengths. Different wavelengths normally have no phase relationship, hence all measurements made with polychromatic x-rays are simply the sum, in intensity, of all the individual frequency components, averaging out the interference terms. However, this consideration is still compatible with the concept of *longitudinal coherence*, which quantifies the length scales over which a wavefield can interfere with itself along the propagation direction. The longitudinal coherence length L_l is defined as:

$$L_l = \frac{\lambda^2}{\Delta\lambda} \tag{1.15}$$

where λ is the central wavelength, and $\Delta\lambda$ is the spectral bandwidth of the source. The smaller $\Delta\lambda$, i.e. the more monochromatic is the source, the longer the coherence length is. Typical values for laboratory X-ray sources are in the order of hundreds of nm, while for synchrotron sources values can reach tens of microns.

Transverse coherence

Transverse coherence defines a scale for the coherence on the object plane (perpendicular to the beam propagation direction). It mainly depends on the spatial extent of the source and the propagation distance. Transverse coherence length L_t is given by:

$$L_t = \frac{\lambda z_1}{S} \tag{1.16}$$

where z_1 is the source to sample distance and S is the source size. If the size of the object is smaller than this length, the object will effectively experience the illumination as transversely coherent. Typical values for a micro-focus laboratory X-ray source are in the order of a micrometers, while for synchrotron sources values can reach tens of microns. For effective phase-contrast imaging, the sample features of interest should be comparable to or smaller than both coherence lengths.

1.3 COMPUTED TOMOGRAPHY

Computed tomography (CT) is an imaging technique that allows reconstructing cross sectional images of an object. It is based on the transmission of X-rays through matter and, as opposed to planar radiography, which produces projection images, it generates tomographic images. This is achieved by collecting many X-ray projection images at different angles with respect to the sample, and using them to reconstruct the distribution of the attenuation coefficient $\mu(x, y)$ of the sample. The mathematical methodology for image reconstruction is described in the following paragraphs and is based on the approach described in [Kharfi 2013].

A two-dimensional Cartesian coordinate system (x,y) is chosen to define the reconstructed slice (see Figure 1.4).

A new rotational coordinate system (t,s) is introduced, related to the Cartesian system (x,y) in the following way:

$$\begin{aligned} t &= \ \ x\cos\theta + y\sin\theta \\ s &= -x\sin\theta + y\cos\theta \end{aligned}$$

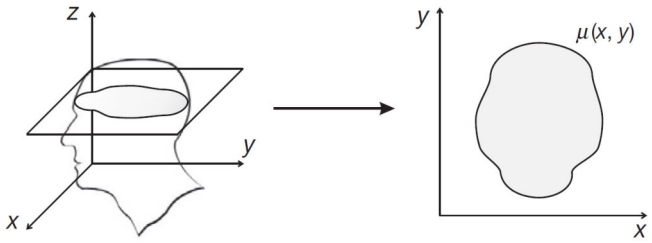

FIGURE 1.4: Tomographic reconstruction aims to recover the distribution of the linear attenuation coefficients, on a section of the patient's body. Sketch taken from [Brahme 2014]

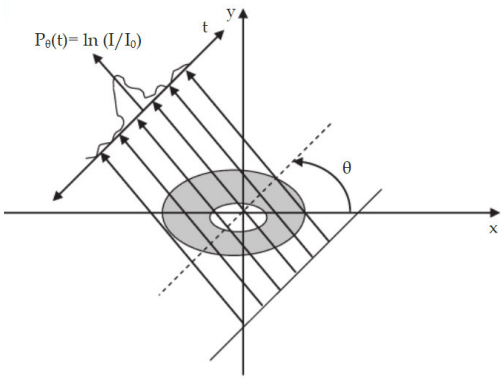

FIGURE 1.5: Scanning of a layer in the plane (x,y). $P_\theta(t)$ is the obtained projection.

While scanning a slice of an object $f(x, y)$ by varying the angle θ, projections $P_\theta(t)$ are obtained. The total attenuation of the X-ray beam along each line of propagation is the line integral of μ over that line (from Equation 1.4):

$$P_\theta(t) = -ln\left(\frac{I}{I_0}\right) = \int_{path} ds\ \mu(x, y) \tag{1.17}$$

Which can be written as:

$$P_\theta(t) = \int_{-\infty}^{+\infty} \int_{-\infty}^{+\infty} \delta(xcos\theta + ysin\theta - t)\mu(x, y)\ dxdy \tag{1.18}$$

where δ is the Dirac delta function. The set of all projection data $P_\theta(t)$ obtained as an output from a tomographic scan is called sinogram, or mathematically, the Radon transform of the object [Radon 2005]. Each row of the sinogram represents a radiographic projection in one dimension, and the sinogram contains enough information to analytically reconstruct a two-dimensional slice. The ultimate goal of tomographic reconstruction is to invert the Radon transform in order to obtain $\mu(x, y)$.

The original distribution of the object can be recovered through problem inversion making use of the Fourier Central Slice theorem.

The latter states that the data of the 1D Fourier transform of a projection $P_\theta(t)$ is a subset of the data of 2D Fourier transform $F(u,v)$ of the object function $\mu(x,y)$: $FT[P_\theta(t)] = F_\theta(w) \subset FT[\mu(x,y)] = F(u,v)$, where $u = w \cdot cos\theta$ and $v = w \cdot sin\theta$. This means that the values of the Fourier transform of one projection coincide with the values of the Fourier transform of the unknown distribution $\mu(x,y)$ along that scan line. In other words, each projection at a given angle gives us access to a "slice" of the frequency spectrum of the object.

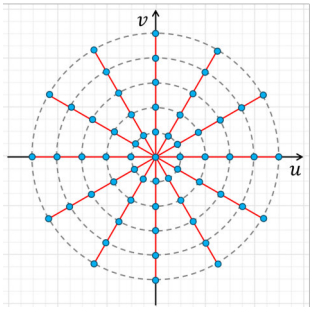

Figure iii: Sampling in Fourier space: the blue dots are the 1D Fourier transform of the set of all projection data $P_\theta(t)$, where each radial line corresponds to a projection. It is important to note that the radial sampling is higher at lower frequencies.

Therefore, the inverse transformation of the Fourier transform of $P_\theta(t)$ can be used to produce the reconstructed layer of $\mu(x,y)$. This is also called backprojection (BP). Unfortunately, backprojection alone is not able to reconstruct the object with high fidelity. This is due to the radial sampling in Fourier space, where the sampling at higher spatial frequencies is more sparse compared to the one at low frequencies. It is therefore convienent to use polar coordinates rather than cartesian ones.
The inverse Fourier transform $\mu(x,y)$ of $F(u,v)$ written in Cartesian coordinates is given by:

$$\mu(x,y) = \int_{-\infty}^{+\infty} \int_{-\infty}^{+\infty} F(u,v)\, e^{2\pi i(ux+vy)}\, du dv \tag{1.19}$$

The same inverse transform in polar coordinates is given by:

$$\mu(x,y) = \int_{0}^{2\pi} \int_{-\infty}^{+\infty} F(\omega,\theta)\, e^{2\pi i\omega(xcos\theta+ysin\theta)}\, \omega\, d\omega d\theta \tag{1.20}$$

By substituting $t = x\ cos\theta + y\ sin\theta$:

$$\begin{aligned} \mu(x,y) &= \int_{0}^{\pi} \int_{-\infty}^{+\infty} F(\omega,\theta)\, e^{2\pi i\omega t}\ |\omega|\ d\omega d\theta = \\ &= \int_{0}^{\pi} \left[\int_{-\infty}^{+\infty} F(\omega,\theta)\, e^{2\pi i\omega t}\ |\omega|\ d\omega \right] d\theta \end{aligned} \tag{1.21}$$

The integral in brackets can be regarded as the inverse Fourier transform $P_\theta(t)$ of $P_\theta(w)$. $|w|$ is a filter in the frequency domain called *ramp filter*. Because the sampling density decreases linearly with the absolute value of the spatial frequency, the filtering function must increase linearly with the absolute value of the spatial frequency. Equation 1.21 is the so-called *filtered back projection (FBP)*.

FBP is one of the most common CT reconstruction algorithms. Nevertheless, there are various other algorithms that are used in different contexts, but they will not be described in this work. Their description can be found in [Hiriyannaiah 1997; Beister et al. 2012; Russo 2017].

1.4 X-RAY SOURCES

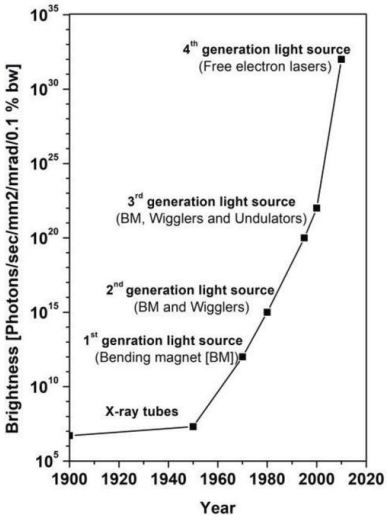

Figure iv: Peak brilliance for X-ray tubes and 1^{st}, 2^{nd}, 3^{rd}, and 4^{th} generation light sources as a function of year. Figure taken from [Bharti and Goyal 2019]

Since the discovery of X-rays, X-ray tubes have been the most commonly used source, widely used for medical diagnostics, industry and science, owing to their availability and cost-effectiveness [Behling and Grüner 2018].

One key parameter of X-ray sources is brightness, which refers to the photon flux (photons/second) per unit area, and per unit solid angle, or brilliance, which is the brightness per unit energy bandwidth. It is no surprise that the higher the brilliance, the higher the quality of the source. In recent years, the growing demand for higher brilliance in laboratory settings has led to the development of compact high-brightness light sources, such as *liquid metal jet anode* and *inverse compton scattering* X-ray source sources. Liquid metal jet sources exploit a focused electron beam which is directed onto a continuous liquid metal jet, which replaces the traditional solid anode. These sources can sustain higher termal loads, allowing for a higher electron beam power density and resulting in a significantly increased X-ray flux compared to traditional solid anodes [Hemberg et al. 2003]. In alternative, inverse compton scattering sources generate X-rays by colliding a high-power laser beam with a relativistic electron beam. The photons from the laser are backscattered and gain energy from the electron beam, producing highly collimated X-ray photons [Graves et al. 2014].

On the other hand, large-scale facilities such as synchrotrons and X-ray free-electron lasers provide the highest levels of brightness and spatial coherence. The highly-collimated synchrotron beams are ideal for high-resolution spectroscopy and imaging applications [Willmott 2019].

Free-electron lasers use linear accelerators to generate femtosecond-duration pulses of coherent X-rays with peak brightness several orders of magnitude greater than that of synchrotrons [O'Shea and Freund 2001].

Within the scope of this thesis, two main categories of sources will be described: conventional laboratory X-ray sources and synchrotron radiation sources. Each offers different characteristics in terms of beam quality, energy spectrum, flux, coherence, and accessibility.

1.4.1 *Laboratory X-ray sources*

X-rays are produced when highly energetic electrons interact and are decelerated in matter, converting some of their kinetic energy into electromagnetic radiation. A device that produces X-rays in the diagnostic energy range typically contains an electron source, or *cathode*, an evacuated path for electron acceleration, a target

electrode, or *anode*, and an external power source to provide a high voltage to accelerate the electrons (see Figure 1.6).

The cathode generally contains one or more tungsten filaments. When current passes through the filament, the latter is heated through electrical resistance, leading to thermionic emission: the release of electrons from the filament surface. These free electrons are then accelerated across the vacuum by a high-voltage potential toward the anode. When the emitted electrons reach the anode, electrical forces attract and decelerate them changing their direction, causing a loss of kinetic energy. This energy loss is emitted in the form of X-ray photons through a process known as *bremsstrahlung radiation*. The energy of each X-ray photon depends on the electron's loss of energy.

The X-ray energy spectrum resulting from this type of interaction is continuous, ranging from 0 to a maximum equal to the kinetic energy of the incident electrons (determined by the tube voltage). In addition to this spectrum, discrete X-ray energy peaks called *characteristic radiation* can be produced when inner-shell electrons in a target atom are ejected creating a vacancy, causing an outer-shell electron with less binding energy to transition to fill the vacancy emitting a characteristic X-ray. The energy of this X-ray is equal to the difference in the electron binding energies of the two shells, and is called *characteristic* because it depends on the target material.

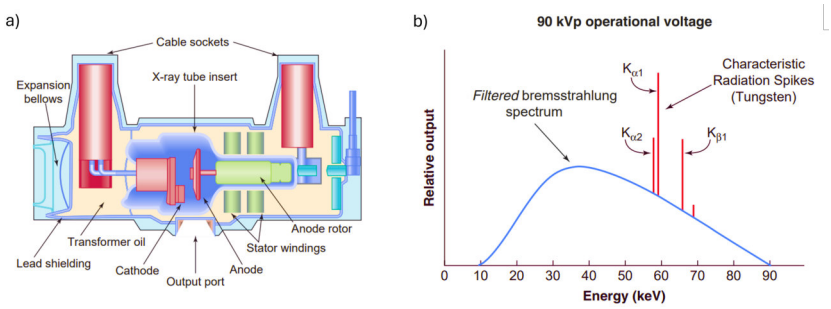

FIGURE 1.6: a) Sketch of the major components of a modern X-ray tube and housing assembly. b) Filtered spectrum of bremsstrahlung and characteristic radiation from a tungsten target with a potential difference of 90 kV. Figure taken from [Bushberg et al. 1994]

Tungsten is the most commonly used anode material because of its high melting point and high atomic number. Other anode materials, such as molybdenum and rhodium, are also used as anode materials in imaging applications where softer X-ray spectra are advantageous, such as mammography. The target materials affect the efficiency of bremsstrahlung radiation production, with the output exposure being proportional to the square of the atomic number.

Conventional X-ray sources can have a fixed anode or a rotating anode. Fixed anodes have the lowest brightness of all sources as they have limited heat dissipation, with values around 10^5 photons s^{-1} mm^{-2} $mrad^{-2}$ 0.1 % bandwidth. In contrast, rotating anode sources

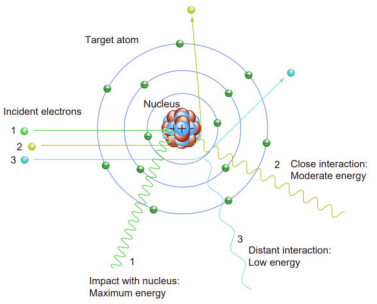

Figure v: Bremsstrahlung radiation arises from the interaction of an electron an atomic nucleus of the target material. The interaction consists in deceleration and redirection, resulting in a loss of kinetic energy that results in an X-ray. The X-ray energy depends on the interaction distance between the electron and the nucleus. Figure taken from [Bushberg et al. 1994]

dissipate heat more efficiently by distributing it over a larger surface area, gaining an order of magnitude in brightness [Paganin 2006]. Another class of laboratory sources are microfocus X-ray tubes, which produce X-rays from a very small focal spot size, typically in the range of a few micrometers, allowing for high-resolution imaging [Mayo et al. 2002].

Conventional X-ray tubes have the advantage of being compact, cost-effective, and very accessible. However, they are limited in performance compared to large-scale sources such as synchrotrons. Specifically, laboratory tubes produce lower photon flux and intensity, and are characterized by limited spatial and temporal coherence [Ou et al. 2021].

1.4.2 *Synchrotron X-ray sources*

Synchrotron sources are based on a different physical process. In synchrotron facilities, electrons are accelerated to relativistic speeds, close to the speed of light, and are forced to travel on curved paths using magnetic fields, such as bending magnets, wigglers, or undulators. As electrons are deflected, they emit radiation tangentially to their trajectory: this radiation is called *synchrotron radiation*. This electromagnetic radiation goes from infrared to hard X-rays.

A synchrotron is composed of five main components: electron source, booster ring, storage ring, radio frequency supply, and beamlines (see the margin Figure vi). Electrons are typically generated via thermionic emission from a heated filament and are then pre-accelerated and injected into a booster ring, where their energy is increased to match that of the storage ring. Electrons are periodically transferred from the booster to the storage ring to maintain beam current.

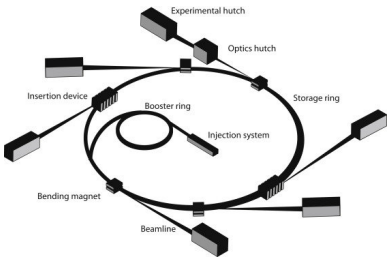

Figure vi: Generic scheme of a synchrotron facility. Figure taken from [Dubsky 2021].

The trajectory of the electrons in the storage ring is controlled by multiple magnetic components. Modern synchrotrons use a modular ring structure composed of alternating arched sections (with bending magnets) and straight sections containing insertion devices (undulators or wigglers) that generate highly collimated and intense synchrotron radiation.

The emitted radiation is collected by beamlines, which work tangentially to the bending magnet, and is conveyed to experimental chambers.

Synchrotron X-rays are suitable for advanced imaging techniques, such as phase-contrast imaging and X-ray microtomography, and are considered the gold standard for these applications [Lewis 1997; Sedigh Rahimabadi et al. 2020]. X-rays produced in synchrotrons have high brilliance, reaching 10^{20} photons s^{-1} mm^{-2} $mrad^{-2}$ 0.1 % bandwidth, high angular collimation that confines the emission, small effective source size, and high coherence. Additionally, beam-

lines can select specific energies using monochromators, enabling energy-resolved or monochromatic imaging. These properties allow for the acquisition of images with low noise, high spatial resolution, and enhanced contrast.

On the other hand, synchrotron facilities are less accessible, both in terms of cost and availability, compared to laboratory-based X-ray sources, which can limit their use in routine imaging applications.

2

Spectral and Phase-Contrast X-ray Imaging

As introduced in Chapter 1, conventional X-ray imaging is based solely on absorption contrast. Although this can provide optimal results when visualizing highly absorbing structures, it performs poorly when imaging weakly absorbing materials, such as those composed of low-atomic-number (low-Z) elements.

To overcome these limitations, advances in X-ray imaging have given rise to new imaging modalities that take advantage of additional physical properties of X-rays. The interaction processes described in Chapter 1 all have a dependence on the energy of the X-rays. Spectral imaging exploits this energy dependence to differentiate different materials based on their unique spectral properties. Meanwhile, phase-contrast imaging enhances the visibility of features with weak absorption contrast by detecting phase shifts induced as X-rays traverse the sample.

In this chapter, both spectral and phase-contrast X-ray imaging methods are explored, including their underlying principles and complementary advantages. The discussion begins with spectral imaging, covering the material decomposition algorithm and providing detailed description of the spectral methods used during my PhD research. Following this, an overview of phase-contrast techniques is presented, giving particular emphasis to the techniques employed during my work. The chapter ends with a description of recent developments that integrate spectral and phase information into imaging systems, concluding with a unified spectral phase-contrast material decomposition algorithm.

2.1 SPECTRAL TECHNIQUES

This section incorporates and extends content from my previous work published in [Perion et al. 2024b]. Spectral X-ray imaging is an advanced imaging method whose aim is to obtain information about the

elemental composition of an object by exploiting the energy dependence of X-ray photon attenuation in matter. This procedure requires the images to be acquired at multiple (at least two) X-ray energies, and it can discriminate among different materials/compounds within an object providing quantitative and material-specific maps [Alvarez and Macovski 1976; Vries et al. 2015].

High-atomic-number contrast agents are being used in biomedical X-ray imaging applications to enhance the contrast of otherwise scarcely visible target tissues or structures within the body. When combined with spectral X-ray imaging, the use of contrast elements greatly improves material differentiation and quantification by exploiting the element absorption edges, further increasing the visibility of details of interest [Panahifar et al. 2016; Panta et al. 2018].

Spectral imaging has gained interest over the years because of the rapidly increasing availability of spectral and dual-energy CT systems and the introduction of energy-resolving photon-counting detectors. Several spectral imaging approaches exist for conventional sources. Spectral scanners used in medical applications typically use a *source-based* approach, which involves running multiple standard image acquisitions at different tube voltage settings, also in combination with different filtering to create spectral separation [Fredenberg 2018]. This can be implemented using a single source with sequential scans [Leng et al. 2015], dual-source systems [Flohr et al. 2006], or rapid kVp switching [Kalender et al. 1986]. Alternative techniques include the use of energy discriminating detector technologies, such as sandwich detectors [A. Brooks and Chiro 1978]. The recent advent of photon-counting detectors has revolutionized spectral imaging by allowing energy binning of individual photons, leading to a *detector-based* spectral imaging approach, improving both spatial and spectral resolution [Taguchi and Iwanczyk 2013]. Detector-based spectral computed tomography scanners are also now becoming commercially available in hospitals [Rajendran et al. 2022].

In synchrotron facilities, *source-based* spectral imaging is made possible due to the possibility of making the beam monochromatic. This enables very precise energy selection just above and below the K-edge of a contrast element, exploiting the K-edge subtraction (KES) technique [Jacobson 1953], a dual-energy imaging method that acquires images near the absorption edges. On the other hand, *crystal-based* implementations of KES are performed using a bent Laue crystal in combination with a beam splitter to simultaneously generate and separate two beams at different energies [Thomlinson et al. 2018]. More recently, this concept has been extended to spectral K-edge subtraction (SKES), which employs a bent Laue crystal to acquire images on a continuous energy spectrum surrounding the K-edge, opening the door to more advanced applications such as multiple-contrast-agent

imaging [Zhu et al. 2014].

For the scope of this thesis, source-based synchrotron imaging, detector-based spectral imaging, and crystal-based SKES imaging will be discussed thoroughly in the Sections 2.1.4, 2.1.5, and 2.1.6, respectively.

2.1.1 *K-edge imaging*

K-edge imaging is an X-ray technique that takes advantage of the sharp rise in the attenuation coefficient of certain contrast agents at their K-edges to produce quantitative images of the components of the analyzed object. Contrast agents used in clinical and pre-clinical settings are typically elements with a high-Z, which are introduced in the body to enhance visibility of specific tissues.

K-edge subtraction (KES), consists in acquiring two images at two different energies, just above and below the K-edge of the contrast element. While the mass attenuation coefficient of the embedding material (usually water-like tissue) decreases as the X-ray energy increases, the contrast element exhibits the opposite behaviour at energies around its K-edge. Here, its mass attenuation coefficient rises sharply, allowing to separate it from the embedding material through specific image processing procedures.

An example of the energy selection for KES using iodine as contrast agent and water as embedding material is illustrated in Figure 2.1.

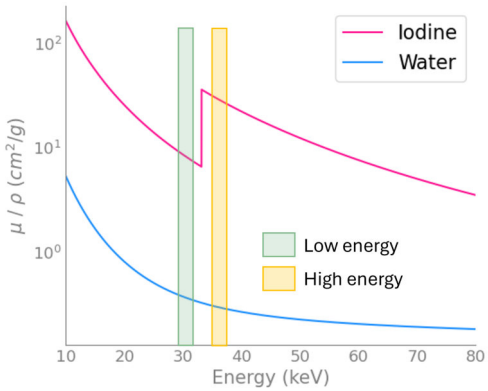

FIGURE 2.1: Mass attenuation coefficient μ/ρ as a function of photon energy, for iodine and water.

The two images taken above and below the K-edge can either be processed through simple logarithmic subtraction or via a material decomposition algorithm. In the first case, the low energy image is subtracted from the high energy image, yielding an image where the positive signal is only due to the contrast medium. In material decomposition, two quantitative images are produced: one for the contrast agent and one for the embedding material (typically water). In tomographic imaging, these images display volumetric density, while in radiographic imaging, they represent projected density. In

this thesis, all images are processed via the material decomposition algorithm approach.

This dual-energy decomposition is described in Section 2.1.2 Equations 2.3 and 2.4. It should be mentioned that this represents the "simplest" case in a broader group of decomposition methods. This concept can be extended to multi-energy decomposition, as in Spectral K-Edge Subtraction (SKES), and to polychromatic sources, as used in most laboratory X-ray systems.

SKES is a generalized version of KES in which material discrimination is performed using a continuous energy spectrum that encompasses the absorption edges of the target elements. As in KES, SKES allows the quantification of the materials of an object thanks to the high rise in mass attenuation coefficient at the K-edge. In contrast to dual-energy approaches, SKES acquires data over tens to hundreds of energy bins, with a relative energy resolution in the order of 10^{-3}, allowing for multi-material decomposition when multiple K-edges are included in the continuous energy spectrum. The multi-material decomposition algorithm is described in Section 2.1.2 Equation 2.5.

While synchrotron-based implementations of KES and SKES typically rely on quasi-monochromatic illumination, most laboratory systems employ polychromatic X-ray tube spectra. In such cases, material decomposition requires additional corrections to account for spectral weighting and detector energy response. The formulation of this polychromatic decomposition approach is presented in Section 2.1.3.

Further details on the SKES technique, including the preparation and tuning of the energy spectrum, are provided in Section 2.1.6.

2.1.2 *Material decomposition algorithm - monochromatic case*

In this section, the material decomposition algorithm, in the case of monochromatic image acquisitions, is described. Consider an X-ray beam passing through an object consisting of two known materials: a contrast agent (material 1) and a water-based material (material 2). According to the Lambert-Beer law (Equation 1.4) the beam intensity will be modulated as:

$$I(E,\vec{z}) = I_0(E)e^{-\frac{\mu(E)}{\rho}\Big|_1\rho_1 z_1 - \frac{\mu(E)}{\rho}\Big|_2\rho_2 z_2}$$

where I_0 is the incident intensity, E is the beam energy and $\vec{z}$ is the vector that contains the materials' thicknesses z_i, where $i = 1, 2$. Let's define $S(E,\vec{z})$ as follows:

$$S(E,\vec{z}) = -ln\left(\frac{I(E,\vec{z})}{I_0(E)}\right) \tag{2.1}$$

The method involves acquiring two images at different X-ray energies, resulting in two independent measurements. These measurements can be expressed as a system of two equations:

$$S^{high} = \frac{\mu}{\rho}\Big|_1^{high} \cdot \rho_1 z_1 + \frac{\mu}{\rho}\Big|_2^{high} \cdot \rho_2 z_2$$

$$S^{low} = \frac{\mu}{\rho}\Big|_1^{low} \cdot \rho_1 z_1 + \frac{\mu}{\rho}\Big|_2^{low} \cdot \rho_2 z_2$$

that can be written in matrix form as follows:

$$\begin{pmatrix} S^{high} \\ S^{low} \end{pmatrix} = \begin{pmatrix} \frac{\mu}{\rho}\Big|_1^{high} & \frac{\mu}{\rho}\Big|_2^{high} \\ \frac{\mu}{\rho}\Big|_1^{low} & \frac{\mu}{\rho}\Big|_2^{low} \end{pmatrix} \begin{pmatrix} \rho_1 z_1 \\ \rho_2 z_2 \end{pmatrix} \tag{2.2}$$

where $\frac{\mu}{\rho}\Big|_i^j$, with $i = 1, 2$ and $j = high, low$ are the mass attenuation coefficients of the two materials at the selected energies. Material 1 corresponds to the contrast agent, and material 2 to a water-based substance. The terms *high* and *low* refer to energies chosen above and below the K-edge of the contrast agent, respectively. For simplicity, dependencies on energy and material thickness are omitted. The mass attenuation coefficients are known, and are available in specific databases [Berger et al. 2010]. Therefore, it should be noted that the system has two equations and two unknowns: this makes the algorithm applicable when decomposing in two materials only.

The matrix can be inverted allowing for the reconstruction of two separate images representing the contrast agent and the water-equivalent material:

$$\rho_1 z_1 = \frac{S_{low}\,\frac{\mu}{\rho}\Big|_2^{high} - S_{high}\,\frac{\mu}{\rho}\Big|_2^{low}}{\frac{\mu}{\rho}\Big|_1^{low}\,\frac{\mu}{\rho}\Big|_2^{high} - \frac{\mu}{\rho}\Big|_1^{high}\,\frac{\mu}{\rho}\Big|_2^{low}} \tag{2.3}$$

$$\rho_2 z_2 = \frac{S_{high}\,\frac{\mu}{\rho}\Big|_1^{low} - S_{low}\,\frac{\mu}{\rho}\Big|_1^{high}}{\frac{\mu}{\rho}\Big|_1^{low}\,\frac{\mu}{\rho}\Big|_2^{high} - \frac{\mu}{\rho}\Big|_1^{high}\,\frac{\mu}{\rho}\Big|_2^{low}} \tag{2.4}$$

We now move to the material decomposition algorithm for SKES, which is a generalized version of the algorithm just described for KES. In SKES, images are acquired on a spectrum that typically contains hundreds of energies, allowing material decomposition for more than two materials. Assuming that the object consists of m known materials and the spectrum is composed of n energies, the intensity of the transmitted beam I_i at the i-th energy is:

$$I(E,\vec{z})_i = I_0(E)_i \; exp\left(\sum_{j=1}^{m} - \frac{\mu(E)}{\rho}\bigg|_j^i \rho_j z_j\right)$$

Here, $I_0(E)_i$ is incident intensity at energy E_i, and $\vec{z} = [z_1, ..., z_m]$ is the vector of materials' thicknesses. Defining $S(E,\vec{z})_i$ as in Equation 2.1, the following matrix system is obtained:

$$\begin{pmatrix} S^1 \\ \vdots \\ S^n \end{pmatrix} = \begin{pmatrix} \frac{\mu}{\rho}\Big|_1^1 & \cdots & \frac{\mu}{\rho}\Big|_m^1 \\ \vdots & & \vdots \\ \frac{\mu}{\rho}\Big|_1^n & \cdots & \frac{\mu}{\rho}\Big|_m^n \end{pmatrix} \begin{pmatrix} \rho_1 z_1 \\ \vdots \\ \rho_m z_m \end{pmatrix} \tag{2.5}$$

The matrix system is composed of n equations and m unknowns, with $m \leq n$: by inverting it through a least-squares minimization algorithm, the $\rho \cdot z$ maps, i.e. the line integrated densities in the case of planar radiography, or the ρ maps, i.e. the densities, in the case of tomography, are obtained for each chosen material.

The algorithm can be applied to any set of chosen materials. In biomedical imaging applications, the most common choice consists in the selection of water, of which soft tissues are mostly composed of, and one or more contrast elements that typically target specific anatomical districts.

It is worth mentioning that, like all matrix inversion algorithms, basis material decomposition tends to amplify the noise of the output data when applied to real (i.e. noisy) data. Several strategies have been conceived to mitigate this effect. These include the use of principal component analysis [Butler et al. 2011], or the use of all available energy bins to identify the main elements in each reconstructed voxel prior the material decomposition [Di Trapani et al. 2022], or finally by constrained minimization [Xie et al. 2019]. For this reason, for best performance, the algorithm requires basis materials with rather different energy dependencies (i.e. appreciably different atomic numbers) to avoid major noise amplification in the matrix inversion. For this reason, spectral decomposition is particularly suited to quantify and separate high-Z contrast media from the soft tissue background.

Finally, it should also be remarked that, by considering the system's geometry (i.e. relative distances and effective pixel size), the applied decomposition procedure is inherently quantitative and does not require any density calibration based on objects with known concentrations.

2.1.3 *Material decomposition algorithm - polychromatic case*

The material decomposition algorithm described in Section 2.1.2 can be extended to the case where the X-ray beam is polychromatic and

the photons are separated in energy bins, which is the typical scenario when using spectral detectors with laboratory sources. In this case, we consider an energy spectra $w(E)$ and a spectral detector with a settable double threshold that allows image acquisition in two energy bins. Denoting $D(E)_j$ as the detector energy response of the j-th bin, Equation 1.4 can be generalized as:

$$I^j = \int_E dE\ D(E)_j\ w(E)\ exp\left(-\int d\hat{s}\ \mu(\hat{z}, E)\right) \tag{2.6}$$

where $j = high, low$ and $\mu(\hat{r}, E)$ is the mass attenuation coefficient that is a function of $\hat{z}$, the position vector and energy E. The integral over $\hat{s}$ denotes the line integral for a ray passing through the object. In the case of a detector with a number $l > 2$ of settable thresholds, $1 \leq j \leq l$. Equation 2.6 can be normalized by dividing it by I_0^j:

$$\frac{I^j}{I_0^j} = \frac{\int_E dE\ D(E)_j\ w(E)\ exp\left(-\int d\hat{s}\ \mu(\hat{z}, E)\right)}{\int_E dE\ D(E)_j\ w(E)} \tag{2.7}$$

The decomposition algorithm proceeds as in the monochromatic case: the logarithm of Equation 2.6 is taken and then the full rank matrix system is inverted in order to find the $\rho \cdot z$ maps for each chosen material.

Since the imaging system acquires each image in an energy bin which is defined by the set thresholds, the mass attenuation coefficient matrix is calculated by integrating the mass attenuation coefficient over the energy spectrum in the specific bin, i.e.:

$$\frac{\mu}{\rho}_j = \frac{\int_E dE\ D(E)_j\ w(E)\ \frac{\mu(E)}{\rho}}{\int_E dE\ D(E)_j\ w(E)} \tag{2.8}$$

where $\frac{\mu}{\rho}_j$ is the mass attenuation coefficient of the j-th bin.

2.1.4 *Source-based*

We now turn to the description of spectral X-ray imaging techniques.

Source-based spectral imaging relies on monochromator crystals at synchrotron beamlines, which allow the generation of monochromatic beams. Narrow energy bands are separated from the polychromatic synchrotron radiation using a Bragg monochromator, which uses a crystal (typically silicon) with a well-known lattice spacing. This device is based on Bragg's law of diffraction, which states:

$$n\lambda = 2dsin\theta_B \tag{2.9}$$

where n is the order of diffraction (an integer, usually 1), λ is the wavelength of the X-ray, d is the spacing between atomic planes in the crystal, and θ_B is the angle of incidence, called Bragg angle. By rotating the crystal to a specific Bragg angle, only X-rays of a particular energy, or wavelength, are diffracted according to Bragg's law. The typical energy resolution for these types of monochromators is in the order of 10^{-4}.

Synchrotron monochromators usually employ a double-crystal configuration: the first crystal selects the desired energy, while the second one redirects the beam back into the horizontal direction, compensating for the angular deflection introduced by the first crystal (see Figure 2.2). This setup ensures beam stability and alignment during energy scans.

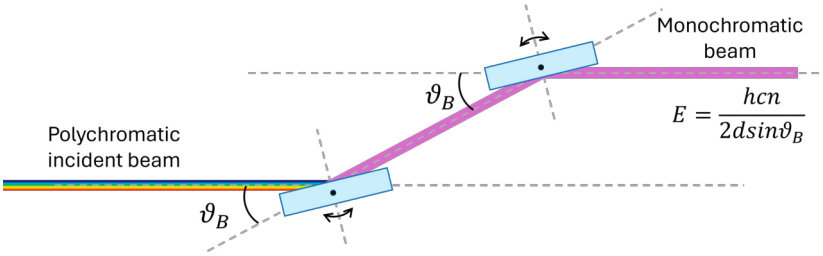

FIGURE 2.2: Double crystal monochromator. The output monochromatic beam has energy $E = hcn/2dsin\theta_B$, where h is Planck's constant, c is the speed of light, d is the spacing between atomic planes in the crystal, and θ_B is the Bragg angle.

For KES imaging, the Bragg angle is first tuned to select an energy just below the K-edge of the material of interest, and the image acquisition is performed. Later, the angle is readjusted to select an energy above the K-edge, followed by a second image acquisition. These two acquisitions are then used as input in the material decomposition algorithm outlined in Equations 2.3 and 2.4 as S_{low} and S_{high}.

The main advantage of this approach lies in the acquisition of two monochromatic images, which makes the material decomposition process reliable, as no spectrum weighting is required. Additionally, synchrotron sources allow for relatively fast acquisitions at a high spatial resolution. However, the limitations of this technique include the need for a sequential acquisition, which is not optimal for time-resolved measurements, and the restricted accessibility of synchrotron facilities.

2.1.5 *Detector-based*

A different approach is represented by X-ray photon-counting detectors (XPCDs), which are direct conversion detectors that directly convert X-ray photons to electric charge. Each detected photon on the detector generates a pulse whose height is proportional to the photon's energy. This type of detector performs counting of single events by selecting photons by means of single/double or multiple

energy thresholds. If the photon releases an energy that exceeds the selected threshold, one event is counted. As a function of the number of thresholds, the counts are grouped into different energy bins, therefore providing spectral information through a single exposure. Material decomposition can be performed on images acquired with XPCDs by applying two energy thresholds: one below the K-edge of the contrast agent energy and one at the K-edge energy.

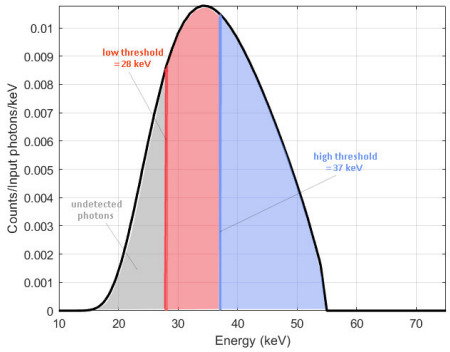

FIGURE 2.3: Example of X-ray spectrum obtained at 55 kVp. The first threshold is set at 28 keV, while the second is set at 37 keV (barium's K-edge is at 37.4 keV). Two ideal energy bins are generated: a low energy bin (in red) and a high energy bin (in blue). In practice, due to finite energy resolution and fluorescence phenomenon, the corresponding energy bins partially overlap. Photons with insufficient energy remain undetected (gray).

In Figure 2.3, an example of X-ray spectrum obtained at 55 kVp containing the K-edge of barium is shown. The two energy thresholds, set at 28 keV and 37 keV, generate two energy bins, illustrated as ideal in the figure. A single exposure therefore yields two images corresponding to these energy bins. In practice, however, the finite energy resolution of the detector causes partial overlap between the bins. In addition, fluorescence and escape peaks can lead to incorrect photon energy assignment.

The main advantage of XPCDs is the ability to perform spectral imaging and material discrimination using conventional X-ray tubes. Spectral data is acquired in a single exposure, which ensures spatial consistency between datasets at different energies. A limitation of XPCDs is their limited sensitive area, typically of a few cm^2, which requires a multi-module architecture to achieve larger fields of view. Additionally, XPCDs' time resolution is limited by their deadtime τ, which imposes a limit on the maximum achievable count rate. Moreover, the limited energy resolution and non-ideal spectral response causes imperfect energy discrimination, resulting in partial overlap between adjacent energy bins and incorrect energy assignment caused by fluorescence and escape peaks, reducing the accuracy of spectral separation [Faby et al. 2015].

2.1.6 *Laue crystal-based*

The experimental implementation of SKES imaging is based on the use of bent Laue monochromators with good focal and energy dispersive properties. This method is well suited for synchrotron beamlines with white beam access. In this kind of setup, a bent Laue crystal is placed at a chosen Bragg angle and acts as a monochromator, diffracting the incoming polychromatic beam. This allows the selection of a continuous energy spectrum containing the K-edge of the contrast element of interest. Due to the crystal's curvature, the diffracted beam geometrically focuses onto a line (where the sample is placed) and then diverges towards the detector.

It is important to note that the beam is dispersed in energy along the diffraction plane, meaning that different energies are mapped onto different pixel rows of the detector. The energy dispersion along the vertical axis means that each row of the detector captures photons of a different energy, while the horizontal direction captures spatial information. Thus, a single exposure acquires spatial data (one "line" of the sample) across a wide energy range. The energy bandwidth comprises tens to hundreds of energy bins, also opening up the possibility of imaging multiple K-edges simultaneously [Bassey et al. 2016].

The resulting images can be processed through the SKES material decomposition algorithm described in Section 2.1.2 to obtain quantitative maps of two or more elements of interest. In Figure 2.4, a schematic representation of the SKES setup is shown.

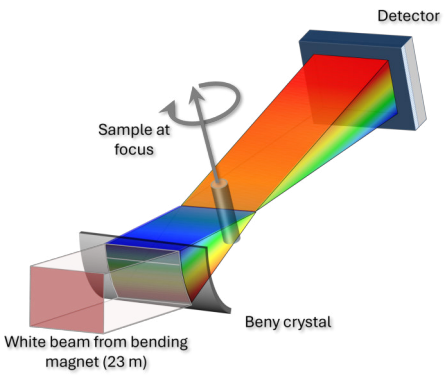

FIGURE 2.4: Sketch of a SKES setup. A polychromatic synchrotron beam reaches a bent Laue crystal and is diffracted. The diffracted beam is focused onto a line and then diverges onto the detector. The energetic dispersion occurs in the diffraction plane.

In the implementation of a SKES setup, both the diffracted spectrum bandwidth and the energy resolution are fundamental parameters defining the overall imaging performance. The spectral bandwidth determines the number and the type of contrast media that can be simultaneously imaged: for fixed geometrical and crystal parameters, the spectral bandwidth is inversely proportional to the

bending radius of the crystal. The energy resolution influences the blurring of the K-edge, thus the accuracy of the material decomposition [Samadi et al. 2016]. In general, the energy resolution of a bent Laue crystal depends on several parameters including the reflection type, the lattice *d*-spacing variation across the crystal due to its curvature, beam divergence, and the effect of the finite source size [Qi et al. 2021]. Nonetheless, it has been demonstrated that by choosing asymmetrically cut crystals matching a focusing criterion referred to as *magic condition* [Martinson et al. 2015; Qi et al. 2019] optimal energy resolution can be reached. This brings a significant reduction of edge-crossing blurring [Samadi et al. 2016].

In conventional KES, a splitter blocks approximately 1/3 of the vertical beam size to create two energy beams. These beams cross the sample at slightly different angles, introducing *crossover artifacts*. This artifact arises because the two beams intersect the object at slightly different angles, and due to the inevitable spatial extension of the sample around the focus, some parts of the object are out of focus when imaged, leading to inconsistencies during image decomposition. SKES minimizes artifacts by narrowing down the vertical beam size and producing a smaller crossover angle. Moreover, having a higher imaging flux is possible since the full beam's height is used without the need for beam splitter systems. Another advantage of this technique is the reduction of motion artifacts due to the acquisition of the image at multiple energies in only one shot rather than sequentially, allowing the imaging of living systems [Elleaume et al. 2002]. Finally, the intrinsically high energy resolution of bent crystals, which is in the order of a few tens of electronvolts, enables enhanced sensitivity to low concentrations of contrast agents, opening the door to quantitative imaging in cases where photon-counting detectors, which are restricted to an energy resolution of 1-2 keV, do not provide sufficient energy resolution [Elleaume et al. 2000].

Some limitations of spectral imaging with bent monochromators are that having the object placed at the beam focus allows the acquisition of only one row of the sample at a time, so a vertical scan is necessary to examine the whole object. Moreover, as of now this type of spectral imaging is limited to synchrotron facilities, and the overall setup is more complex compared to other types of spectral imaging configurations.

The following sections provide a more detailed discussion of bent Laue crystal diffraction, energy bandwidth, energy calibration, focus dimension, and the magic condition.

Bent Laue diffraction

A crystal is a solid with a highly ordered atomic structure. X-ray diffraction in a crystal occurs when the solid selectively reflects or

transmits X-rays from specific atomic planes.

A crystalline lattice is built by translating a unit cell characterized by three primitive translation vectors $\vec{a}_1$, $\vec{a}_2$ and $\vec{a}_3$. The orientation of the planes in a solid is defined by the Miller indices h, k and l, which are a sequence of three integer numbers obtained by taking the reciprocals of the intercepts of the plane with the crystal axes. These indices identify families of parallel planes in the crystal structure. In crystallographic notation, Miller indices are enclosed in different types of brackets to denote distinct crystallographic elements: round brackets (hkl) indicate a specific set of lattice planes, while angle brackets $\langle hkl \rangle$ denote a crystallographic direction perpendicular to those planes.

For crystals having a cubic unit cell with side a_0, the distance between planes is given by:

$$d = \frac{a_0}{\sqrt{h^2 + k^2 + l^2}}$$

The condition for constructive interference is given by Bragg's Law (see Equation 2.9): it is satisfied when the path difference between X-rays reflected from successive planes is equal to a integer multiple of the wavelength $n\lambda$.

X-ray diffraction can be performed in two main geometries:

1. Bragg (reflection) geometry: the incident wave is reflected and the diffracted wave exits the solid from the same surface of incidence; the planes in the solid are parallel to the surface.

2. Laue (transmission) geometry: the wave passes through the crystal exiting from the opposite surface; the planes of the crystal are typically perpendicular to the crystal's surface.

These two geometries are shown in Figure 2.5.

As previously mentioned, SKES setups employ Laue-type crystals and therefore operate in transmission geometry. If the planes are perpendicular to the crystal surface, but tilted by an angle χ with respect to the surface normal, it is referred to as the asymmetric Laue case and the angle χ is called asymmetry angle.

Energy calibration

As noted before, the X-ray photons diffracted by the crystal are dispersed in energy along the diffraction plane, meaning that different energies are mapped onto different pixel rows of the detector. Each pixel row therefore encodes the energy information of the captured photons. Establishing an accurate correspondence between pixel rows and their exact energy values is thus essential.

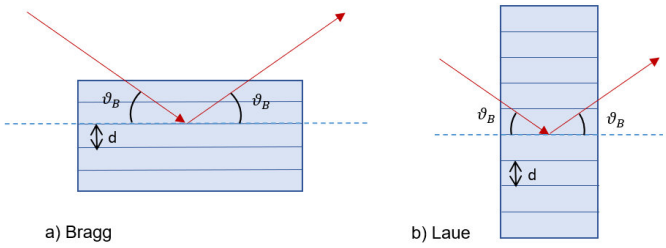

FIGURE 2.5: Bragg and Laue geometries. In the first one, the wave is reflected, thus exits the same surface it entered from. In the second one, the wave is transmitted through the crystal and is diffracted through the opposite surface.

This calibration can be done by using an analytical equation which requires the knowledge of the geometry of the crystal-detector system and the position of the K-edge in the image. In this way, the energy-position information for every pixel in the diffraction plane can be determined. An example of two X-ray images of some cuvettes filled with different contrast media is shown in Figure 2.6.

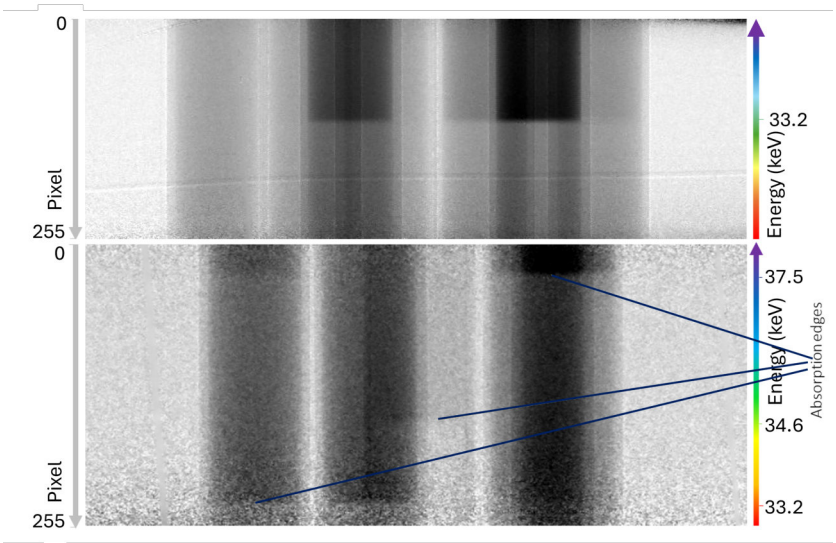

FIGURE 2.6: Top: projection image of 7 plastic cuvettes filled with different dilutions of water and iodine. Iodine's K-edge, at 33.2 keV, is clearly visible at around the center of the image. Bottom: projection image of 4 plastic cuvettes filled with dilutions of water with iodine or barium, and one plastic cuvette filled with xenon. The K-edges of iodine, barium, and xenon, at 33.2 keV, 34.6 keV, and 37.5 keV respectively, are clearly visible at different vertical positions of the image.

The equation that relates the energy of the X-ray photons to the i-th pixel on the detector is given by:

$$E_i = \frac{hc}{2d_{hkl}sin\left(\theta_K + \frac{1}{2}tan^{-1}\left(\frac{y_i - y_K}{d_{fd}}\right)\right)} \tag{2.10}$$

where E_i is the energy at the i-th pixel of the detector, h is the Planck constant, c is the speed of light, d_{hkl} is the d-spacing of the

crystal, θ_K is the Bragg diffraction angle of the X-rays at the K-edge energy, d_{fd} is the focus-to-detector distance, y_K is the detector pixel location of the K-edge energy and y_i is the i-th detector pixel location. For a known K-edge energy E_K, the Bragg angle θ_K is given by the following formula:

$$\theta_K = asin\left(\frac{hc}{2E_K d_{hkl}}\right) \tag{2.11}$$

In cases where two K-edges are within the field of view, the previous analytical equation can be modified to remove the explicit dependence on the focus-to-detector distance, resulting in:

$$E_i = \frac{hc}{2d_{hkl}sin\left(\theta_K + \frac{1}{2}tan^{-1}\left(\frac{(y_i - y_K)tan(2\theta_{K'} - 2\theta_K)}{y_{K'} - y_K}\right)\right)} \tag{2.12}$$

where $y_{K'}$ is the location of the pixel of the second K-edge. The geometry behind Equations 2.10 and 2.12 is shown in Figure 2.7.

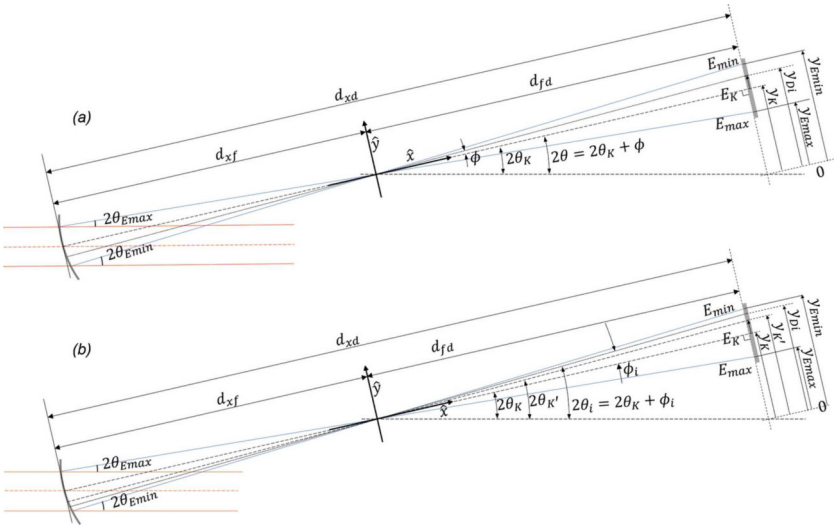

FIGURE 2.7: The geometry for relating the pixel positions on the detector to their energy values with (a) one reference energy and (b) two reference energies. [Qi et al. 2021]

Energy bandwidth

Energy bandwidth is a fundamental parameter in crystal-based spectral imaging, as it ultimately determines both the number and the type of contrast media that can be simultaneously imaged. Once the geometrical and crystal parameters have been fixed, the spectral bandwidth is found to be inversely proportional to the bending radius, whose lower bound (i.e., maximum bending) corresponds to the rupture of the crystal itself:

$$\Delta E = E_K \cot(\theta_B)\, \sigma \left(\frac{F_1}{R\cos(\chi \pm \theta_B)} + 1\right) \tag{2.13}$$

where θ_B is the Bragg angle, σ is the vertical angular divergence, F_1 is the source to crystal distance, R is the bending radius, and χ is the asymmetry angle.

Considering a flat crystal, i.e. $R \rightarrow \infty$, the energy dispersion can be rewritten as:

$$\frac{\Delta E}{E_K} = \frac{\Delta \theta}{tan\theta}$$

where $\Delta\theta$ corresponds to the divergence of the beam σ. This equation can be easily obtained from the Bragg equation.

The original work introducing the SKES by [Zhu et al. 2014] reported a small energy bandwidth of 0.56 keV. These results were obtained by employing the (311) reflection of a 600 μm thick Si crystal curved to a 1 m bending radius.

More recently, [Bassey et al. 2016] reported an exceptionally wide bandwidth reaching 15.0 keV using the (111) reflection of a 600 μm thick crystal curved to 1 m bending radius. As shown in Equation 2.13, the energy bandwidth scales linearly with the beam divergence. In this case, the extreme bandwidth was achieved by exploiting the horizontal divergence of the beam (order of 10^{-3} rad), which in bending magnet sources is one order of magnitude larger than the vertical divergence (order of 10^{-4} rad). However, using the higher divergence for energy dispersion implies that the smaller divergence is used for imaging. As a result, the useful field of view (FOV) for imaging is determined by the smaller vertical divergence, yielding only ∼6 mm. A FOV this small does not allow, for instance, to perform tomographic imaging of large samples (e.g., small animal studies).

Conversely, the ∼5 keV bandwidth reported in one of my previous papers [Perion et al. 2024b], was obtained employing the (111) reflection of a 600 μm thick Si crystal curved to a 1 m bending radius. The bandwidth was obtained across the vertical direction, using the small beam divergence for energy dispersion and exploiting the larger horizontal divergence for imaging. This configuration guaranteed a large FOV (50 mm in the work, which can reach 150 mm at the SYRMEP beamline): this is largest energy bandwidth reported so far over a several centimeter FOV, making the system suitable for biomedical imaging applications.

Focus dimension

Monochromator crystals are placed in the path of a polychromatic X-ray beam to selectively diffract specific wavelengths. When bent, such crystals can yield focusing, increased energy bandwidth or increased flux.

In Bent Laue diffraction, a polychromatic X-ray beam passes through the crystal, the resulting beam converges in a focus. The focal properties of the bent crystal generate two distinct foci: a geometric focus, which arises from the overall curvature of the lattice, and a single-ray focus, appearing from the intersection of each ray with the crystal, which generates a fan of focusing diffracted rays. These are illustrated in Figure 2.8. In both cases, the crystal curvature makes the planes have different angles with respect to the beam, so according to Bragg's law each ray will be diffracted differently.

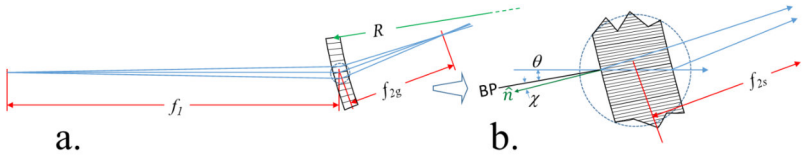

FIGURE 2.8: Bent Laue crystal focusing. (a) Geometric focusing: the source at a distance f_1, the Laue crystal is bent with radius R, and the focus is generated at distance f_{2g}. (b) Single-ray focus caused by diffraction of a polychromatic beam at an angle θ relative to the Bragg planes. [Qi et al. 2021]

Typically, these two foci do not coincide with each other. It has been reported that both the energy resolution and the focal size are optimized when the geometric focus and the single-ray focus match [Qi et al. 2021]. This is known as *magic condition*.

Because the beam focuses onto a line, only a thin line of the sample is acquired in a single image acquisition. In order to build a complete image, the sample must be scanned vertically. The size of the focus S_f is given by [Qi et al. 2021]:

$$S_f = \left[\left(\frac{q_G S^2}{f_1}\right) + \frac{W^2}{12}\right]^{\frac{1}{2}} \tag{2.14}$$

Here, S is the size of the source, q_G is the crystal's focal distance, and W is the spread of the nearly parallel diffracted rays.

The focal size defines the vertical spatial resolution of the final reconstructed image of the sample. For this reason, achieving the *magic condition* is critical, as it minimizes the focal size and maximizes the imaging performance of the system.

Magic condition

When using bent Laue crystals, reaching the magic condition is essential for the optimization of both spatial resolution and energy resolution. When a Laue-type crystal is bent around an axis perpendicular to the diffraction plane, parallel X-rays incident on the convex side of the crystal will be focused on the concave side of the crystal. This effect is analogous to a lens but with a modified focal equation given by [Samadi et al. 2016]:

$$\frac{cos(\chi \mp \theta)}{f_{2g}} - \frac{cos(\chi \pm \theta)}{f_1} = \frac{2}{R}$$

where χ is the asymmetry angle, θ is the angle of the incident beam with respect to the lattice planes (Bragg angle), f_1 and f_{2g} are defined as in Figure 2.8 and R is the bending radius. The signs indicate the location of the Bragg planes in relation to the source and focus locations. If the Bragg planes are between the source and focus the upper sign is used, otherwise, the lower sign is used. Thus the geometric focus can be expressed by the following equation:

$$f_{2g} = \frac{R\, f_1 cos(\chi \mp \theta)}{2f_1 + R\, cos(\chi \pm \theta)}$$

On the other hand, an infinitesimally small polychromatic beam that meets the crystal produces a fan beam on the exit surface (Borrmann fan, Figure 2.8.b). The generated focus f_{2s} can be real or virtual and is given by:

$$\frac{f_{2s}}{R} = \pm \frac{sin(2\theta)}{2sin(\chi \pm \theta) + (1+\nu)sin(2\chi)cos(\chi \pm \theta)}$$

where ν is the Poisson ratio for the crystal type and orientation [Greaves et al. 2011]. A simple equation links the asymmetry angle χ to the Bragg angle θ under the assumption that the source-crystal distance is large ($f_1 >> f_{2g}$) and the Bragg angle is small ($\theta << 1$). The latter is satisfied when high photon energies are considered. The equation states:

$$\chi_{magic} \simeq \frac{\theta}{2+\nu}$$

When the magic condition is satisfied, diffracted X-rays form a perfect fan beam.

In summary, the magic condition ensures that the geometric and single-ray foci coincide, optimizing both spatial and energy resolution. Carefully selecting the asymmetry angle χ based on this condition allows for high-resolution SKES imaging.

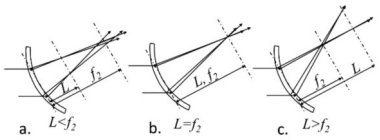

Figure vii: L is the single-ray focus while f_2 is the geometrical focus. (a) $L < f_2$, (b) $L = f_2$ (magic condition), (c) $L > f_2$. Figure taken from [Samadi et al. 2016]

2.2 PHASE-CONTRAST METHODS

Phase-contrast X-ray imaging detects the phase shifts that occur in X-rays as they traverse matter. Unlike conventional absorption-based X-ray imaging, phase-contrast offers higher visibility of low-absorbing materials, such as soft tissues, as it is sensitive to the small variations in the refraction index.

As discussed in the previous chapter, the index of refraction of X-rays is complex and can be expressed as $n = 1 - \delta + i\beta$: the refractive decrement δ is typically three orders of magnitude greater than the imaginary part β, making the effects due to phase shift generally more relevant than those due to absorption. For this reason, phase-contrast imaging provides significantly enhanced contrast, especially in regions where conventional absorption imaging fails to distinguish between materials with similar attenuation coefficients.

Thanks to the availability of high-brilliance synchrotron sources and, more recently, advanced X-ray laboratory sources, it has become routine to observe and exploit refraction and interference phenomena in X-ray fields. As a consequence, X-ray phase effects in imaging are now effectively used in combination with traditional attenuation effects as they can provide complementary information about a sample's internal structure. The term *differential phase-contrast* is often used in this context to refer to imaging approaches that directly detect the angular deviation of the X-ray beam, corresponding to the gradient of the phase, as defined in Equation 1.12.

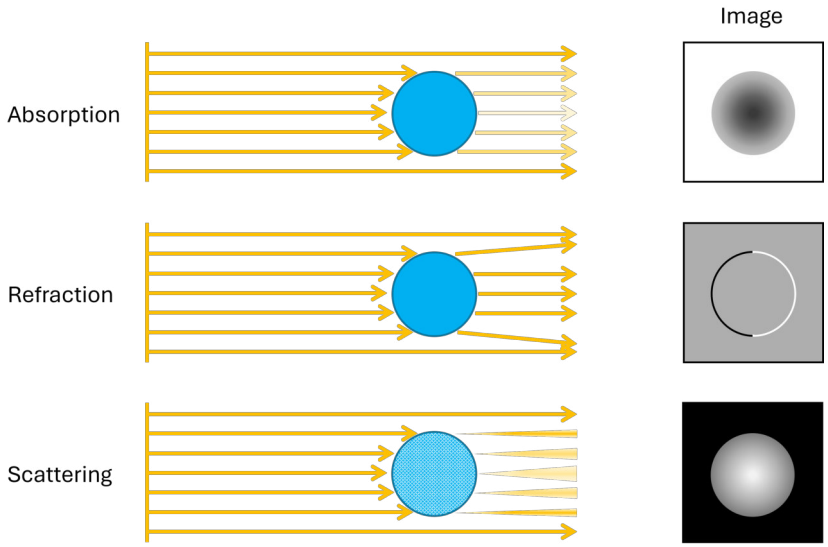

FIGURE 2.9: Absorption imaging (top), and phase-contrast imaging (middle and bottom). The refraction image results from the change in direction of the X-rays due to phase-shift, while the scattering (or dark-field) image arises from multiple small-angle refraction that cause blurring without significantly altering the overall beam direction.

Phase-contrast imaging is particularly valuable in fields such as

biomedical imaging, materials science, and non-destructive testing. Various techniques exist to convert the phase shifts of X-rays into modulations of intensity recorded at the detector.

Among them, *Free-space propagation* is probably the simplest, requiring only an appropriate propagation distance between the sample and the detector to make phase effects detectable [Snigirev et al. 1995; Wilkins et al. 1996]. Another method is synchrotron-based *Analyzer-based imaging*. This approach employs two crystals: the first serves as monochromator and collimator, while the second acts as an angular filter that translates phase-induced deviations into intensity modulations [Chapman et al. 1997]. *Grating-based methods* use periodic structures to encode and analyze the X-ray wavefront. Initially developed at synchrotron facilites using two gratings [Clauser and Reinsch 1992], this method has been extended to low-brilliance sources by adding a third grating [Pfeiffer et al. 2006]. Another category of X-ray phase-contrast imaging techniques is based on the use of structured illumination to extract information about absorption, refraction, and dark-field, these are referred to as *tracking-based methods*. A known pattern, such as an absorption grid [Vittoria et al. 2015b] or a speckle pattern [Morgan et al. 2012] is imposed on the beam. Phase shifts introduced by the sample distort the pattern, while absorption reduces the overall intensity of the pattern. By tracking these modifications, it is possible to recover absorption and refraction images. These approaches can have two-dimensional sensitivity [Wen et al. 2010] and can be sensitive to dark-field signals [Berujon et al. 2012]. When the detector pixel size is too large to directly resolve the imposed pattern, the *edge illumination* method can be employed [Olivo and Speller 2007]. This technique uses two absorbing masks: a sample mask that divides the beam into beamlets and a detector mask that creates insensitive regions between adjacent pixels, and it is particularly well suited for incoherent and polychromatic X-ray sources.

In this thesis, the phase-contrast imaging techniques that I used during my PhD will be described: propagation-based phase-contrast, and tracking-based methods using absorption grids or speckle patterns.

2.2.1 *Propagation-based*

Propagation-based imaging is the most used technique in synchrotrons and the simplest phase-contrast method, as it only requires a source, a sample, and a detector. The key requirements for this technique are sufficient sample-to-detector distance and high lateral coherence of the beam, meaning that the amplitude of the waves must be highly correlated in the direction perpendicular to the beam propagation. This requirement makes this technique particularly suited for synchrotron setups.

As anticipated in Chapter 1, variations in thickness and refractive index within a sample lead to a change in the shape of an X-ray wavefront. By recording the intensity of the wavefront at sufficient distance from the sample, the wavefront distortions are converted into detectable intensity variations due to Fresnel diffraction (see Figure 2.10). By analyzing the resulting intensity pattern at the detector plane, information about the phase of the object can be retrieved.

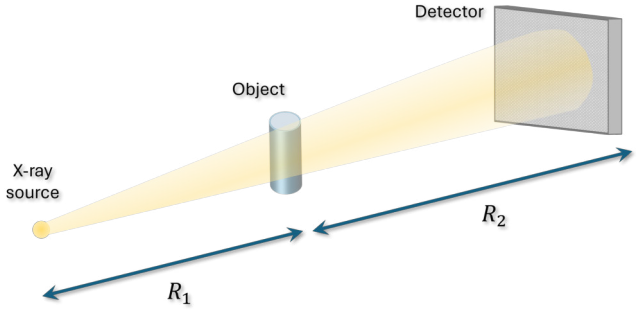

FIGURE 2.10: Sketch of a propagation-based imaging setup.

A rigorous treatment of this phenomenon requires a wave-optical approach. This leads, for a pure phase object and assuming a point source, to the following expression [Wilkins et al. 1996]:

$$I(x,y,M,\lambda) = \frac{I_0}{M^2}\left[1 + \frac{R_2\lambda}{2\pi M}\nabla_\perp^2\phi(x,y,R_1,\lambda)\right] \tag{2.15}$$

where R_2 is the sample-to-detector distance, and $M = (R_1+R_2)/R_1$ is the magnification, with R_1 being the source-to-sample distance. The phase-contrast vanishes when $R_2 \to 0$, which is the typical condition for conventional radiography.

In practice, most samples are not purely phase objects, they also attenuate the beam to some extent. As a result, the intensity projection image will contain a mixture of both absorption and phase shift. The process of separating and quantitatively recovering the phase and amplitude at the exit surface of the sample is known as *phase retrieval*. Since the aim is to recover both absorption and phase, usually more than a single measurement, either at different propagation distances or at different energies, is required unless some constraints are imposed on the sample [Nugent et al. 1996; Gureyev et al. 2001]. Quantitative phase retrieval with a single measurement can be performed by assuming an homogeneous object, which is a reasonable approximation in most cases [Paganin et al. 2002].

2.2.2 *Tracking-based*

Multiple tracking-based techniques exist in phase-contrast imaging. These methods rely on the creation of a radiation field with a well-known structure and tracking its modifications to extract absorption, refraction, and dark-field information. Specifically, absorption is linked to the reduction of the field's intensity, refraction to its displacement in space, and dark-field to its blurring.

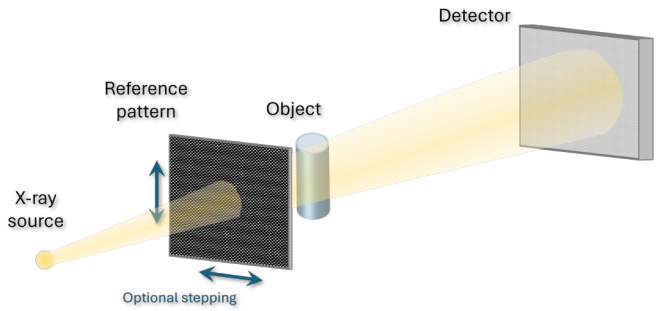

FIGURE 2.11: Sketch of a tracking-based imaging setup.

Figure 2.11 illustrates a typical tracking-based experimental setup. A grid or structured object that produces a known reference pattern is placed in the beam path. First, reference images of this pattern are acquired without the sample. When the sample is inserted, it alters the wavefront, and the resulting pattern is recorded. By comparing the reference and sample images, absorption, phase, and dark-field information can be retrieved. The technique is single shot, although to increase the resolution of the reconstructed image, several pairs of reference/sample images are typically acquired by moving the membrane between each pair of acquisitions.

In this thesis, particular attention will be given to the Beam Tracking and modulation-based/speckle methods which will be described in the following sections.

Modulation-based/speckles

One type of tracking-based approach consists in modulating the beam by introducing randomly distributed intensity patterns. A *speckle* pattern is the random granular pattern that is generated when a coherent beam impinges on an element with a rough surface (such as sandpaper) [Morgan et al. 2012]. Speckle size is an important property of the speckle pattern that affects the quality of the reconstructed images. Since speckles generally have irregular shapes and random distribution of sizes, small, well-defined speckles that cover a few pixels in the detector plane are usually preferred [Zdora 2018].

Recently, alternatives to sandpaper modulators have been explored with the aim of optimizing membrane modulation patterns [Magnin

et al. 2025]. These include the use of structured membranes designed to produce specific hole patterns in different geometries.

The goal in modulation-based imaging is to effectively track how the sample distorts the modulator pattern. To do this, a reference image is initially acquired when only the membrane is present between the source and the detector. Then, the object is added and a second image, called sample image, is acquired. By comparing the two images and analyzing the local distortions of the modulator pattern, information about attenuation, refraction, and dark-field induced by the sample can be retrieved.

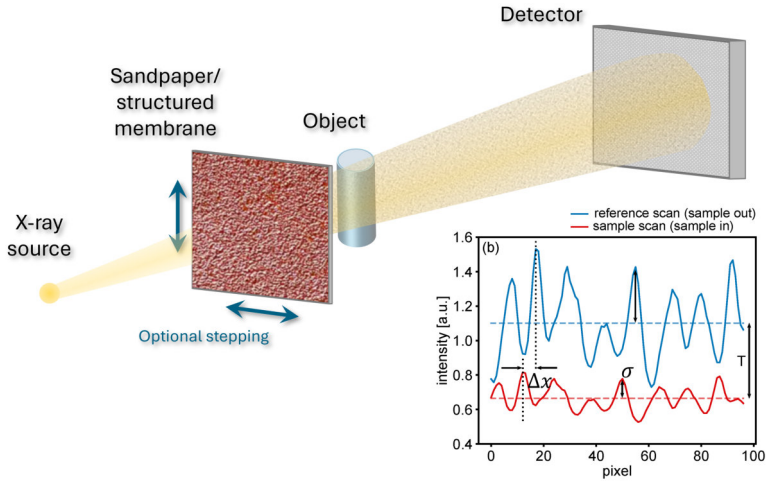

FIGURE 2.12: Sketch of a tracking-based imaging setup with sandpaper as modulator. In the plot, adapted from [Zdora 2018], profile plots of the reference scan (blue) and sample scan (red) are shown.

The advantages of this technique are that it brings no limitations in terms of field of view and spatial resolution (which are governed by the detector), and the relatively simple setup. Although the method is in principle single-shot, the membrane is typically scanned and multiple exposures are recorded to improve spatial resolution.

Modulation-based imaging using speckles usually requires enough transverse coherence to resolve grain structure of the mask, but it is tolerant of low longitudinal coherence. As a result, it is compatible with the polychromatic spectra produced by conventional X-ray tubes. In practice, achieving visible speckle patterns typically requires an X-ray source with a small focal spot, generally below 50 µm [Zanette et al. 2014].

One of the challenges of this approach is the accurate extraction of displacement and dark-field information from the speckle patterns. Several algorithms have been developed to address this, categorized in explicit and implicit tracking methods.

Explicit algorithms directly detect the local displacement of the patterns by comparing small groups of pixels from the reference images and the sample images. This procedure is repeated for each

pixel across the image. An example of explicit tracking algorithm is the *Unified Modulated Pattern Analysis* (UMPA) [Zanette et al. 2014; Zdora et al. 2017], which estimates local displacements by minimizing the local mean squared error of a cost function $\mathcal{L}(x, y)$.

On the other hand, implicit tracking algorithms are based on a mathematical model, assuming the conservation of the optical wave flow. An example of implicit algorithm is the Low Coherence System (LCS) algorithm [Paganin and Morgan 2019; Morgan and Paganin 2019; Quénot et al. 2021]. LCS is based on flux conservation: the model relates the reference and sample images to the absorption I_{obj}, the displacement fields D_x and D_y (representing refraction), and a diffusion term D_f (corresponding to the dark-field signal). The approach is based on the Transport of Intensity equation, which describes the intensity evolution of a paraxial complex coherent scalar wave field as it propagates, expressing local energy conservation [Teague 1983]. Adding a loss term I_{obj} to account for the object's attenuation we get:

$$I_r(x,y) - \frac{I_s(x,y)}{I_{obj}(x,y)} = \nabla[I_r(x,y)D_\perp(x,y)] \tag{2.16}$$

where I_r is the reference image, I_s is the sample image, and $D_\perp = [D_x, D_y]$. This equation becomes the Fokker-Plank equation when completed by a diffusion term D_f:

$$I_r(x,y) - \frac{I_s(x,y)}{I_{obj}(x,y)} = \nabla[I_r(x,y)D_\perp(x,y)] - z_2\nabla_\perp^2[D_f(x,y)I_r(x,y)] \tag{2.17}$$

where z_2 is the sample-to-detector distance. After expanding this equation, the term $I_r(x,y)\nabla D_\perp(x,y)$ is neglected as it describes the interference fringes and the LCS algorithm is designed for low coherent sources. Then the equation simplifies to:

$$I_r(x,y) - \frac{I_s(x,y)}{I_{obj}(x,y)} = D_\perp(x,y)\nabla I_r(x,y) - z_2 D_f(x,y)\nabla_\perp^2[I_r(x,y)] \tag{2.18}$$

In order to solve for the four unknowns (I_{obj},D_x,D_y, and D_f), at least four independent equations are needed. This is typically achieved by acquiring images at at least four different membrane positions, yielding:

$$
\begin{cases}
I_r^{(1)}(x,y) = \dfrac{I_s^{(1)}(x,y)}{I_{obj}(x,y)} + D_x(x,y)\dfrac{\partial I_r^{(1)}(x,y)}{\partial x} + D_y(x,y)\dfrac{\partial I_r^{(1)}(x,y)}{\partial y} \\
\qquad\qquad -z_2 D_f(x,y)\nabla_\perp^2[I_r^{(1)}(x,y)] \\
I_r^{(2)}(x,y) = \dfrac{I_s^{(2)}(x,y)}{I_{obj}(x,y)} + D_x(x,y)\dfrac{\partial I_r^{(2)}(x,y)}{\partial x} + D_y(x,y)\dfrac{\partial I_r^{(2)}(x,y)}{\partial y} \\
\qquad\qquad -z_2 D_f(x,y)\nabla_\perp^2[I_r^{(2)}(x,y)] \\
I_r^{(3)}(x,y) = \dfrac{I_s^{(3)}(x,y)}{I_{obj}(x,y)} + D_x(x,y)\dfrac{\partial I_r^{(3)}(x,y)}{\partial x} + D_y(x,y)\dfrac{\partial I_r^{(3)}(x,y)}{\partial y} \\
\qquad\qquad -z_2 D_f(x,y)\nabla_\perp^2[I_r^{(3)}(x,y)] \\
I_r^{(4)}(x,y) = \dfrac{I_s^{(4)}(x,y)}{I_{obj}(x,y)} + D_x(x,y)\dfrac{\partial I_r^{(4)}(x,y)}{\partial x} + D_y(x,y)\dfrac{\partial I_r^{(4)}(x,y)}{\partial y} \\
\qquad\qquad -z_2 D_f(x,y)\nabla_\perp^2[I_r^{(4)}(x,y)]
\end{cases}
$$

where $I_r^{(i)}$ and $I_s^{(i)}$ are the reference and sample images of the i-th membrane position. Solving the system allows for the retrieval of absorption, refraction and dark-field signals.

Beam Tracking

The beam tracking technique uses a structured absorbing mask, placed in the X-ray beam, to shape it into an array of narrow beamlets, each featuring a width that can range from 1 to tens of micrometers [Vittoria et al. 2015a]. A key requirement is that the absorbing regions of the mask attenuate the beam completely, ensuring that only the beamlets transmitted through the apertures contribute to the detected signal. After exiting the mask, the beamlets propagate and reach the detector, where their intensity distribution is mapped. When a sample is introduced into the beam, it modifies the beamlets' profiles in terms of intensity, spatial shift, and broadening. These changes correspond, respectively, to absorption, refraction (proportional to the gradient of the phase shift), and ultra-small-angle scattering (dark-field). To accurately capture these effects, the technique requires a high-resolution detector with a pixel size smaller than 10 µm, unless geometric magnification is used to effectively increase the sampling resolution.

Two important mask parameters are the width of the mask aperture (corresponding to the beamlet width), called *aperture*, and the distance between one beamlet and the other, called *period*.

The effects of absorption, refraction, and dark-field on the recorded intensity profiles can be mathematically formulated as:

$$I(x) = TI_0(x - \delta x) * s(x)$$

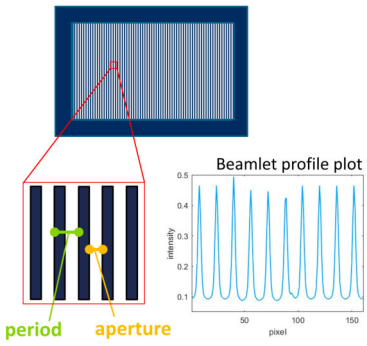

Figure viii: One-dimensional absorbing mask (top), detail of the mask (bottom left), and horizontal profile plot of a mask image (bottom right).

where I and I_0 are the beamlet intensities acquired with and without the sample, respectively, T is the transmission (absorption effect), δx is the lateral shift of the beamlet due to refraction, and $s(x)$ is a scattering function which accounts for the effect of dark-field. Each beamlet is detected and analyzed independently, and is modeled as a Gaussian function:

$$f(x) = A\frac{1}{\sqrt{2\pi}\sigma}e^{-\frac{(x-\mu)^2}{2\sigma^2}}$$

Here, A is the amplitude, μ is the beamlet center (related to refraction), and σ is the standard deviation (related to dark-field). These parameters can be calculated either by fitting a Gaussian curve to the beamlet profile, which provides high accuracy but is computationally intensive, or by computing the moments (centroid and variance) of the profile, which is faster and less resource demanding, although potentially less robust in low signal-to-noise conditions. The beamlet is modeled as a Gaussian function because its intensity distribution results from the convolution of the finite source size, mask apertures, and detector point spread function, which collectively lead to an approximately Gaussian profile under typical experimental conditions. The transmission is computed as the ratio $I(x)/I_0(x)$ between the integrals of the Gaussians with and without the sample. The beamlet displacements on the detector plane are related to the refraction angles through:

$$\Delta\alpha = tan^{-1}\frac{\Delta x}{z}$$

where Δx is shift of the beamlet calculated from parameter μ, and z is the sample-to-detector distance. As previously discussed, this angle is proportional to the first derivative of the phase shift.

To achieve full sample illumination, the mask is scanned in small increments, smaller than its period, in a process known as *dithering*. The step size usually corresponds to the mask's aperture width, which ultimately defines the system's effective spatial resolution [Lioliou et al. 2023]. As a result, the final resolution is not governed by the detector pixel size but by the number of mask steps, with the resolution being equal to the mask aperture when the mask is stepped by half the aperture width [Esposito et al. 2022].

To ensure complete illumination of the sample, the mask is translated in small increments—smaller than its period—in a process known as dithering. The step size is typically set by the mask aperture width, which ultimately determines the system's effective spatial resolution [Lioliou et al. 2023]. Consequently, the final resolution is governed not by the detector pixel size but by the mask stepping scheme. When the mask is stepped by half the aperture width, the maximum achievable resolution equals the aperture size itself.

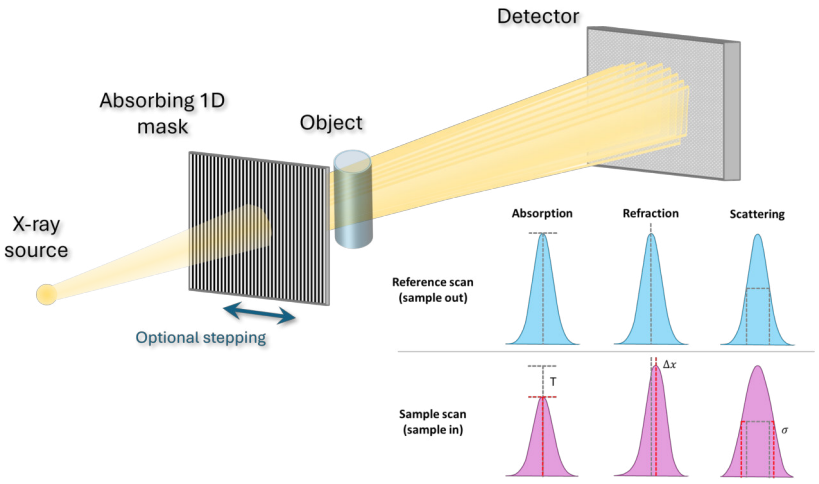

FIGURE 2.13: Sketch of a tracking-based imaging setup with an absorbing membrane as modulator. On the bottom right, beamlet profiles with no sample (blue), and beamlet profile changes due to absorption, refraction, and dark-field (pink) are shown.

If a reference mask with two-dimensional features (i.e., structured in both horizontal and vertical directions) is used, differential phase-contrast can be extracted in both directions from a single exposure. In this thesis, however, only one-dimensional beam tracking measurements will be discussed.

Beam tracking is an accessible phase-contrast technique: it is compatible with both coherent and conventional polychromatic X-ray sources, and it enables quantitative imaging of refraction, which can relate directly to electron density. Differently from other phase-contrast techniques, beam tracking directly measures beamlet displacement and broadening, avoiding reliance on approximated mathematical models. On the other hand, it has its limitations, including mask fabrication which can be expensive, and spatial resolution which is limited to the mask's aperture size.

2.3 SPECTRAL PHASE-CONTRAST IMAGING

In the last two sections, spectral X-ray imaging and phase-contrast X-ray imaging have been discussed individually and in detail. In this section, the advantages of combining these two techniques are addressed.

It has already been covered how conventional absorption-based X-ray imaging methods can fail to provide sufficient contrast when different structures inside an object are similarly attenuating, such as in soft tissues. To overcome this limitation, high-Z contrast elements can be introduced to selectively enhance the contrast of regions of interest. Spectral X-ray imaging takes advantage of the energy dependence of high-Z elements, whose mass attenuation coefficient exhibits a sharp rise at their K-edge. By acquiring images at two or more energies above and below the K-edge of the contrast element, spectral imaging allows material-specific discrimination and quantification through spectral decomposition [Alvarez and Macovski 1976]. In contrast, X-ray phase-contrast imaging detects the phase shifts in X-rays as they traverse matter. Unlike conventional absorption-based X-ray imaging, this technique offers higher visibility of low-Z materials, such as soft tissues, as it is sensitive to their refraction properties.

It is clear how these two imaging modalities provide complementary information: spectral imaging providing high-Z material specificity and phase-contrast imaging discriminating among low-Z materials. Their integration can enhance material discrimination by benefitting from the strengths of the individual methods while mitigating their weaknesses.

There are only a few reported examples of spectral phase-contrast imaging in the literature. Among them, [Mechlem et al. 2019] investigate the combination of grating-based phase-contrast with spectral detectors through a numerical simulation. Their results show that incorporating phase shift information leads to highly reduced basis material image noise levels compared to conventional spectral X-ray imaging. Additionally, the extraction of information about the microstructure via the dark-field image can be beneficial for clinical diagnosis. [Schaff et al. 2020] perform propagation-based phase-contrast imaging at two monochromatic energies at the synchrotron. [Ji et al. 2020] employ a dual-energy differential phase-contrast CT system, combining a grating interferometer with a photon counting CT scanner with two energy bins. They compare this scan with a triple spectra CT scan, showing that the combination of the two techniques correctly differentiates the bone structure, iodine, and the soft tissue in the biological samples with a much lower quantification noise. Finally, in a study I contributed to, we report the first integration of spectral phase-contrast in a tomographic edge-

illumination setup. Applied to a test phantom and an ex-vivo murine model perfused post-mortem with an iodine-based contrast agent, the study demonstrates the advantages of this integration showing that the signal-to-noise ratio in the soft tissue channel is 9 times greater compared to a conventional spectral algorithm [Brombal et al. 2024].

This chapter concludes with the theoretical formulation of the spectral material decomposition algorithm extended to account for phase information, which is presented in the following section.

2.3.1 *Spectral-Phase decomposition algorithm*

In Section 1.2 the complex index of refraction for X-rays was introduced as:

$$n = 1 - \delta + i\beta \tag{2.19}$$

where δ is the *refractive index decrement*, and β is the *absorption index*. These quantities can be expressed as:

$$\beta = \frac{\mu}{2k} \qquad \delta \approx r_0 \rho_e \lambda^2 / 2\pi \tag{2.20}$$

The expression for δ is an approximation that holds for forward scattering and when the photon energy is sufficiently far from the absorption edges. A more complete description requires the atomic form factor to be taken into account. Here, δ is directly proportional to the electron density ρ_e, while β is related to the linear attenuation coefficient μ. Consequently, absorption measurements provide information about a material's attenuation properties which is linked to its effective atomic number, whereas phase measurements are directly linked to its electron density.

As previously discussed in Section 2.1.2, material discrimination and quantification can be achieved through decomposition algorithms. The same linear decomposition formalism applied to the attenuation coefficient μ in spectral imaging can be extended to the phase component δ. Specifically, the phase signal can be represented as a linear combination of mass-specific refractive index decrements for a given basis set of materials:

$$\delta = \sum_i \rho_i \left(\frac{\delta}{\rho}\right)_i \tag{2.21}$$

Thus, the material decomposition framework can be expanded to include phase information alongside spectral data. The system of equations becomes:

$$\begin{pmatrix} S^{high} \\ S^{low} \\ S^{phase} \end{pmatrix} = \begin{pmatrix} \frac{\mu}{\rho}\Big|_1^{high} & \frac{\mu}{\rho}\Big|_2^{high} & \frac{\mu}{\rho}\Big|_3^{high} \\ \frac{\mu}{\rho}\Big|_1^{low} & \frac{\mu}{\rho}\Big|_2^{low} & \frac{\mu}{\rho}\Big|_3^{low} \\ \frac{\delta}{\rho}\Big|_1 & \frac{\delta}{\rho}\Big|_2^{low} & \frac{\delta}{\rho}\Big|_3^{low} \end{pmatrix} \begin{pmatrix} \rho_1 z_1 \\ \rho_2 z_2 \\ \rho_3 z_3 \end{pmatrix} \tag{2.22}$$

Here, the incorporation of a third input (i.e. the phase image) allows for the decomposition of three distinct materials. It is important to note that while the energy dependence of δ differs from that of μ, it is nearly identical across different materials. As a result, the inclusion of a single phase measurement contributes a linearly independent row to the decomposition matrix. However, incorporating additional phase measurements at different energies would yield rows that are approximately linearly dependent, limiting their contribution to the decomposition matrix.

Part II

METHODS AND DEVELOPMENT

3

Laboratory-based Spectral and Phase-Contrast Imaging

In this chapter, laboratory-based measurements performed during my PhD are presented. The measurements are based on the techniques introduced in the previous chapters.

Section 3.1 focuses on spectral imaging using an energy-resolving detector, carried out at the PEPI laboratory at INFN Trieste [Brombal et al. 2023], with part of the work published in [Perion et al. 2024a]. These experiments were conducted to evaluate the ability of the system to perform quantitative multiple-material spectral decomposition.

Section 3.2 describes phase-contrast imaging experiments performed at Xenocs SAS in Grenoble, France, during my six-month PhD stay at the STROBE laboratory, University of Grenoble. The study consisted of optimizing the motion of membranes in phase-contrast imaging. The results of this work are submitted for publication in Physical Review A.

3.1 SPECTRAL IMAGING WITH LABORATORY SOURCE AND ENERGY-RESOLVING DETECTOR

All measurements described in this section were performed at the PEPI laboratory of INFN Trieste.

PEPI laboratory

The PEPI (Photon-counting Edge-illumination Phase-contrast imaging) laboratory is a compact multi-modal imaging setup, which enables both X-ray phase-contrast imaging with edge illumination technique and spectral imaging through a chromatic detector [Brombal et al. 2023]. The system enables multiple imaging modalities: among

these, spectral micro-tomography has been used for the measurements described in this thesis.

The X-ray source is a Hamamatsu micro-focus tube operating at voltages from 40 to 100 kV and currents between from 10 to 200 µA. The maximum power output is 20 W, and the X-ray focal spot size ranges between 5 to 30 µm scaling linearly with power.

The detector in the laboratory is Pixirad-1/Pixie-III, which is a large-area direct detection photon-counting device. This detector is built with a hybrid architecture, where a high-Z sensor is coupled to the ASIC (Application Specific Integrated Circuit) through the flip-chip bonding technique [Bellazzini et al. 2015]. The CdTe sensor is a 650 µm thick Schottky type diode. The active area is of 32 mm^2 × 25 mm^2 and the chip is organized as a matrix of 512 s × 402 square pixels at 62 µm pitch. The detector features two independent energy thresholds allowing the acquisition of two images over different energy bins in a single shot, therefore enabling spectral imaging. When two thresholds are applied, events are counted in the first counter if their energy falls inside the window defined by the lower and the upper threshold. Instead, they are counted into the second counter if their energy is higher than the upper threshold. The Pixirad-1/Pixie-III detector is sensitive in a broad energy range (from 2 to 100 keV), features a high frame rate (around 100 fps), a high detection efficiency (high-Z sensor) and a good energy resolution (between 3 and 4 keV). Relevant system specifications are summarized in Table 3.1.

TABLE 3.1: PEPI laboratory specifications.

X-ray source	Spectrum (kVp)	40-100
	Power (W)	20 (maximum)
	Focal Spot (µm)	5-30
Detector	Pixel size (µm)	62
	Field of View (pixels)	512x402
	Sensor (µm)	650, CdTe
	Dimensions (cm)	50-120
Geometry	Magnification	1.3-2.8
	Resolution (PSF) (µm)	20-50

3.1.1 *Multiple-energy-bin micro-CT for gold and iodine detection*

Parts of this section are adapted from my previously published conference contribution [Perion et al. 2024a].

This study demonstrates spectral micro-CT imaging using a multiple-energy-bin approach, performed at the PEPI laboratory of INFN Trieste. The measurement involved multiple scans, each using a different energy threshold which was optimized for the discrimination of iodine and gold.

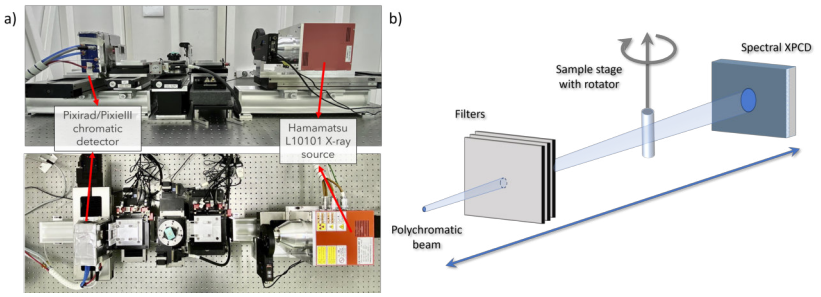

FIGURE 3.1: Schematic representation of the experimental setup implemented at the PEPI laboratory.

As anticipated in the previous chapters, high-atomic-number contrast agents enhance the visibility of specific tissues or structures in the body. Their attenuation profiles exhibit a distinct dependence on energy, characterized by sudden increases of absorption at K-edges, making them suitable for spectral imaging purposes [Roessl and Proksa 2007]. Specifically, iodinated contrast media are the most commonly used in cardiovascular imaging [Hallouard et al. 2010], while gold nanoparticles are emerging as a CT contrast agent due to their high X-ray absorption, low toxicity, high biocompatibility, and their specificity in targeting tumors [Hainfeld et al. 2006; Sousa et al. 2010; Menk et al. 2011].

To explore this potential, a sub-100 µm resolution spectral micro-CT scan was performed on a test sample using multiple energy thresholds. The results demonstrate the feasibility of multi-material decomposition, holding potential for improving material detectability and quantification in a range of pre-clinical applications, including cardiovascular and oncologic imaging.

Data acquisition and reconstruction

The images were acquired through multiple acquisitions in 5 energy bins defined by the applied energy thresholds. These were chosen at 26, 33, 42, 70 and 92 keV (see Figure 3.2(a)). A CT scan of the object, in a 1.3 cm^3 × 1.8 cm^3 × 1.4 cm^3 volume, was acquired with 720 projections over 360°, for a total scan time of 75 minutes per energy bin. The sample consisted of three plastic cuvettes, filled with water, a calcium salt ($CaCl_2$) and a 50 $mg\,mL^{-1}$ iodine dilution, all inserted in a spool of 25 µm-thick gold wire, as visible in Figure 3.2(b). The magnification factor was 1.8, reducing the effective voxel size down to 35 µm.

A detector-specific pre-processing procedure and an image-denoising technique [Di Trapani et al. 2022] were applied to the projection images before tomographic reconstruction. The images were then processed through the material decomposition algorithm described in Section 2.1.3 to obtain independent distributions of each chosen

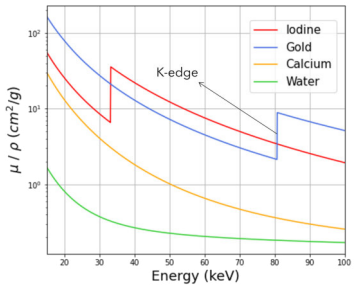

Figure ix: Mass attenuation coefficients of iodine, gold, calcium and water.

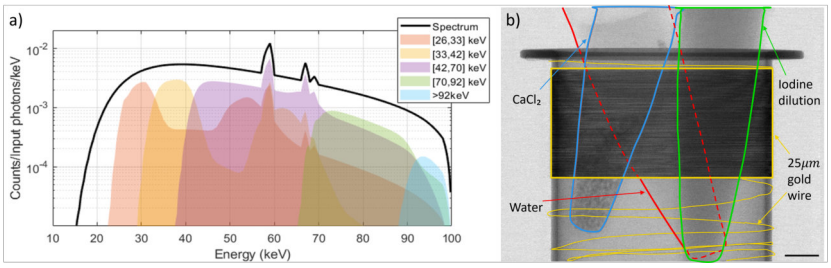

FIGURE 3.2: a) Simulated X-ray spectrum at 100 kVp voltage (black line). The energy thresholds were set at 26, 33, 42, 70 and 92 keV. These delimit the shaded regions, which correspond to the fraction of photons in each energy bin. b) X-ray projection of the sample composed of three plastic cuvettes, filled with water, a calcium salt and an iodine dilution respectively, all inserted in a spool of gold wire.

material. Each mass attenuation coefficient was integrated over the energy spectrum $w(E)_i$ and the detector energy response $D(E)_i$ in the specific bin, both derived from detector characterization measurements and Geant4-based simulations [Brombal et al. 2022; Di Trapani et al. 2020].

Results and discussion

A four-element material decomposition was applied to the reconstructed slices. Notably, the results demonstrate the successful separation of iodine, gold, calcium and water into four distinct maps, with minimal cross-contamination between channels, as shown in Figure 3.3.

It is important to note that all decomposition images are quantitative, as indicated by the colour bars in Figure 3.3. The density of the elements was determined by selecting a circular region of interest (ROI) inside each cuvette and by measuring its mean intensity. The uncertainty associated with each measurement was calculated as the standard deviation within the chosen ROI. Water and iodine inside the cuvettes are accurately quantified, with a relative error of 6.8 % for iodine and of 2 % for water. Measurement results are reported in table 3.2. The actual density of calcium is unknown because it was not diluted in water, and the density of gold could not be assessed as the gold wire diameter is smaller than the voxel size of the imaging system.

TABLE 3.2: Expected and measured densities of iodine, water, and calcium inside the cuvettes.

	expected	measured
Iodine (mg/mL)	50	46.6 ± 1.3
Water (mg/mL)	1000	1020 ± 115
Calcum (mg/ml)	-	134.6 ± 44.6

The material decomposition into calcium failed to accurately localize the element when it was surrounded by gold (see Figure 3.3,

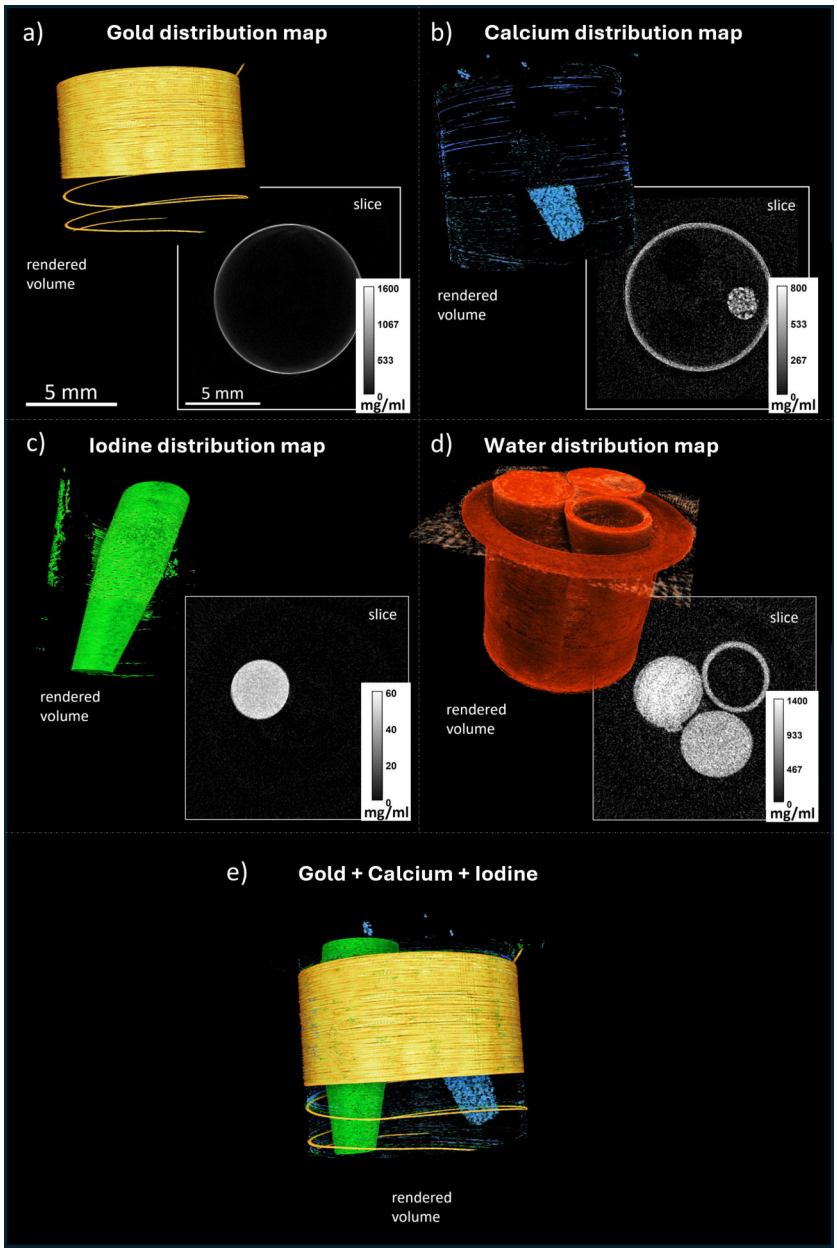

FIGURE 3.3: a), b), c), and d): 3D rendered volumes along with single tomographic slices of gold, calcium, iodine, and water decompositions, respectively. e) 3D rendered volume of gold, calcium and iodine together.

top right). This is likely due to beam hardening effects introduced by the gold wire, which, owing to its high atomic number and strong attenuation, significantly alters the X-ray spectrum and affects the measured absorption. This lead to an underestimation of calcium density in regions near the gold wire.

In contrast, iodine decomposition was more robust in the presence of gold. Although the decomposition exhibited an increase in noise in this region, the high absorption of iodine and the presence of its K-edge allowed for a more precise localization and quantification of the element.

3.1.2 *Dual-energy-bin micro-CT for iodine detection*

A whole-body atlas of a murine model using spectral X-ray micro-CT was performed at the PEPI laboratory of INFN Trieste. The goal of the experiment was to map both the bone structure and the iodine-perfused organs to evaluate the feasibility of a subsequent dissection. The dissection was later performed at the Cattinara Hospital in Trieste, where multiple organs were extracted and subsequently transported to the ESRF synchrotron in Grenoble for further measurements. The analysis demonstrated successful discrimination between iodine and bone, allowing a high-resolution visualization of the vascular structure of the murine model at a voxel size of 38 µm.

Data acquisition and reconstruction

The following description of the sample is adapted from [Brombal et al. 2024]. The sample was an ex vivo 7 week old female athymic nude mouse (Charles River Laboratories, Wilmington, MA, USA), that received post-mortem perfusion with μAngiofil® (Fumedica AG, Muri, Switzerland), a polymerizing iodine-based vascular contrast agent. The mouse was euthanized and afterwards perfused with warm dPBS and contrast agent through the descending aorta. The euthanasia was performed according to the Helmholtz Zentrum Munich Animal Care and Use Committee guidelines. After euthanasia the μAngiofil® was left to polymerize for one hour at room temperature. The sample was then shortly rinsed with dPBS, fixed in 4% paraformaldehyde, and stored at 4°C until ex vivo μ-CT scanning, for which it was inserted in a standard 50 mL Falcon tube. A schematic of a transversal slice of the mouse sample is shown in Figure 3.4.

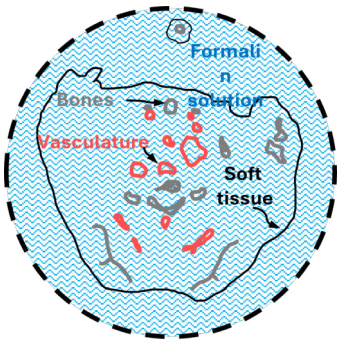

FIGURE 3.4: Schematic of a slice of the murine sample.

The micro-CT was acquired with 720 projections over 360°. The images were acquired in two energy bins, setting the low threshold at 26 keV and the high threshold at 33 keV. The high threshold was set at iodine's K-edge, in order to obtain an energy bin below and the other above this energy. Three shots were acquired for each projection with an exposure time of 3 s. The X-ray tube voltage was set to 50 kVp and the tube current to 2 mA. Given that the detector's active area is

32 mm × 25 mm and that the volume of the whole murine model is 30 mm × 30 mm × 96 mm, 7 acquisitions at different vertical positions of the sample were necessary. The source-to-detector distance was 65 cm and the sample-to-detector distance was 25 cm, making the magnification 1.61 and the voxel size 38 µm.

After acquisitions, the projections were reconstructed using the ASTRA toolbox [Van Aarle et al. 2016] and then the reconstructions from the 7 different acquisitions were stitched together. A two-material decomposition was performed on the stitched volume, using iodine and water as basis materials.

Results and discussion

The results indicate that both the bone structure and the iodinated vasculature were successfully discriminated in the murine body atlas. It is worth mentioning that, although the material decomposition was performed choosing iodine and water as basis material, the entire bone structure falls in the water channel, as its attenuation dependence on energy is more similar to water compared to iodine. This approach thus enabled simultaneous visualization of skeletal tissue and vascular structure at high resolution, providing a comprehensive anatomical reference of the specimen.

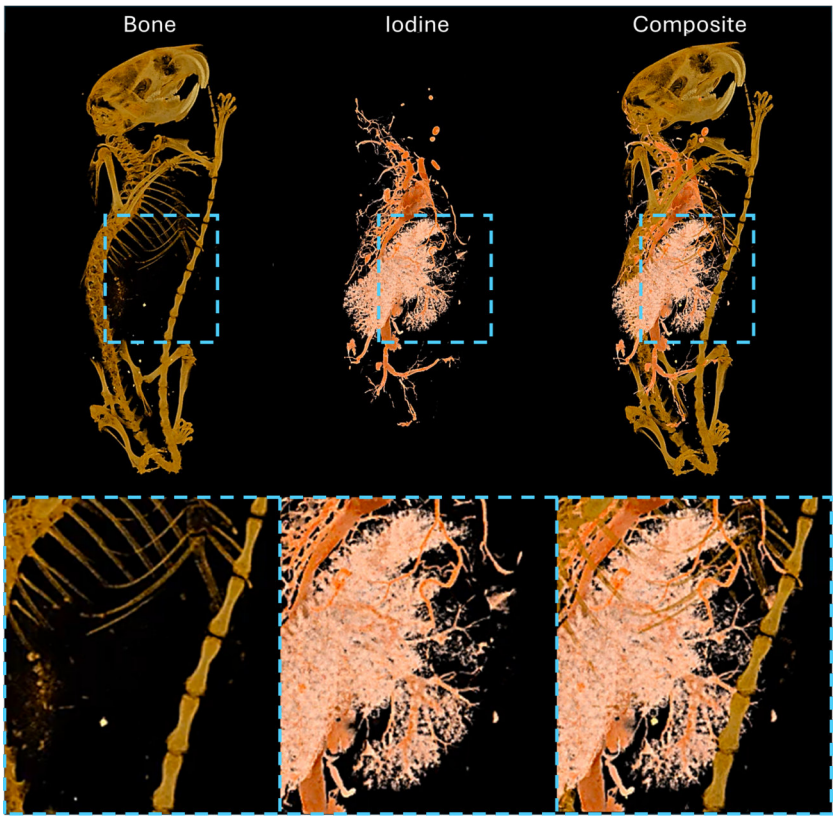

FIGURE 3.5: Bone, iodine, and composite decomposition maps with zoom-ins.

3.2 PHASE-CONTRAST IMAGING WITH LABORATORY SOURCE AND MODULATORS

The work presented in this section is currently submitted for publication in Physical Review A, with the title "*Membrane stepping optimization in Modulation Based Imaging*".

Among the different X-ray phase-contrast imaging techniques mentioned in the previous chapters, tracking-based methods rely on the use of structured illumination to extract information about absorption, refraction and scattering. First, reference images of the known pattern are acquired with no sample. Then, after placing the sample, the altered wavefront is recorded. Phase shifts introduced by the sample distort the modulation pattern, while absorption reduces its overall intensity. By tracking these modifications, it is possible to recover absorption, refraction, and dark-field images.

In general, modulation-based imaging (MoBI) is the term used when referring to X-ray phase-contrast imaging performed using an intensity modulator (or membrane) placed in the beam. Among the existing membranes, sandpaper produces randomly distributed intensity patterns (or speckles if coherent light is employed), which generally have irregular shapes and random distribution of sizes. Small, well-defined speckles that cover a few pixels in the detector plane are usually preferred [Morgan et al. 2012; Zdora 2018]. Recently, alternatives to sandpaper membranes have been explored with the aim of optimizing membrane modulation patterns [Magnin et al. 2025]. These include the use of structured membranes designed to produce specific hole patterns in different geometries.

Although MoBI can, in principle, be performed in a single exposure [Pavlov et al. 2020; Gänz et al. 2022], image quality is typically improved by acquiring several pairs of reference and sample images while moving the membrane between exposures, since repeated measurements reduce noise and provide diverse modulation patterns that strengthen the retrieval. In most implementations of MoBI, this shift is performed in a regular stepping pattern, mainly for practicality reasons. This shift can be performed either one- or two-dimensionally, depending on the experimental setup. Similar strategies are used in related techniques, such as beam tracking using 2D absorption grids, where the regular stepping corresponds to a fraction of the period and the total motion naturally matches the periodic grid structure [Navarrete-León et al. 2023]. Alternative motions schemes have also been investigated: for example, spiral trajectory of sandpaper membranes have been employed to improve sampling across the field of view [Savatović et al. 2025].

While some alternative motion schemes have been explored in the literature, the specific impact of different membrane movement

patterns in MoBI remains unexplored. In this work, we investigate this to determine if, and to what extent, the choice of motion type affects the quality of the final image in MoBI reconstructions, with the aim of optimizing the movement strategy to maximize image quality.

The analysis was conducted experimentally to evaluate the feasibility of optimizing the membrane stepping procedure. The following sections describe the experimental setup, the stepping optimization procedure, and the final data analysis.

3.2.1 *Experimental setup*

The experimental setup is shown in Figure 3.6. Measurements were performed at Xenocs SAS in Grenoble, France, using the Xeuss 3.0 instrument. For this work, its polychromatic cone-beam imaging source, featuring a copper target and operating at 30 kVp with 8.6 keV mean energy, was used. Four different types of membrane were tested in the setup:

1. Sandpaper membrane
2. Archimede: nickel membrane featuring holes arranged in an Archimedean spiral pattern
3. Honeycomb: nickel membrane with holes organized in a hexagonal matrix
4. Vogel: nickel membrane with holes arranged in a spiral pattern that mimics the arrangement of sunflower seeds.

The membrane patterns can be seen in Figure 3.6. The membranes were obtained by laser micro drilling using a fiber laser and was processed by STPgroup (STPgroup, Saint Ismier, France). They were made of Ni foil of 30 µm in thickness, which was then drilled with a circular apertures of 80 µm in diameter.

The scanned sample is a 3D-printed object that follows Julia's fractal geometry, fabricated in resin with dimensions 18 mm × 10 mm and maximum height of 5 mm. The in-plane resolution used was 18 µm, below the spatial resolution of our system. This sample was chosen because it presents features of many different sizes, allowing a better evaluation of the quality of the image.

The detector used was the Eiger2 500k [Donath et al. 2023], which has a 1030 × 514 matrix of 75 µm pixels and a 450 um thick silicon sensor. The membranes, sample, and detector were placed in the primary vacuum. The relevant distances in the setup can be seen in Figure 3.6.

A total of 200 reference images (I_r) and 200 sample images (I_s) were acquired for each membrane while the membrane was stepped in the vertical direction with respect to the X-ray propagation axis.

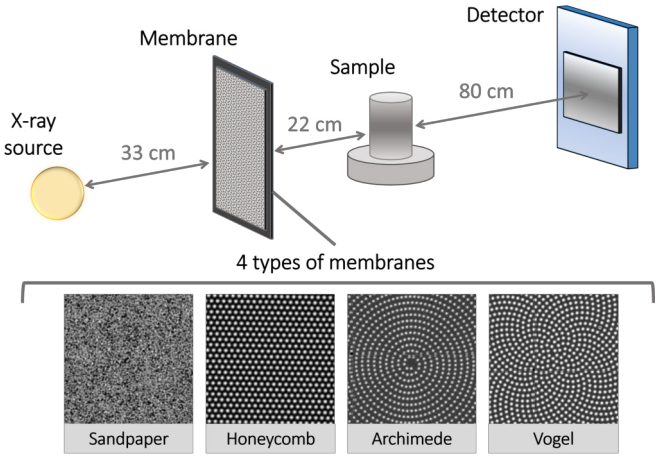

FIGURE 3.6: Experimental setup sketch showing the relevant distances.

Owing to experimental constraints, this motion was restricted to a single direction.

3.2.2 *Stepping optimization procedure*

A dataset of 200 pairs of reference and sample images was acquired for each membrane, covering a wide range of stepping positions with step size of 70 µm. This large dataset allowed for the selection of subsets that simulate different membrane movement patterns, allowing for a comparative analysis of how different stepping procedures affect image quality.

To do this, four distinct stepping strategies were tested (see Figure 3.7). For each of these, subsets of N images were extracted from the full set of 200 reference images:

1. Random stepping: N membrane images were randomly chosen from the large dataset to simulate a random movement of the membrane.

2. Regular stepping: N consecutive membrane positions were selected, mimicking a regular, stepwise membrane motion.

3. Global standard deviation minimization: the subset of N images whose sum had the lowest global standard deviation was selected, with the goal of achieving the lowest global standard deviation across the entire image.

4. Local standard deviation minimization: This method focuses on local uniformity. The sum of N selected membranes was computed, and a local standard deviation map was generated over 7×7 pixel regions. The subset of N membranes that exhibited the smallest standard deviation of this map was chosen. The aim was to avoid localized intensity fluctuations.

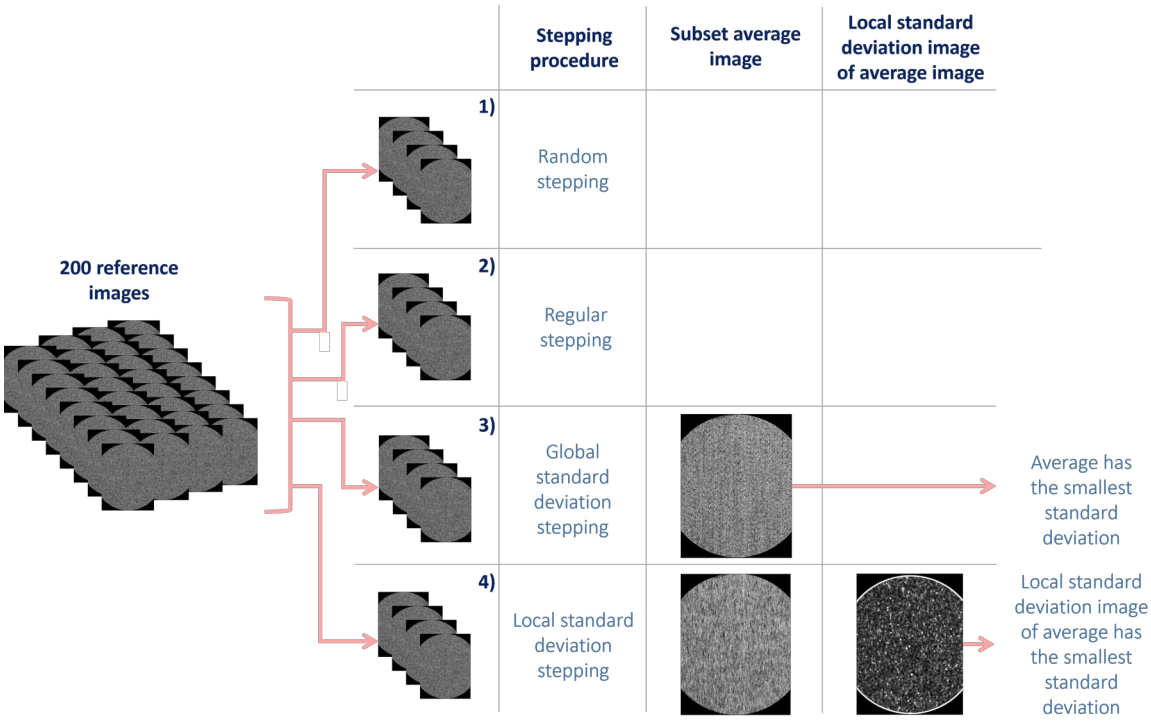

FIGURE 3.7: Stepping optimization procedure. For each membrane type, 200 reference/sample image pairs were acquired. Subsets of size N were extracted using different stepping methods: subsets (1) are extracted randomly, subsets (2) are composed of consecutive images, subsets (3) were chosen by minimizing the standard deviation of their average image, and subsets (4) were selected by averaging the images, thus minimizing the standard deviation of their local standard deviation.

In both optimization-based methods (3 and 4), the objective was to maximize illumination uniformity on the sample, both globally and locally, using standard deviation as an optimization metric to quantify intensity variation. A lower standard deviation in the sum image indicates an overall more homogeneous illumination. The local standard deviation stepping method was thought to prevent small pixel regions with high intensity variation.

3.2.3 *Data analysis*

The stepping optimization procedure described in the previous section was applied for each of the four membrane types shown in Figure 3.6. For every combination of membrane type and stepping strategy, seven subsets were extracted from the full set of 200 reference/sample pairs of images. Each subset contained a number N of pairs of reference/sample images, with N=4, 5, 7, 10, 15, 20 and 30. This range was chosen to evaluate how the number of stepping positions affects image quality across different membrane types and stepping methods. This data handling is summarized in Table 3.3.

For each subset, absorption, refraction, and dark field images were recovered from reference and sample images using the implicit Low Coherence System (LCS) algorithm [Quénot et al. 2021; Morgan

TABLE 3.3: Overview of the data handling. For each of the four membrane types, a dataset of 200 reference/sample image pairs was acquired. From each dataset, subsets of size $N = 4, 5, 7, 10, 15, 20, 30$ were extracted using four different stepping strategies.

Membrane Type	**Total Images**	**Stepping Strategies**	**Subset Sizes (N)**
Archimede	200 pairs	Random, Regular, Global Std, Local Std	4, 5, 7, 10, 15, 20, 30
Honeycomb	200 pairs	Random, Regular, Global Std, Local Std	4, 5, 7, 10, 15, 20, 30
Sandpaper	200 pairs	Random, Regular, Global Std, Local Std	4, 5, 7, 10, 15, 20, 30
Vogel	200 pairs	Random, Regular, Global Std, Local Std	4, 5, 7, 10, 15, 20, 30

and Paganin 2019; Paganin and Morgan 2019].

In general, modulation-based imaging algorithms compare reference and sample images by analyzing how the reference pattern is distorted when the sample is inserted. LCS is based on flux conservation: the model relates the reference and sample images to the absorption, the displacement fields (representing refraction), and a diffusion term (corresponding to the dark field signal). The algorithm is formulated as a system of equations presenting 4 unknowns, indicating that a minimum of 4 membrane positions is required in order to solve it.

Once absorption, refraction, and dark field images are retrieved, image quality is evaluated using the contrast-to-noise ratio (CNR) for absorption and dark field images and angular sensitivity for refraction images. The total CNR is calculated as the average CNR measured across six different 30 pixel × 30 pixel regions inside the sample and six 30 pixel × 30 pixel regions in the background:

$$CNR = \frac{\bar{\mu}_s - \bar{\mu}_{bg}}{\bar{\sigma}_{bg}} \tag{3.1}$$

where $\bar{\mu}_s$ and $\bar{\mu}_{bg}$ are the means of the individual mean intensity values of the regions respectively inside the sample and in the background, and $\bar{\sigma}_{bg}$ is the mean standard deviation of the regions of pixels in the background. The associated error is evaluated through

propagation of the error. Multiple regions were chosen to give a more global estimate of image quality.

The angular sensitivity σ_θ is assessed in a region of the image without the sample by calculating the mean and standard error of the standard deviation of the refraction angles in twelve 45 pixel×45 pixel regions (σ_{θ_i}):

$$\sigma_\theta = \frac{1}{12}\sum_{i=1}^{12}\sigma_{\theta_i} \tag{3.2}$$

Quantifying the dispersion of noise, the angular sensitivity determines the minimum detectable refraction angle of the system.

Finally, spatial resolution was calculated with an approach similar to that described in [Modregger et al. 2007]. The method determines spatial resolution by identifying the point in the frequency domain at which the signal becomes indistinguishable from noise. The noise power spectrum is calculated from the 2D image as a function of spatial frequency, the noise baseline is then identified from high-frequency components where only noise exists, and the resolution is calculated from the maximum spatial frequency where the total spectral power equals twice the noise baseline.

These quality metrics were evaluated for each membrane type, stepping method, and subset with a number of N reference/sample pairs.

3.2.4 *Results and discussion*

The experiment involved four different membranes types [Magnin et al. 2025], aiming not only to validate the proposed optimization approach but also to assess its consistency across various membrane types. Subsets containing 4, 5, 7, 10, 15, 20 and 30 membrane positions each were extracted from each dataset of 200 reference/sample pairs, using each of the four stepping procedures (regular, random, global standard deviation and local standard deviation). This allowed for an evaluation of how the number of stepping positions affects image quality.

Figure 3.8 shows the results obtained using the honeycomb membrane and a subset size of five positions. The graphs display the quality metrics measured from the images as a function of the membrane stepping method. A cropped region of the image for each stepping method is displayed for visual comparison.

The results indicate that the global standard deviation and the local standard deviation stepping procedures generally produced the highest image quality whatever the modulation topology. Specifically, these methods achieved the highest CNR values both in absorption and dark field images, as well as the lowest angular sensitivity values

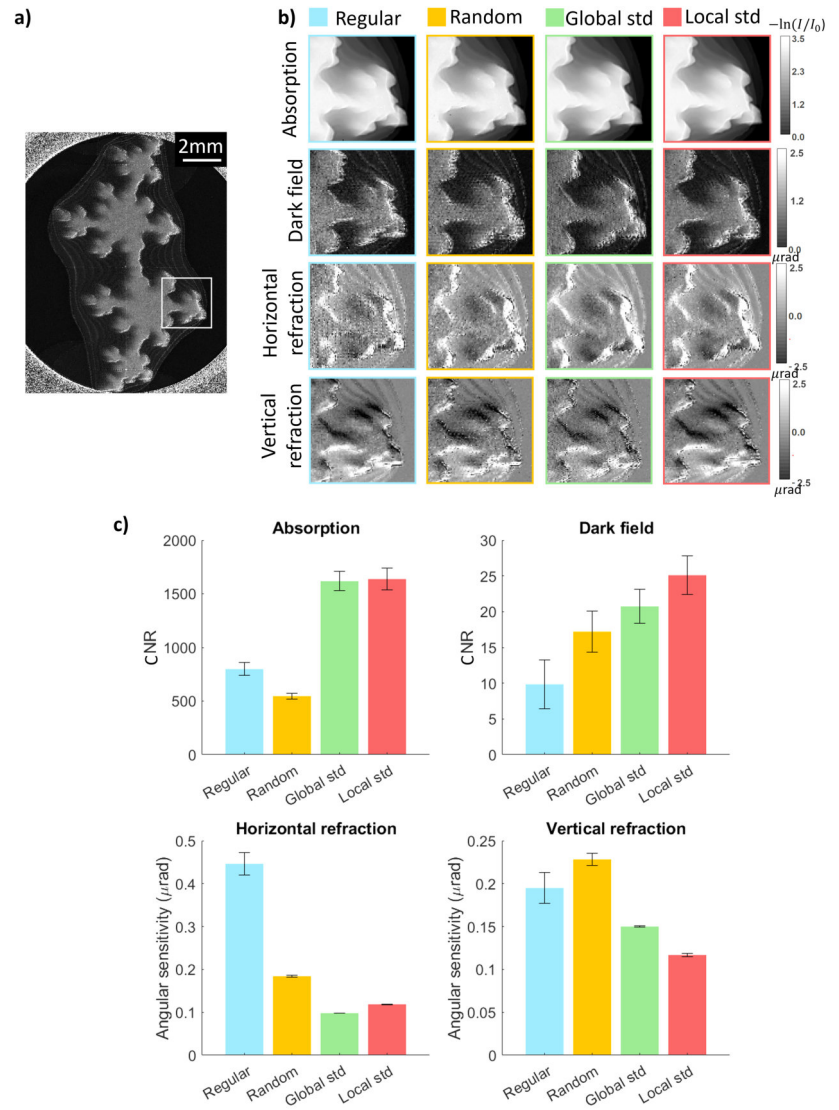

FIGURE 3.8: a) Dark field image of the full sample obtained with a subset size of 5 and the honeycomb membrane. b) Absorption, dark field, horizontal refraction, and vertical refraction images retrieved using each optimization procedure: regular, random, global standard deviation, and local standard deviation. Only a cropped region of the image is shown for clarity. c) Quantitative evaluation: graphs displaying the quality metrics measured from the images as a function of the membrane stepping method.

in refraction. For both vertical and horizontal refraction, angular sensitivity values around 0.1 μrad were achieved with the optimized stepping methods, approximately twice as low as those obtained with regular and random stepping.

Given its overall better performance, the local standard deviation method was selected to evaluate the performance of the different membrane types. The results obtained using this method for each membrane, with a subset size of 5, are presented in Figure 3.9. The same quality metrics were computed and plotted as a function of the membrane type. Again, only a cropped region of the image is displayed for visual comparison.

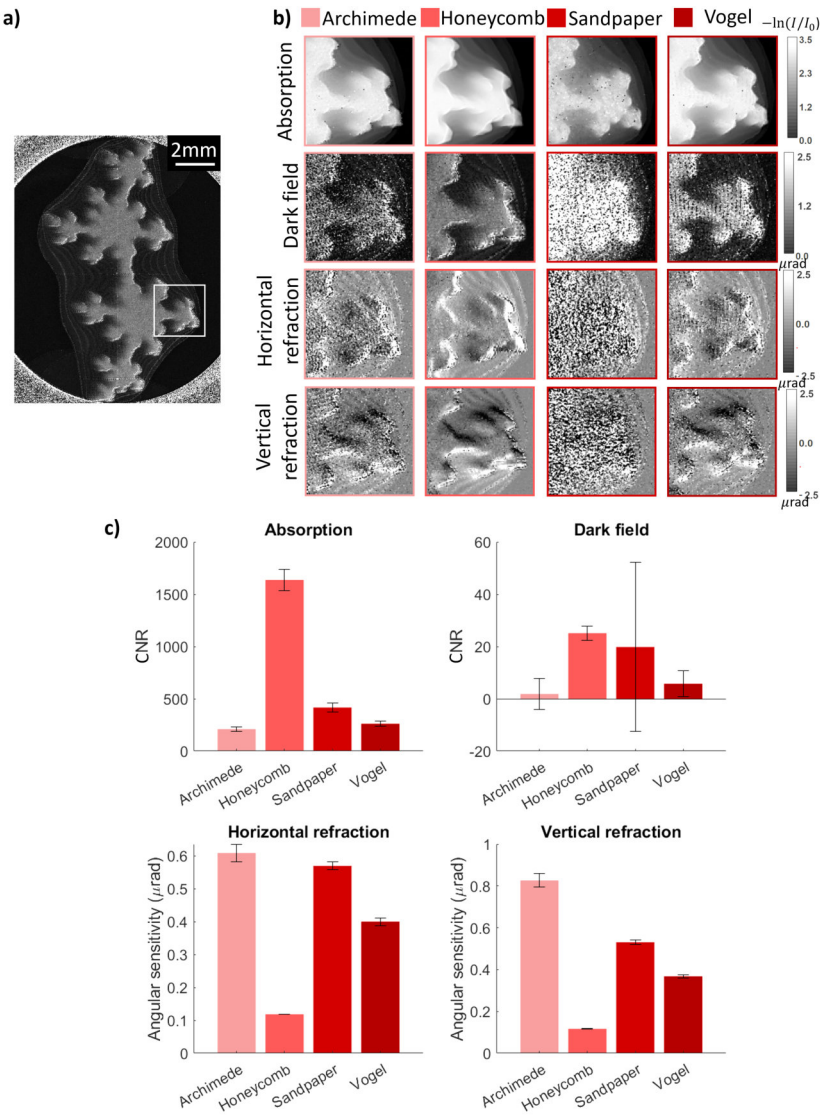

FIGURE 3.9: a) Dark field image of the full sample obtained with a subset size of 5 and the local standard deviation method. b) Absorption, dark field, horizontal refraction, and vertical refraction images retrieved using each membrane: archimede, honeycomb, sandpaper, and Vogel. Only a cropped region of the image is shown for clarity. c) Quantitative evaluation: graphs displaying the quality metrics measured from the images.

The results indicate that the honeycomb membrane consistently yields the best results, with the highest CNR values in both absorption and dark field images, as well as the lowest angular sensitivity in refraction images. Specifically, the honeycomb membrane achieves angular sensitivity values around 0.1 μrad, whereas the other membranes range between 0.3 and 0.8 μrad. This suggests stronger compatibility between the honeycomb membrane and the optimization procedure. It is also worth noting that the sandpaper membrane did not produce usable images. The retrieved images in this case are dominated by noise and do not contain any meaningful information. While the noise estimation in the background was reliable for all other membranes, the sandpaper membrane exhibits significantly higher

noise within the sample.

The results presented above are all obtained from a fixed subset size of five pairs of sample/membrane images. However, as mentioned earlier, the study was conducted across multiple subsets sizes. Figure 3.10 presents the results obtained for each membrane using the local standard deviation procedure, showing how the quality metrics vary with the number of membrane positions included in each subset.

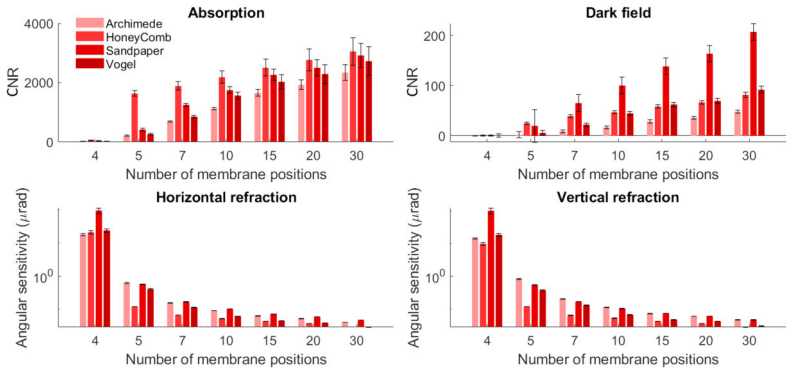

FIGURE 3.10: Quality metrics measured from the absorption, refraction and dark-field images for each membrane type, plotted as a function of the number of membrane positions included in the subset.

Again, the honeycomb membrane delivers the best overall performance, showing a rapid increase in CNR when the number of membrane positions increases from 4 to 5 in the absorption images. The same trend is seen in angular sensitivity as the number of positions increases. These trends are observed across all membranes types, although with a more gradual improvement in quality metrics. Notably, for the dark field CNR, the honeycomb membrane exhibits a rapid initial increase, but the Vogel membrane outperforms it when more than 10 membrane positions are used.

Finally, spatial resolution was evaluated through the noise power spectrum method. Figure 3.11 shows the noise power spectra derived from the vertical refraction images, using a subset of five honeycomb membrane positions. In the plot, the noise power spectrum obtained for the random stepping is not showed as it did not converge. The corresponding resolution values, reported in Table 3.4, are reported for horizontal and vertical refraction, and dark-field, allowing a comparison of the performance across different membrane stepping methods.

The noise power spectra clearly show the superiority of the global and local standard deviation stepping methods compared to the random and regular approaches. Both the local and global methods achieve consistent spatial resolution values across all modalities, supporting the effectiveness of the proposed stepping optimization strategy. The global standard deviation method exhibits greater variability,

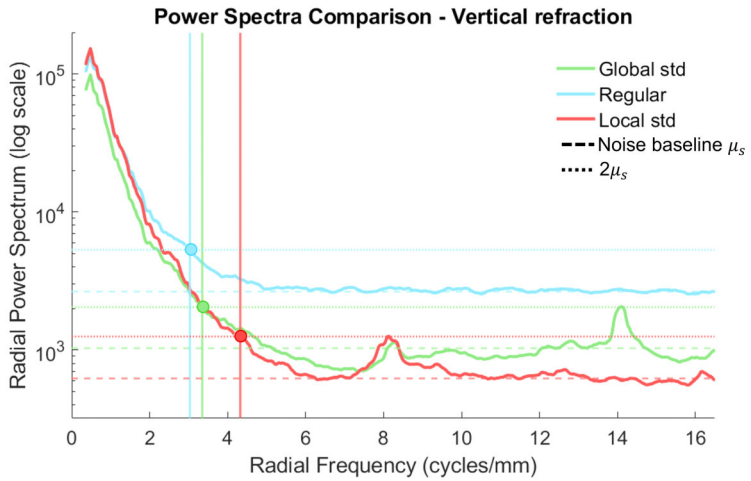

FIGURE 3.11: Radial noise power spectrum calculated from vertical refraction images for each membrane stepping method. The noise baseline is identified from high-frequency components where only noise exists, and the resolution is calculated from the maximum spatial frequency where the total spectral power equals twice the noise baseline (dots on spectrum).

TABLE 3.4: Spatial resolution values for each membrane stepping method across refraction and dark-field images. The value for the random stepping method in the case of vertical refraction is not displayed as it did not converge. HR: Horizontal Refraction; VR: Vertical Refraction; DF: Dark Field

Method	**HR (mm)**	**VR (mm)**	**DF (mm)**
Random	1.67 ± 0.22	-	1.47 ± 0.17
Regular	1.32 ± 0.14	0.329 ± 0.013	0.463 ± 0.036
Global std	0.202 ± 0.028	0.298 ± 0.079	0.218 ± 0.106
Local std	0.266 ± 0.022	0.232 ± 0.020	0.221 ± 0.008

indicating a higher sensitivity to local fluctuations. In contrast, the regular and random methods yield poorer resolutions, ranging between 0.3 mm and 2 mm. Notably, the random method fails to converge for vertical refraction. One important thing to note is that the reported spatial resolution values are derived from an "arbitrary" method and should not be interpreted as an absolute measure of spatial resolution. Rather, they should be regarded as a qualitative indicator for comparing different images (for example, to assess which image performs better or worse). In this context, a more meaningful approach is to compare the overall behavior of the noise power spectrum, considering it as a whole function rather than extracting a resolution value from a single, arbitrarily chosen point on the curve. The selection of a single point is adopted solely for clarity and conciseness, in order to summarize the results without the need to display a large number of noise power spectra.

The findings of this work suggest the advantage of optimizing the membrane stepping strategy at the beginning of an experiment. By initially sampling a large number of different membrane positions, the local or global standard deviation methods can be applied to

identify the optimal stepping pattern. Once this is determined, the corresponding motor positions can be recorded and used consistently throughout the experiment. This procedure ensures that data acquisition is performed under optimized and reproducible conditions, ensuring an optimized and stable image quality.

This work demonstrated the effectiveness of optimized movement strategies in MoBI through an experimental study. The results show that the two optimized stepping procedures consistently produced the highest image quality, achieving the highest CNR in the absorption and dark field images, the best angular sensitivity in refraction images, and superior spatial resolution overall.

The study was performed using four different types of membranes: the honeycomb membrane yielded the best results overall, suggesting a stronger compatibility with the optimization procedure compared to the other membranes. In addition, the quality analysis conducted using the noise power spectrum method confirmed the superiority of both the global and local standard deviation stepping methods.

Future work may extend this study exploring alternative optimization procedures, also including a broader range of membrane types or different experimental conditions including directional dark-field sensitivity. Ultimately, the optimization of membrane movement in MoBI has the potential of enhancing image quality without increasing experimental complexity, thereby strengthening the technique's overall performance and potentially reducing the number of exposures required to achieve the same image quality.

4

Synchrotron-Based Imaging

Synchrotron X-ray imaging exploits the unique properties of synchrotron radiation to achieve high-quality imaging of biological samples and materials. The main advantages of synchrotron-based imaging are the enhanced spatial resolution and contrast, due to the high brilliance, small effective source size, and high coherence of the beam.

This chapter presents the research conducted during my PhD in synchrotron-based imaging.

The first section describes a source-based spectral phase-contrast experiment performed at the European Synchrotron Radiation Facility (ESRF) in Grenoble. Human thyroid specimens were scanned using the beam tracking phase-contrast technique at two monochromatic energies, with the goal of performing spectral decomposition to assess the distribution of iodine within the samples.

The second, more extensive section focuses on my primary PhD research project *Spectral PHasE REtrieval X-ray imaging (SPHERE-X)*. The aim of the project was to develop and implement a combined spectral and phase-contrast imaging setup at the SYRMEP beamline of the Elettra synchrotron in Trieste. Phase-contrast was achieved using the beam tracking technique, while spectral imaging was performed using an energy-dispersive Laue crystal. This section presents simulation development, crystal characterization (energy resolution and focus dimension), as well as studies on the beam tracking absorbing mask. The chapter concludes with the imaging results obtained from the main experimental setup, along with additional results obtained from an alternative configuration.

4.1 SOURCE-BASED SPECTRAL PHASE-CONTRAST IMAGING WITH BEAM TRACKING

Virtual histology is an emerging imaging tool used in medical imaging that uses X-rays to provide three-dimensional, high-resolution images of soft-tissue specimens. Conventional histology is used to study

the detailed structure of tissues and cells using optical microscopy and is the standard diagnostic procedure in pathology [D'Avanzo et al. 2004]. While this method is still the gold standard for tissue pathology as it is widely accessible and highly specific for particular tissue regions or cells [Alturkistani et al. 2015], it is time-intensive, and requires mechanical sectioning of the specimens. In addition, regions of interest cannot be located beforehand and the analysis is intrinsically two-dimensional [Albers et al. 2018]. These problems are potentially overcome by virtual histology. Virtual histology uses X-ray micro-tomography to provide three-dimensional images at high resolution and allows for quantification of tissue structures, as well as the localization of small regions of interest, while being non-destructive [Frohn et al. 2020]. Moreover, this technique enables virtual slicing, allowing for the localization and analysis of regions of interest without prior physical intervention. However, the limited accessibility of synchrotron facilities restricts the routine medical use of these methods, though laboratory-based implementations are also being investigated [Töpperwien et al. 2017; Scott et al. 2015].

The X-ray modality which allows for effective virtual histology is phase-contrast imaging, which measures the phase shifts of X-rays which are generally 2 or 3 orders of magnitude larger than X-ray attenuation. This enhances the visibility of soft tissues, which normally exhibit low absorption contrast in conventional absorption-based X-ray imaging. When phase-contrast imaging is combined with spectral imaging, they allow not only for structural visualization but also for material differentiation, providing compositional information about the sample [Lee et al. 2019].

In this section, source-based spectral phase-contrast imaging was applied to human thyroid tissue samples to investigate its potential for the characterization of thyroid microstructure. The thyroid is an organ of particular interest due to its complex architecture, as well as its critical physiological role in endocrine regulation. The thyroid synthesizes two iodine-containing hormones, triiodothyronine (T3) and thyroxine (T4), which regulate metabolism, growth, and development. Iodine is an essential, rate-limiting element in this process: it is actively accumulated by the thyroid gland and incorporated into the precursors of T3 and T4 [Chung 2014; Sorrenti et al. 2021]. The local distribution and concentration of iodine within thyroid tissue can therefore serve as an important marker of both normal and pathological states.

The following sections describe in detail the experimental setup, data acquisition, and image processing, followed by the presentation and discussion of some of the results obtained from the spectral phase-contrast imaging of thyroid samples.

4.1.1 *Experimental setup, acquisition, and image processing*

The experiment was carried out at the BM05 beamline of the European Synchrotron Radiation Facility (ESRF, Grenoble, France) [Ziegler et al. 2004].

X-rays were produced by a 2-pole wiggler and monochromatized at the desired energy using a double-crystal monochromator. The acquisition was performed at two monochromatic energies bracketing the K-edge of iodine (33.2 keV), specifically at 33.05 keV and 33.29 keV. For each energy, 2000 projections were acquired over 360° in extended field-of-view modality and continuous rotation mode, with an exposure time of 0.5 s per projection.

The acquisition was performed using the beam tracking technique by inserting an absorbing mask made of a 350 µm thick gold substrate about 20 cm before the sample. The mask featured 10 µm apertures with a 61 µm pitch, thus six dithering steps of the absorbing mask were necessary to cover the whole sample.

The detector consisted of a PCO.edge 5.5 sCMOS camera [Excelitas Technologies Corp. 2019] with a pixel size of 6.5 µm, coupled to an optical system. The sample-to-detector distance was 1.4 m, resulting in an effective pixel size of 6.34 µm after accounting for magnification.

The samples consisted of multiple formalin-fixed and paraffin-embedded human thyroid tissue blocks. In total, five thyroid tissue blocks were scanned during the experiment; however, only two representative samples are presented in this thesis. The first (Thyroid 1), contained an invasive follicular carcinoma with multiple foci of capsular infiltration, while the second (Thyroid 2) presented a minimally invasive follicular carcinoma.

Photographs of both the two samples and the sample stage with the absorbing mask in the beamline are shown in Figure 4.1.

The acquired images were first preprocessed through dark subtraction and flat-field correction. Each beam tracking projection was then analyzed in MATLAB [Inc. 2022] to extract the absorption, refraction, and dark-field signals. The refraction projections were subsequently integrated using a Wiener-filter regularized phase retrieval algorithm to generate the corresponding phase projections. All projection sets were reconstructed via filtered back projection, yielding three tomographic volumes (absorption, phase, and dark-field) for each of the two acquisition energies. Finally, the absorption images at both energies, together with the phase images, were used as inputs for the spectral phase-contrast decomposition algorithm, employing water, calcium, and iodine as basis materials.

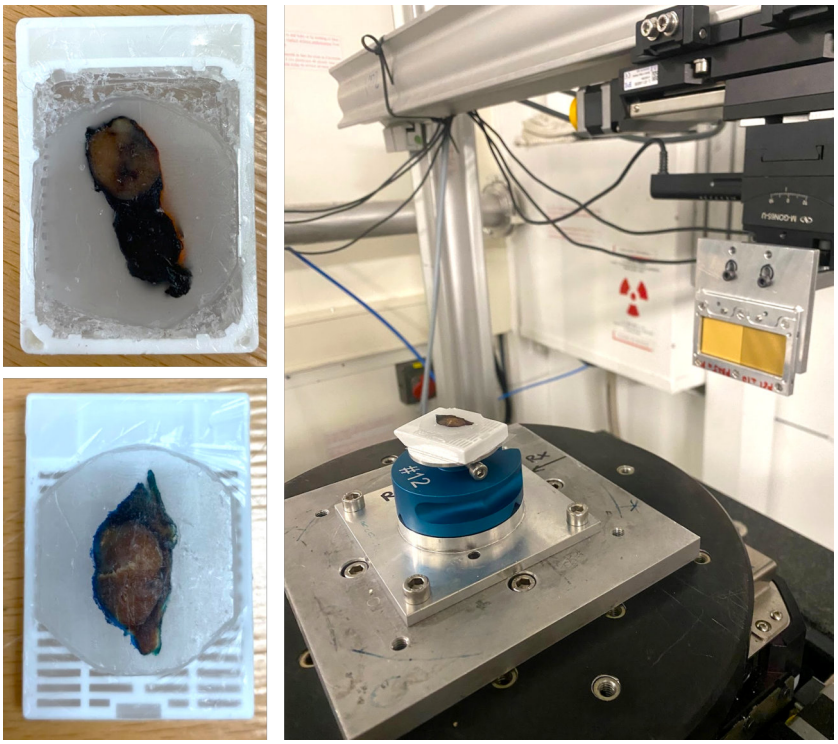

FIGURE 4.1: Left: photographs of the two histological cassettes containing the specimens. Right: photograph of the sample stage of the beamline, where the absorbing mask can be seen too.

4.1.2 *Results and discussion*

The imaging results obtained for Thyroid 1 are presented in Figure 4.2.

The figure shows the total phase image, obtained by summing the phase images acquired below and above the K-edge, along with the decomposition maps of calcium and iodine, as well as an overlay of these maps on the phase image. Panels (a) and (b) display a zoom in of the phase image and the overlay, respectively.

The results demonstrate high-fidelity visualization of tissue structures in the phase map and effective separation of elemental components in the iodine and calcium maps. Notably, both small follicles and macro-follicles containing iodine are clearly visible, while a large high-contrast feature within the thick capsule is observed in the calcium map. Histological analysis independently confirmed the presence of a macro-calcification in this region, and consistently, the corresponding signal in the material decomposition is assigned to calcium. In the zoom in, the high-intensity features in the phase map are confirmed to correspond to calcium. The mean iodine concentration and total iodine content of the thyroid were determined over a volume of 30 slices (corresponding to 0.023 cm^3), yielding values of 0.83 $mg\,mL^{-1}$ and 19.5 µg, respectively. A threshold-based mask was applied to segment the thyroid volume from the background.

The results for Thyroid 2 are shown in Figure 4.3.

Similar to Thyroid 1, the figure shows the total phase image, the

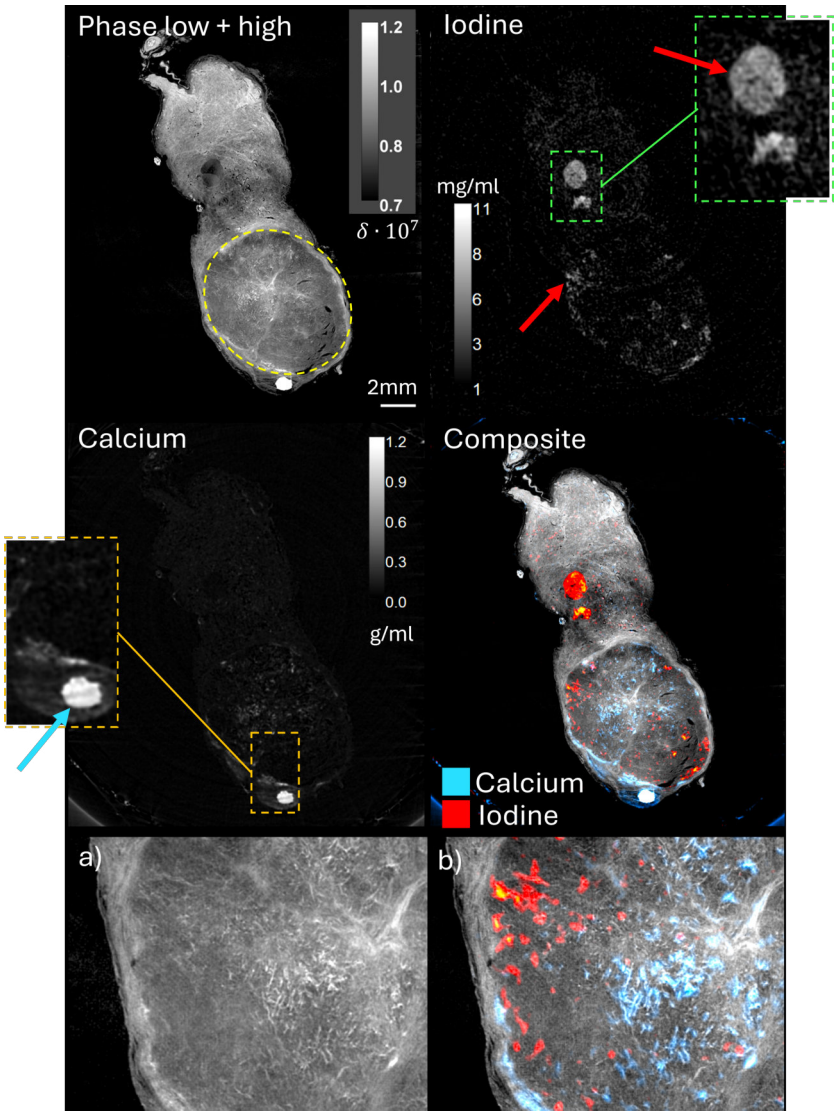

FIGURE 4.2: Imaging results for Thyroid 1. Top left: total phase image, with the tumor capsule indicated by a yellow dashed line. Top right: elemental decomposition map for iodine, with micro- and macro-follicules highlighted by red arrows; the zoom in shows a macro-follicle. Center left: elemental decomposition map for calcium, with a macro-calcification indicated by a blue arrow; the zoom in shows the macro-calcification. Center right: overlay of the elemental maps on the phase image. (a) Shows a zoom in of the phase image, and (b) shows a zoom in of the overlay.

decomposition maps of calcium and iodine, and an overlay of the elemental maps on the phase image. Panels (a), (b), and (c) display a zoom in of the phase image, the calcium overlay, and the total overlay, respectively.

In Thyroid 2, the healthy tissue maintains the ability to accumulate iodine, whereas the lesion shows a loss of iodine uptake, highlighting the altered functionality of the affected region. Multiple small calcifications are also evident in the healthy tissue from the calcium map. Compared to Thyroid 1, which also contained a follicular carcinoma, only the healthy regions in Thyroid 2 exhibit iodine accumulation, while the lesion does not. Again, the mean

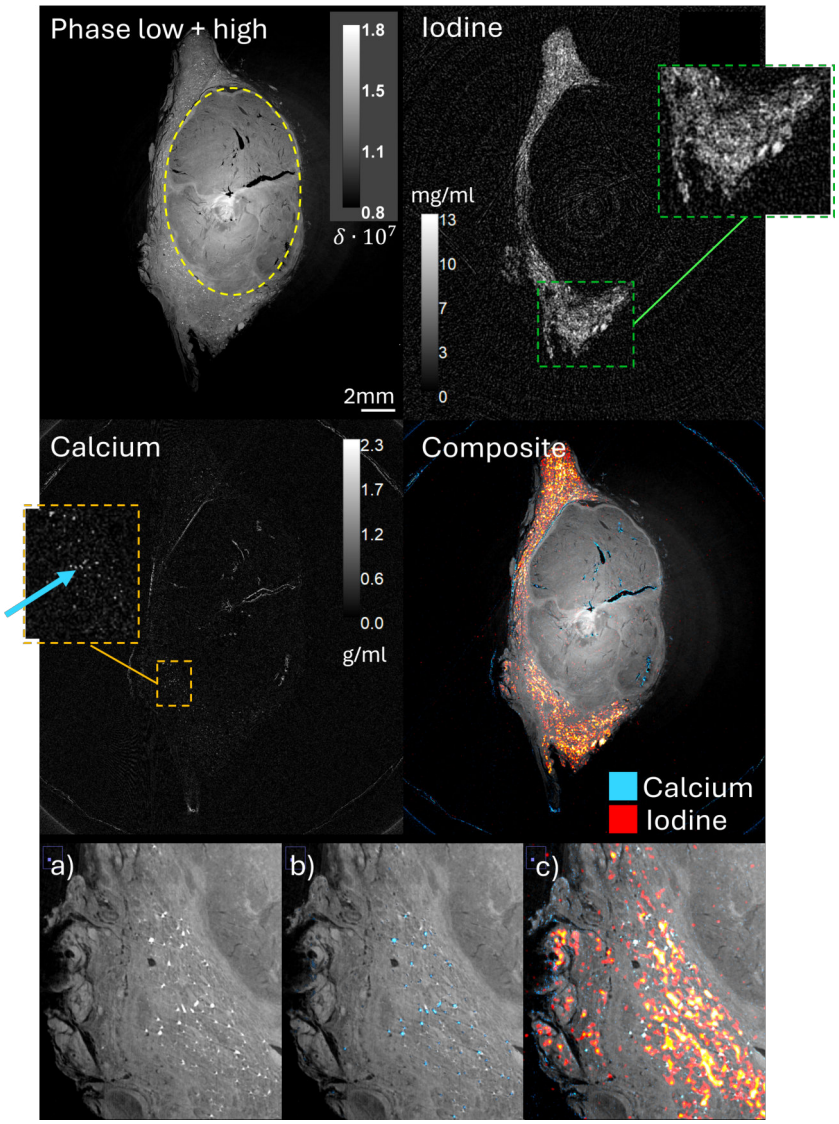

FIGURE 4.3: Imaging results for Thyroid 2. Top left: total phase image, with the lesion capsule indicated by a yellow dashed line. Top right: elemental decomposition map for iodine; the zoom in follicles filled with iodine. Center left: elemental decomposition map for calcium; the zoom in shows multiple micro-calcifications indicated by a blue arrow. Center right: overlay of the elemental maps on the phase image. (a) Shows a zoom in of the phase image, (b) shows a zoom in of the phase image with calcium overlaid, and (c) shows a zoom in of the phase image with calcium and iodine overlaid.

iodine concentration and total iodine content of the thyroid were determined over a volume of 30 slices (corresponding to 0.021 cm^3), yielding values of 1.10 $mg\,mL^{-1}$ and 23.05 µg, respectively.

It is important to note that the inclusion of the phase map in the decomposition process allows for the generation of three quantitative maps rather than only two. This is particularly significant for thyroid tissue, where conventional absorption-based imaging may not distinguish iodine-filled follicules from calcifications, as both can exhibit similar absorption. By combining spectral and phase-contrast information, iodine and calcium can be accurately separated, provid-

ing a more comprehensive and quantitative characterization of the sample's composition.

While conventional histology remains the gold standard for tissue pathology, these results demonstrate the potential of spectral virtual histology, which is capable of providing 3D volumes at a micrometer-scale resolution. The volumetric data allows lesions and microstructures to be examined in their full spatial extension, while the spectral information provides quantitative insight into the sample's composition. Together, both offer a more comprehensive characterization of tissue morphology and material distribution.

4.2 CRYSTAL-BASED SPECTRAL PHASE-CONTRAST IMAGING WITH BEAM TRACKING

Crystal-based spectral imaging, or SKES, is a spectrum-based imaging method conceived to acquire images of an object across typically hundreds of energies [Zhu et al. 2014]. The acquisition of a portion of a sample at hundreds of different energies with a high energy resolution can bring several advantages for chemical imaging by enabling spatial discrimination of different contrast elements.

The beam tracking phase-contrast technique has been introduced in Chapter 2, and will be thoroughly discussed in this section. This method employs a structured absorbing mask positioned in the X-ray beam to shape it into an array of narrow beamlets, whose intensity distribution is mapped on the detector. When a sample is introduced into the beam, it alters the beamlet profiles by changing their intensity, spatial position, and width. These variations correspond respectively to absorption, refraction, and ultra-small-angle scattering.

The goal of the SPHERE-X project, carried out during my PhD, was to develop a novel experimental setup that combined crystal-based spectral imaging with beam tracking phase-contrast imaging at the SYRMEP beamline of the Elettra synchrotron in Trieste. My contribution included simulation development, crystal characterization, mask and image retrieval algorithm optimization, the execution of multiple imaging experiments at Elettra, and data analysis. In this framework, the first ever images combining beam tracking phase-contrast with energy-dispersive Laue crystal imaging were performed. In addition, alternative imaging setups with multiple detectors were also designed and implemented for multi-modal imaging.

The following sections present this work in detail. They begin with crystal characterization (energy resolution and focus dimension), the development of a simulation for SKES, mask optimization through a visibility study, and beam tracking algorithm refinement, before

concluding with the description of the setup design and results.

4.2.1 *A crystal study*

The benders

The bending of the crystals is achieved using a custom-designed two-bar bender, shown in Figure 4.4. The bender consists of two main frames: the first one is an aluminum block with a slotted aperture (8 mm × 80 mm), machined along the bending direction to the desired radius. To ensure a more homogeneous stress distribution on the crystal, a 1 mm thick politetrafluoroetilene (teflon) layer is attached to the curved surface of the bender.

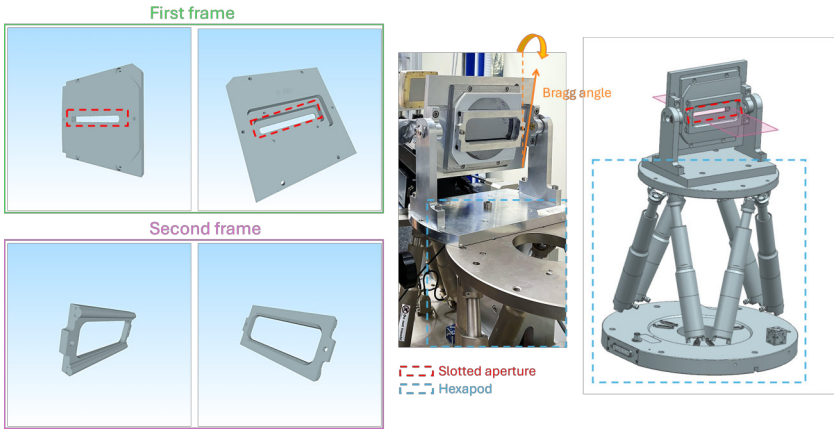

FIGURE 4.4: From left to right: CAD figures of the bending frames, picture of the whole frame mounted in the experimental setup, and CAD sketch of the whole frame mounted on the hexapod.

The second frame consists of an aluminum block featuring a wide aperture and two Teflon rods. The crystal is positioned on the curved frame while the second frame is placed on top and coupled to the first by using two screws. When pressure is applied by the rods, the crystal bends and adapts to the curvature of the underlying surface. Once the crystal is bent and the two frames are screwed together, the first frame is screwed onto a larger support that enables mounting on a positioning stage and tilting to the desired Bragg angle. The inclination of the frame system is fixed according to the desired diffracted energy spectrum.

The entire bending frame is positioned onto a six-degrees-of-freedom hexapod positioning stage, located at approximately 23 m downstream from the bending magnet source.

Benders with radii of 0.3 m, 0.5 m, 1.0 m, and 1.5 m are available for use in the experiments.

Energy resolution

An energy resolution study was carried out at different energies to evaluate the performance of the system. In theory, the intensity transition at the K-edge energy is sharp and has a width of a few electronvolts due to intrinsic lifetime broadening effects [Nicolas and Miron 2012]. In spectral systems making use of bent crystals, the energy resolution is typically broader. As a result, the K-edge transition is spread over a wider energy range. Several factors contribute to this broadening [Qi et al. 2021]:

1. Crystal properties: non-uniformity of the d-spacing due to the crystal's curvature
2. Source characteristics: finite source size and distance from the crystal
3. Detector: pixel size and spatial resolution

These factors are thoroughly described in Appendix B.1.

Both the crystal bending radius and the Bragg angle are fundamental crystal properties that affect energy resolution. The energy resolution of the system was measured by retrieving the intensity profile plot along the energy (i.e. vertical) axis at a position corresponding to the absorption edges. Four elements relevant to biomedical imaging, namely molybdenum, silver, iodine and barium, were investigated, covering a representative range of K-edge energies. Each profile was fitted with the following *Erf* function:

$$f(x) = a + b\ Erf\left(\frac{x-c}{d}\right) \tag{4.1}$$

where a, b, c, and d are the fit parameters, and the variable x corresponds to energy. The *Erf* function describes a smooth, symmetric transition centered in c, representing the cumulative form of a Gaussian distribution. By assuming a Gaussian energy blurring, the full width at half maximum (FWHM) in pixel units is computed as:

$$FWHM = 2\sqrt{2\ ln2}\ \frac{d}{\sqrt{2}} \tag{4.2}$$

The used crystal is a 300 µm thick silicon wafer. The surface pole was oriented along ⟨110⟩ and cut at a 2.5 deg angle relative to the utilized $(\bar{2}20)$ reflection. The crystal bending radius was varied using different benders, reaching the radii of 0.5 m, 1.0 m, and 1.5 m. The Bragg angle was adjusted depending on the contrast element used, in order for the energy spectrum to encompass its K-edge energy.

The pixel to energy conversion was obtained from the energy calibration. By multiplying the energy pixel equivalent by the FWHM

estimated as in Equation 4.2, the system's absolute (dE) and relative (dE/E) energy resolutions were evaluated.

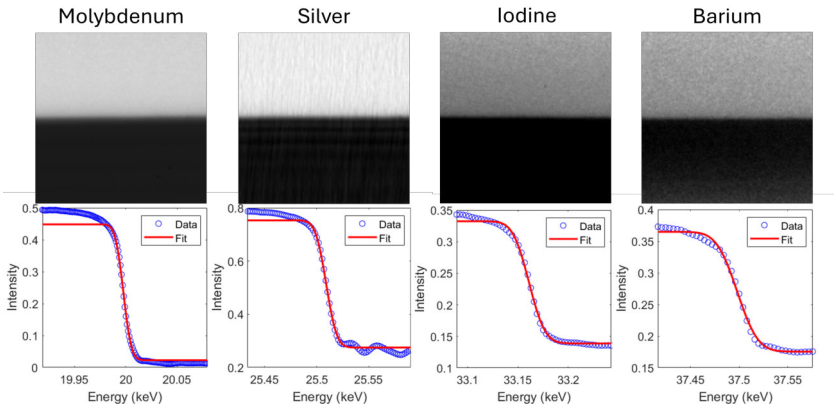

FIGURE 4.5: Top: K-edge images of molybdenum, silver, iodine, and barium obtained with a crystal bending radius of 1.0 m. Bottom: corresponding vertical profile plots fitted with an Erf function.

In Figure 4.5, the K-edge images of molybdenum, silver, iodine, and barium, along with their *Erf* function fits, are shown. These images were obtained with a crystal bending radius of 1.0 m.

Table 4.1 reports the absolute and relative energy resolutions obtained for molybdenum, silver, iodine, and barium at three crystal bending radii.

TABLE 4.1: Energy resolution values for each contrast element used, with their K-edge energy. The relative resolution is indicated as well.

Crystal bending radius (m)	**Contrast material**	**K-edge energy (keV)**	ΔE **(eV)**	$\Delta E/E \cdot 10^{-3}$
0.5	Mo	20.0	16.85 ± 0.45	0.84 ± 0.02
	Ag	25.5	22.58 ± 1.00	0.89 ± 0.04
	I	33.2	36.61 ± 1.36	1.10 ± 0.04
	Ba	37.5	44.58 ± 4.11	1.19 ± 0.11
1.0	Mo	20.0	10.86 ± 0.36	0.54 ± 0.02
	Ag	25.5	16.25 ± 0.98	0.64 ± 0.04
	I	33.2	20.07 ± 1.57	0.61 ± 0.05
	Ba	37.5	26.75 ± 3.53	0.71 ± 0.09
1.5	Mo	20.0	8.45 ± 0.42	0.42 ± 0.02
	Ag	25.5	14.99 ± 1.16	0.59 ± 0.05
	I	33.2	16.50 ± 1.40	0.50 ± 0.04
	Ba	37.5	19.94 ± 2.89	0.53 ± 0.08

From the results, it is clear how the energy resolution worsens progressively as the bending radius decreases. This is expected, since the more the crystal is bent, the larger the non-uniformities in the

crystal d-spacing are, which constitute a fundamental contribution to the broadening of the energy response.

The relative energy resolution values remain within the order of 10^{-3}, demonstrating the system's high spectral resolution within the investigated energy range.

However, another fundamental quantity in crystal-based spectral imaging is the transmitted energy bandwidth (see Section 2.1.6). A larger bending radius produces a narrower energy bandwidth, which improves the energy resolution, but hinders the ability to cover multiple K-edges simultaneously. Conversely, a smaller radius broadens the bandwidth, enabling multiple-element imaging at the expense of resolution. Therefore, the choice of the bending radius of the crystal should be optimized according to the specific imaging task. Large radii are preferred when targeting a single contrast element, whereas smaller radii are more suitable when the goal is to image multiple target elements simultaneously.

Focus dimension

In a crystal-based setup the sample is placed where the beam focuses along the diffraction direction. Consequently, the focal size defines the vertical spatial resolution of the acquired image. By choosing a crystal which matches the magic condition, the focal size can be minimized.

The focal sizes at three different bending radii of the crystal were measured. The X-rays were diffracted around the K-edge of iodine (33.2 keV) and the crystal was a 300 µm thick silicon wafer, with surface pole oriented along ⟨110⟩ and cut at a 2.5° angle relative to the utilized $(\bar{2}20)$ reflection. The crystal was bent to 0.5 m, 1.0 m, and 1.5 m, and the focus profile was fitted with a Gaussian function, and the FWHM was used to quantify the focal dimension. The detector had a pixel size of 7.5 µm. The results are reported in Table 4.2.

TABLE 4.2: Measured focal sizes at three different banding radii, namely 0.5 m, 1.0 m, and 1.5 m.

Bending radius (m)	**Measured focus dimension (µm)**
0.5	31.6 ± 1.1
1.0	29.5 ± 0.9
1.5	32.0 ± 1.1

The measurements show that the focus dimension remains constant within the error bars across the three different bending radii. The focal size should have a dependence on the bending radius since, as seen in Equation 2.14, it is determined by both the crystal's focal distance, which usually corresponds to half the bending radius, and by the spread of the parallel diffracted rays, which is also affected

by the bending radius. However, the main dependence is on the size of the source, which is fixed. Moreover, although the crystal was cut with an asymmetry angle chosen to match the magic condition, there could be a slight mismatch making the magic condition not fully satisfied, thereby affecting the focal size. Nevertheless, the measured focal dimensions confirm that the focus remains sufficiently small for high-resolution imaging.

4.2.2 *Simulation*

In the context of the project, a MATLAB simulation was written to simulate the imaging performance of a SKES setup.

Sophisticated programs simulating the diffraction properties of elastically bent Laue crystals already exist, such as SHADOW [Rio et al. 2011], SRW [Chubar and Elleaume 1998], or OASYS [Rebuffi and Rio 2017]. SHADOW is a ray-tracing software package used to simulate and optimize X-ray beamlines and optical systems for synchrotron radiation facilities, while SRW computes synchrotron radiation from relativistic electrons and simulates how the radiation propagates through optical elements and drift spaces. OASYS instead is a graphical environment for modeling X-ray experiments in Python.

Although the mentioned software programs are really sophisticated and widely used, there is no dedicated tool for the simulation of the magic condition for bent Laue crystals along with the image formation.

The simulation I worked on was based on a pre-existing ray-tracing tool developed by our group specifically for SKES. This section describes the simulation framework and the modifications implemented to improve its accuracy and performance, describing the photon path from its creation to its hit on the detector. A sketch of the simulation geometry can be seen in Figure 4.6.

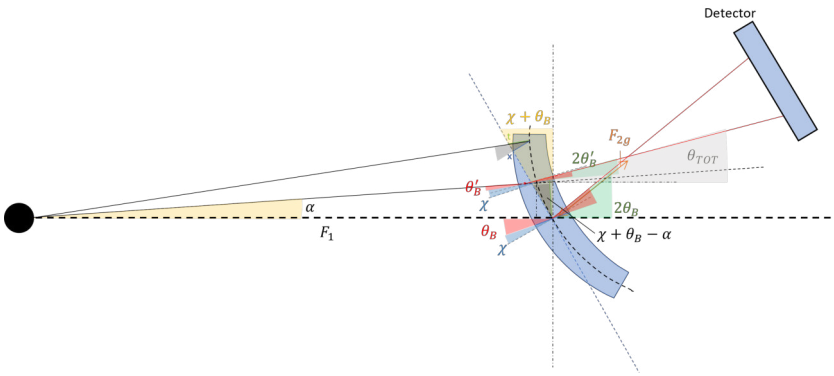

FIGURE 4.6: Sketch of the simulation geometry.

A photon is emitted at a distance F_1 from the center of the crystal, with an angle α with respect to the horizontal, randomly generated

between $-\alpha_{max}$ and α_{max}. The photon then propagates towards the crystal and diffracts.

The function responsible for determining the photon–crystal interaction point, diffraction angle, and photon energy, was significantly revised. In its original implementation, the function assumed a flat crystal geometry, neglecting the tilting of the crystal planes. As a result, to ensure that the photons converged at the focus, the diffraction angle was determined so that each photon's trajectory intersected the path of a hypothetical photon diffracted at the center of the crystal (exactly at Bragg's angle) at the polychromatic focal position. The monochromatic focal distance F_{2g} was taken as input and did not consider bending effects or curvature-related focusing.

To address these limitations, my improvement for this function consisted in using a quadratic equation to find the intersection of the photon trajectory with the bent crystal plane. The calculation accounts for the crystal thickness, curvature (through the bending radius R). A detailed description of the geometry underlying photon diffraction is provided in Appendix B.2. Once the diffraction angle is known, the diffracted photon energy can be obtained:

$$E = \frac{12.398419 \times 10^{-10}}{2d \sin\theta}$$

With this updated approach, the geometric and polychromatic foci arise naturally as a result of the photon-crystal interaction. When the asymmetry angle is chosen to satisfy the magic condition, these two foci coincide, yielding optimal focusing and energy dispersion properties.

The energy dispersion model was also refined. A random energy blurring between 0 and ΔE_{max} is applied to each photon. In the earlier version of the simulation, only fewer contributions to energy dispersion were accounted for. Three additional contributions contributions were incorporated into the model, as detailed in Appendix B.1.

Another major development involved the inclusion of quasi-mosaicity effects, implemented in collaboration with colleagues from INFN Ferrara [Camattari et al. 2015]. A quasi-mosaic crystal consists of small crystalline domains (mosaic blocks) with slight angular misorientations. The quasi-mosaic radius (RQM) characterizes the size scale of this mosaic structure, and governs how the crystal's reflecting properties vary spatially. The updated code modifies the diffraction angle based on the crystal model selected according to the RQM:

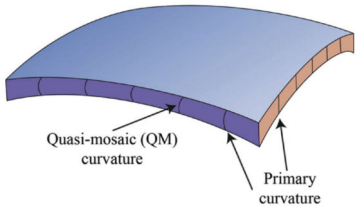

Figure x: Quasi-mosaic curvature of a crystal. Figure taken from [Camattari et al. 2015].

1. Small RQM ($< 10^3$): Curved Dispersive Plate (CDP) model

2. Large RQM ($> 10^3$): Coarse mosaic, Flat crystal model

The simulation calculates the RQM along the crystal's bending direction based on the crystal's properties (see Table 4.3). It first selects the appropriate compliance parameters for the specified material and orientation. Then, using these parameters and the bending direction, it computes the Poisson ratio and the RQM, which quantify the induced secondary curvatures due to the crystal's elastic properties.

The function also returns the diffraction efficiency: for each photon, its diffraction probability is computed. Each photon is then accepted or rejected according to a Monte Carlo criterion. Diffraction occurs only if the calculated probability exceeds a random number between 0 and 1.

Once the photon is diffracted and therefore its energy is defined, it propagates through space until it reaches the sample. In the current implementation, for simplicity, the simulation generates cylindrical samples. Nevertheless, this can be easily extended to more complex geometries by modifying the sample generation function. The sample is placed in the geometrical focus, and each photon traverses the sample undergoing attenuation before reaching the detector. The attenuation accounts for the photon's angle, and a transmission probability is assigned according to Lambert-Beer's law. As for the efficiency calculation, the photon is transmitted only if a randomly generated number between 0 and 1 does not exceed the calculated transmission probability.

Finally, the simulation tracks the photon to the detector plane, where its coordinates are recorded. The photon hits are binned according to the chosen pixel size of the detector, and a Gaussian 2D filter is applied to the resulting image to account for the detector's point spread function. Because the photon energy is mapped along the vertical detector axis, each image corresponds to a single line of the sample. To obtain a 2D projection, vertical scanning of the sample is required. For tomographic imaging, the whole process is repeated for the chosen number of projections while rotating the sample.

All the parameters that can be tuned to achieve the desired setup are listed in Table 4.3.

The simulation was used to identify the most suitable crystal orientation for the experimental setup, and subsequently to evaluate its accuracy in predicting the energy resolution.

Three crystal orientation were considered: (100), (110) and (111). Their influence on the diffraction efficiency and energy resolution was evaluated. For this scope, a 300 µm thick crystal was selected, and the simulation was ran at an energy of 33 keV, a representative energy routinely used in our experiments. The results are presented in Figure 4.7, top.

The results indicate that crystal orientation has only a minor effect on efficiency and energy resolution. Still, the (100) orientation

TABLE 4.3: List of simulation parameters divided into categories.

Parameter Category	Parameter	Units
Imaging Setup	Source-to-crystal distance	m
	Crystal-to-detector distance	m
	Half source divergence (FWHM)	rad
	Selected energy	keV
	X-ray source size	m
	Number of projections	–
	Photons per column	–
Crystal Properties	Bending radius	m
	Asymmetry angle	rad
	Poisson ratio	–
	Crystal thickness	m
	Silicon lattice spacing	m
	Reflection type	(h k l)
	Material	–
	Quasi-mosaic radius	m
Detector Specs	Pixel size (horizontal × vertical)	mm
	Detector dimensions	mm
	Point spread function (σ)	pixels
Sample Properties	Sample position	cm
	Cylinder radius	cm
	Material type	–
	Atomic number	–
	Density	g/cm^3

was selected as it provided the highest efficiency and lowest energy resolution among the three options.

Then, the (100) orientation was fixed, and the effect of crystal thickness was studied across three energies: low, middle, and high energies relative to our typical working energy range. The results are shown in Figure 4.7, bottom.

The analysis shows that at low energies, a thinner crystal (100 µm) optimizes both efficiency and resolution. At intermediate energies, a thinner crystal is still preferred, whereas at higher energies, a thicker crystal (500 µm) yields better performance.

Another key parameter affecting the system's performance is the crystal bending radius. Efficiency and energy resolution were evalu-

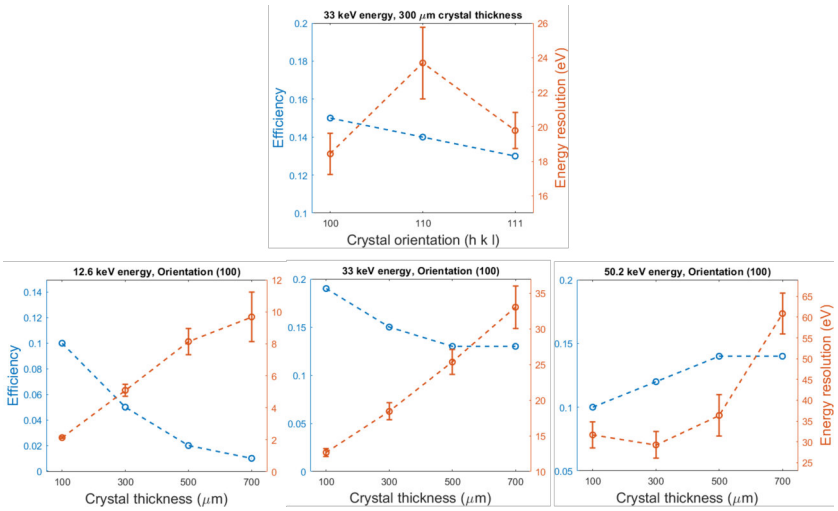

FIGURE 4.7: Top: Efficiency (left ordinate) and energy resolution (right ordinate) as a function of the crystal orientation for a 300 µm thick crystal at 33 keV. Bottom, from left to right: Efficiency and energy resolution (eV) as a function of crystal thickness for a (100)-oriented crystal at low, middle, and high energy, respectively.

ated at three bending radii: 0.5 m, 1.0 m, and 1.5 m, corresponding to the available benders used in our experimental setup. The crystal asymmetry angle was set at 3°. The results are presented in Figure 4.8.

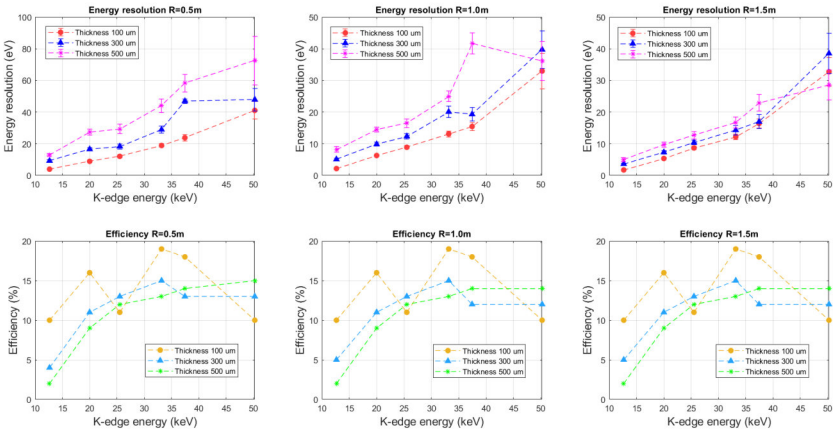

FIGURE 4.8: Top, from left to right: energy resolution (eV) as a function of energy for different crystal thicknesses at bending radii of 0.5 m, 1.0 m, and 1.5 m, respectively. Bottom, from left to right: efficiency as a function of energy for different crystal thicknesses at bending radii of 0.5 m, 1.0 m, and 1.5 m, respectively.

The energy resolution plots reveal two clear trends for energy resolution. First, energy resolution increases with crystal thickness, and second, the energy resolution decreases with increasing bending radius. Both trends are expected, since the dominant contribution to energy resolution is directly proportional to the crystal thickness and inversely proportional to the crystal's curvature (see Appendix B.1).

For efficiency, the results show that thinner crystals yield higher efficiency. This is attributed to the fact that thicker crystals absorb more photons and reduce the effective volume available for diffrac-

tion. As expected, the bending radius has a negligible influence on efficiency.

Another study consisted of a direct comparison between the experimentally measured energy resolution and the corresponding simulated values. The experimental data has previously been described and presented in Section 4.2.1. Figure 4.9 reports the comparison for three different crystal bending radii (0.5 m, 1.0 m, and 1.5 m).

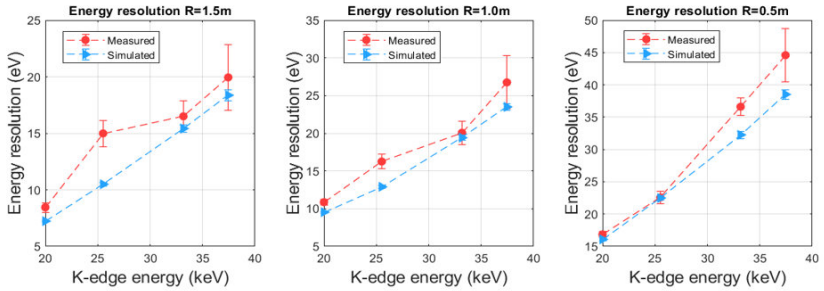

FIGURE 4.9: Comparison between simulated and experimentally measured energy resolution at three crystal bending radii (1.5 m, 1.0 m, and 0.5 m).

The results show good agreement between simulation and experiment. Except for the energy resolution measured at silver's K-edge at a bending radius of 1.5 m, all simulated values are compatible with the measured ones within three standard deviations. The measured values agree with simulations with root mean square errors (RMSEs) of 2.5 eV, 2.4 eV, and 3.7 eV for bending radii of 1.5 m, 1.0 m, and 0.5 m, respectively. This agreement demonstrates the reliability and predictive power of the simulation in modeling the output of the experimental setup under different geometrical conditions.

A final study compared the experimentally measured focus dimensions (Table 4.2) with the simulated values under identical conditions, as summarized in Table 4.4.

TABLE 4.4: Measured and simulated focal sizes at three different banding radii, namely 0.5 m, 1.0 m, and 1.5 m.

Bending radius (m)	**Measured focus dimension (μm)**	**Simulated focus dimension (μm)**
0.5	31.6 ± 1.1	33.8 ± 0.3
1.0	29.5 ± 0.9	34.0 ± 0.2
1.5	32.0 ± 1.1	34.2 ± 0.2

The simulated values slightly overestimate the measured focal sizes. Nevertheless, the results remain consistent and confirms the simulation's predictive capability.

4.2.3 *A mask visibility study*

A mask-specific study was conducted to investigate how detector spatial resolution influences mask visibility. This work is published as a conference proceeding in [Perion et al. 2025a].

In modulation-based X-ray phase-contrast imaging, mask visibility is typically defined as the ratio between the standard deviation and the mean value of the pixel intensity measured from a chosen region in the mask image. The primary focus of this study is to investigate the influence of detector spatial resolution on mask visibility. Three different scintillator-coupled scientific CMOS detectors, with varying pixel sizes and scintillator thicknesses, were tested to highlight the difference in response in terms of visibility from a given mask. Additionally, the impact of visibility on the image quality in refraction images was investigated through a wave optics simulation. The results showcase the trends of contrast and signal-to-noise ratio values as a function of mask visibility.

In the previous chapters, it has already been thoroughly addressed how the beam tracking X-ray phase-contrast imaging works. It is unsurprising that, when imaging the beamlets, an accurate mapping of their intensity distribution is crucial for retrieving quantitative information on X-ray absorption, refraction, and scattering. Since the beamlets usually feature width in the order of tens of micrometers, the beam tracking technique requires a high-resolution detector, generally with a pixel size smaller than 10 μm.

A crucial parameter which is linked to the final overall quality of the retrieved images is the mask visibility, which is defined as the ratio of the standard deviation to the mean intensity value of pixels, measured from a chosen region of interest within the mask image when no sample is in the beam [Zdora 2018].

In this study, experimental images of the same beam tracking mask were acquired using three different off the shelf detectors with different pixel sizes and scintillator properties, thus different point spread functions (PSFs), revealing significant differences in their response in terms of visibility. To investigate how the detector's PSF, which strongly affects mask visibility, impacts the quality of refraction images, a simulation study was conducted. Specifically, the visibility of the mask influences the retrieval algorithm's ability to accurately capture the changes in the beamlets caused by the insertion of the sample by introducing potential crosstalk between adjacent beamlets. For this reason, the present analysis focuses on evaluating image contrast and signal-to-noise ratio (SNR) in refraction images of a Nylon wire obtained from detectors with different PSFs (i.e. images with varying visibilities). This work establishes the relationship between detector configuration and imaging performance, which is crucial for optimizing the beam tracking technique in X-ray phase contrast

imaging.

The integration of an optimal high-resolution detector in the setup is fundamental for both spectral energy resolution and phase-contrast signal retrieval, ensuring the effectiveness of the combined spectral and phase-contrast imaging techniques for advanced imaging applications.

Materials and methods

Mask visibility is a crucial parameter in the beam tracking technique, as it is strictly linked to the ability to detect changes in the beamlets. A beam tracking mask typically consists of a highly absorbing material, which ideally absorbs all the X-rays, alternated, in the horizontal direction, with periodic apertures that transmit the beam (see Figure 4.10a). This arrangement shapes the beam into multiple beamlets, whose size corresponds to the width of the apertures in the mask. In this scenario, the visibility of the mask is defined as:

$$visibility = \frac{\sigma}{\mu} \tag{4.3}$$

where the σ is the standard deviation and μ is the mean intensity, both calculated from a selected bidimensional region of interest within the mask image when no sample is in the beam. Visibility quantifies the extent of the modulation pattern of the beamlets within the image. A higher visibility indicates a reduced crosstalk between beamlets, facilitating the extraction of absorption, refraction, and dark field information.

Experimental setup:

A mask with a 61 µm period and 10 µm aperture (Mask 1, see Figure 4.10b and 4.10c), composed of a 1 mm thick graphite substrate and 250 µm thick gold septa, was imaged experimentally using three distinct scintillator-coupled scientific CMOS imagers. The purpose of this imaging was to evaluate the detectors' responses in terms of visibility and assess their suitability for our experimental setup. These detectors, referred to as Detector 1, 2, and 3 in this work, featured different pixel sizes (7.5 µm, 6.5 µm and 3.76 µm) and varying gallium-based scintillator thicknesses (10 µm, 20 µm, 10 µm, respectively). In detectors with gallium-based scintillators, the scintillator is composed of a powdered material, so its thickness does not correspond to a continuous layer but rather to an effective thickness that accounts for the packing density of the powder. The detectors were positioned at approximately 1 m from the mask, and images were acquired using a monochromatic synchrotron beam at an energy of 33 keV. This energy was selected as it corresponds to the K-edge of iodine, which is a typical contrast agent used in spectral

imaging. The experiments with Detector 1 and 2 were conducted at the Syrmep beamline of Elettra Sincrotrone Trieste, whereas those involving Detector 3 were performed at the BM05 beamline of the European Synchrotron Radiation Facility (ESRF). Moreover, Syrmep's white beam, lens-coupled high-resolution detector, with a pixel size of 4 µm, was used to image a nylon wire, validating the simulation program's outputs.

FIGURE 4.10: a) Sketch of a standard mask used in beam tracking phase-contrast imaging alternating apertures with high absorbing material. b) Microscopic photo of the mask used in both experiments and simulation. c) Photo of two masks, with the mask on the right corresponding to the one used in the experiments and simulations.

Simulation:

The impact of mask visibility on the quality of refraction images was evaluated using a wave optics simulation developed in MATLAB. The propagation of the X-ray beam is modeled in the simulation using the Fresnel propagator [Goodman 2005]. This simulation can predict outcomes for any mask geometry, including its period and aperture, as well as for any point spread function (PSF) of the detector. Moreover, it can work in both monochromatic and polychromatic beam configurations. In this study, a monochromatic beam was simulated at 33 keV, aligning with the energy used to test the detectors experimentally.

The mask used in the simulation replicated the characteristics of the experimental mask, with a 61 µm period and a 10 µm aperture (Mask 1 shown in Figure 4.10b and 4.10c). The simulated high-resolution detector had a pixel size of 4 µm, consistent with the typical configuration used for micro-tomography experiments performed at the Syrmep beamline in white beam mode [Donato et al. 2022], and close to the pixel sizes of the three detectors tested experimentally. For simplicity purposes, its PSF was assumed to be Gaussian. To assess the effect of mask visibility on image quality, we fixed the mask period, aperture, and detector pixel size, while varying the full width at half maximum (FWHM) of the detector PSF. This procedure changes the final visibility in the mask image, allowing the study of its influence on image quality. The PSF's FWHM varied from a minimum of 4 µm (corresponding to the detector's pixel size) to a maximum of 61 µm (equal to the period of the mask).

A sample consisting of a 0.35 mm Nylon wire was simulated, and SNR and contrast values were extracted from the resulting refraction images. This sample was chosen as its refraction properties are well

known. These metrics were calculated as follows:

$$C = peak^{+} - peak^{-} \qquad SNR = \frac{peak^{+} - peak^{-}}{\sigma_{bg}} \tag{4.4}$$

where $peak^{+}$ is the positive peak value, $peak^{-}$ is the negative peak value, and σ_{bg} is the standard deviation measured in the background (see Figure 4.12).

Moreover, contrast and SNR values were measured from refraction images simulated with two additional masks (Mask 2 and Mask 3). Both had the same period as Mask 1 (61 µm), but featured different apertures: Mask 2 had half the aperture of Mask 1 (5 µm), while Mask 3 had double (20 µm).

Results

Experimental results:

In order to test the suitability of the three commercial detectors tested for our setup, their responses in terms of visibility were evaluated. A critical factor affecting visibility is the detector PSF, and, consequently, its modulation transfer function (MTF). While quantum efficiency also plays a role, its characterization was beyond the scope of this study.

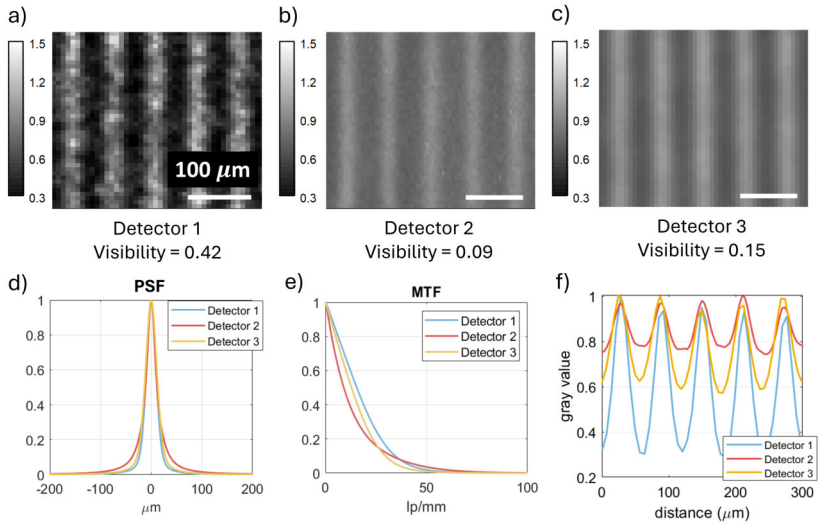

FIGURE 4.11: a), b), and c) Images of a 61 µm period and 10 µm aperture mask acquired with three different detectors and the corresponding visibilities, d) and e) PSF and MTF plots of the three detectors, f) profile plots of a), b) and c). A significant difference in the values of visibility can be observed.

As shown in Figure 4.11, visibility is strongly dependent on PSF and MTF, making its characterization essential to evaluate detector performance in beam tracking phase-contrast imaging. Given the significant differences in terms of visibility and the need to identify the most suitable detector for our setup, the simulation study presented

in the previous section was conducted. Its aim was to quantify how varying detector responses impact the quality of retrieved images in beam-tracking.

Simulation results:

As discussed in the previous sections, the simulation aims to assess how different detector responses, specifically in terms of visibility, affect the quality of refraction images. Figure 4.12a shows the typical refraction image produced by a wire. The peak-to-peak and noise values of the simulated images were used to assess SNR and contrast. For validation, the simulated wire image (Figure 4.12a, right) is compared with an experimental image (Figure 4.12a, left) acquired with Mask 1 using the white beam detector of the Syrmep beamline.

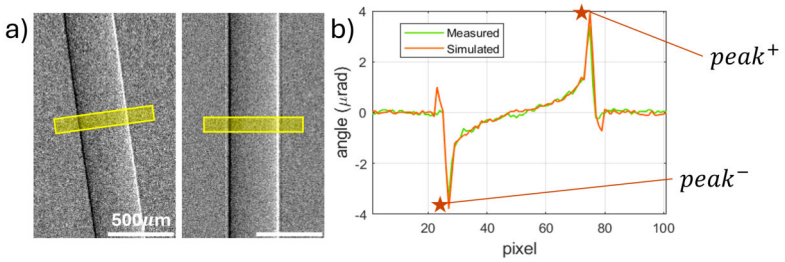

FIGURE 4.12: a) Experimental (left) and simulated (right) refraction images of a 0.35 mm Nylon wire. b) Comparison of the profile plots of the two yellow regions.

The undershoot peaks observed in the simulated profile are not yet fully understood and are most likely caused by contributions that are not accounted for in the simulation. To simulate different detector responses, the detector's PSF FWHM was varied across eight different values and the corresponding SNR and contrast values in refraction images were measured.

Figure 4.13 displays a portion of Mask 1 image for each PSF value, while the corresponding visibility is plotted as a function of the PSF FWHM.

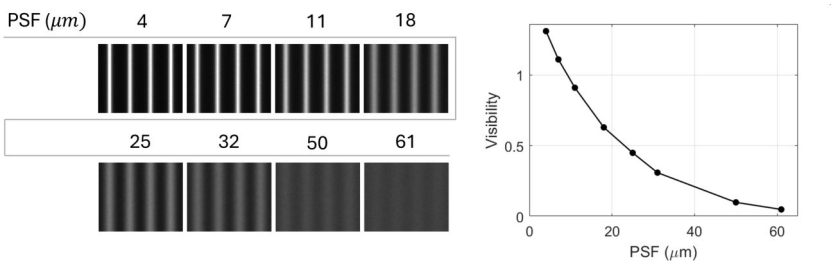

FIGURE 4.13: Regions of interest of Mask 1 image as a function of the detector's PSF FWHM (left). Plot of visibility as a function of the PSF (right).

Subsequently, the refraction images of the Nylon wire were retrieved from the simulated data at 33 keV through a beam tracking algorithm. SNR and contrast values were extracted from the images

and plotted as a function of mask visibility for Mask 1 (see Figure 4.14, a1 and a2).

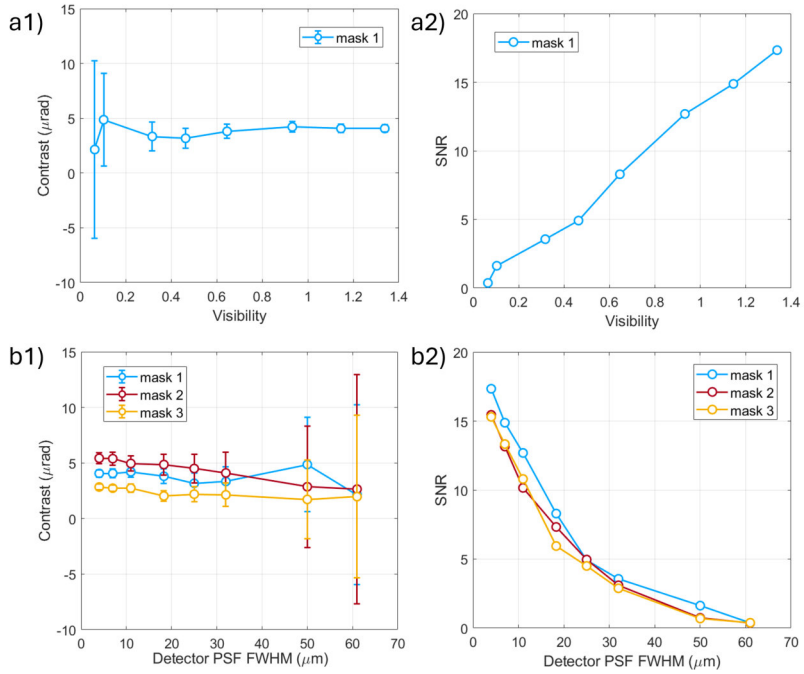

FIGURE 4.14: Contrast (a1) and SNR (a2) values measured from refraction images, obtained with a 61 μm period and 10 µm aperture mask (Mask 1), as a function of mask visibility. Contrast (b1) and SNR (b2) values measured from refraction images, obtained with Mask 1 and two other masks with the same period as Mask 1 (61 µm) but half (5 µm, Mask 2) and double (20 µm, Mask 3) the aperture respectively, as a function of the PSF FWHM.

The results indicate that contrast remains largely constant within the error margins (Figure 4.14, a1), while SNR increases with a near-linear trend (Figure 4.14, a2). Figure 4.14, b1 and b2 display the results for the three mask types. In this case, since different masks may present sightly different visibilities while the PSF remains constant, the results are shown as a function of the PSF FWHM. When comparing masks 1, 2, and 3, Mask 2 consistently yields the highest contrast values (Figure 4.14, b1), while Mask 1 achieves the highest SNR values (Figure 4.14, b2). This can be attributed to the fact that smaller mask apertures improve the spatial resolution of the final image, leading to a better sampling of the wires edges which are responsible for the refraction signal. However, a smaller aperture also results in fewer photons reaching the detector, increasing statistical noise and thus reducing the SNR. Finally, it is worth noting that the uncertainties in the contrast values become very large for wide PSF values. In this case, significant beamlet broadening leads to crosstalk between neighboring beamlets, resulting in highly noisy images in which the retrieval algorithm fails to accurately capture the signal variations.

Conclusions

This study demonstrates the critical role of mask visibility in X-ray phase-contrast imaging in the context of the beam tracking technique. By investigating the effects of different off the shelf detectors with varying pixel sizes and scintillator properties, it has been shown how the detector-dependent mask visibility influences refraction image quality, specifically in terms of contrast and SNR. The findings highlight that while smaller mask apertures can enhance spatial resolution and contrast, they also reduce the photon flux, leading to a decrease in SNR. The detectors used in this study were charge-integrating detectors [Gruner et al. 2002] without single photon sensitivity, which inherently contributes to the overall noise. Future developments employing single photon-counting detectors [Willemink et al. 2018] could improve image quality and overall imaging performance.

4.2.4 *The beam tracking algorithm*

The theoretical background of the beam tracking technique is presented in Section 2.2.2. As introduced, each beamlet created by the absorbing mask is analyzed independently. All beamlets within each image row are extracted and fitted individually. Each beamlet is modeled as a Gaussian function, from which three parameters are determined: amplitude, center, and standard deviation.

An optimized version of the beam-tracking algorithm was developed as part of this work to improve the robustness and reliability of the analysis. The following section describes this improved implementation in detail.

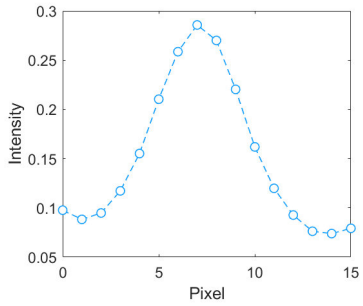

Figure xi: Profile plot of a beamlet detected on the detector using the beam tracking phase-contrast technique.

The typical profile of a beamlet detected on the detector is shown in the margin Figure xi. In this section, the discrete points of the Gaussian profile are denoted by P_i, with $i = 1,\ldots,N$, where N is the number of points within the selected window. The tails of the Gaussian distribution often exhibit asymmetry. This asymmetry arises from fabrication constraints in the absorbing mask: within the absorbing regions, small horizontal bridges where gold cannot be deposited create thin transparent gaps. When the horizontal beamlet profile aligns vertically with one of these bridges, additional photons transmit through the gap, causing one tail of the measured Gaussian to appear higher than the other. When this asymmetry is particularly pronounced, the algorithm may fail in successfully retrieving the desired parameters. To improve robustness, the algorithm first identifies the minimum value in the first half of the points and the minimum value in the second half. A line is then drawn between these two points and subtracted from the profile, normalizing the left and right minima to zero. This preprocessing procedure reduces the impact of asymmetrical tails.

The center of the Gaussian is computed as the first moment of the distribution:

$$\mu = \frac{\sum_1^N x_i P_i}{\sum_1^N P_i}$$

After this, the maximum value of the distribution of points, denoted as $\hat{P}$, is obtained analytically by making a parabola pass through the maximum point of the profile and its two neighboring points. The vertex of the parabola is taken as the peak value of the distribution $\hat{P}$. This approach provides a precise estimate of the peak without performing a curve fit and is essential for the computation of the standard deviation.

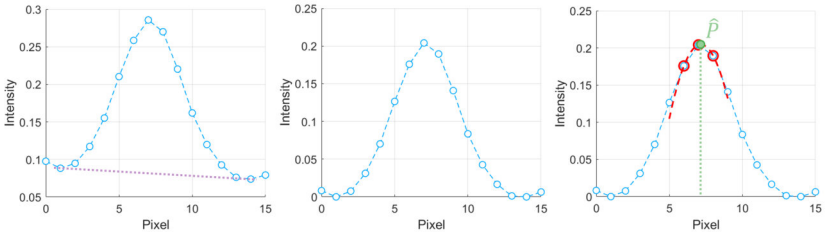

FIGURE 4.15: Steps in the retrieval of area, center, and scattering from a beamlet's profile. First, a line is drawn between the minima on both sides and subtracted from the profile. Then, the maximum value of the distribution of points, denoted as $\hat{P}$, is obtained analytically by making a parabola pass through the maximum point of the profile and its two neighboring points.

The area of the distribution, which is linked to absorption, is calculated as:

$$S = \sum_1^N P_i$$

and the standard deviation is then estimated as:

$$\sigma = \frac{S}{\sqrt{2\pi}\hat{P}}$$

These parameters: area, center, and standard deviation, characterize the Gaussian beamlet profile and are used to retrieve absorption, refraction, and scattering images. The parameters are extracted from both reference (S_{ref}, μ_{ref}, and σ_{ref}) and sample images (S_{sam}, μ_{sam}, and σ_{sam}). The final absorption, refraction, and scattering images are calculated on a pixel-by-pixel basis as:

$$abs = \frac{S_{sam}}{S_{ref}}$$
$$ref = \mu_{sam} - \mu_{ref}$$
$$sca = \sigma_{sam}^2 - \sigma_{ref}^2$$

4.2.5 *The SYRMEP beamline*

After describing the various optimization studies, we now turn to the experimental setup developed at the SYRMEP beamline.

The SYRMEP (SYnchrotron Radiation for MEdical Physics) beamline has been designed by Elettra Sincrotrone Trieste, in collaboration with the University of Trieste and INFN, for research in medical diagnostic radiology, material science, cultural heritage, and life science applications [Tromba et al. 2010; Longo et al. 2024].

The Elettra synchrotron radiation source, which is a bending magnet, can operate at 2 GeV or 2.4 GeV, and the beamline can work both in monochromatic and white beam configurations, in an energy range from 10 keV to 40 keV. SYRMEP can perform multiscale X-ray imaging using pixel sizes ranging from 100 µm down to the sub-µm scale. The availability of long propagation distances (from 0 to 2 m; 3.5 m and from 9.5 to 11 m) makes the beamline well suited for propagation-based phase-contrast imaging.

The beamline is divided into three different sections:

1. The optical hutch, accommodating optical elements and slits, where the beam is prepared for the experiment

2. The experimental hutch, where the experiment takes place, which houses optical tables for instrument alignment, motion stages for sample positioning, and detector for data acquisition

3. The control room, where the control boards are, from which the beamline and experimental operations are managed.

The white-beam detector is a Hamamatsu Orca Flash sCMOS camera with a 2048 × 2048 matrix of pixels, coupled with an optical magnification system which allows pixel size tuning. Figure 4.16 shows a photo of the experimental hutch of the beamline.

4.2.6 *Setup A*

The goal of the SPHERE-X project was to develop a novel experimental setup that combined crystal-based spectral imaging with beam tracking phase-contrast imaging at the SYRMEP beamline of the Elettra synchrotron in Trieste.

The system was mounted and tested on multiple samples during various beamtimes. In this section, the experimental setup is described in detail, followed by an outline of the image processing workflow and a presentation of the image results. The results demonstrate the system's ability to deliver complementary morphological and compositional information with high spatial resolution and quantitative accuracy.

FIGURE 4.16: Photograph of the beamline's experimental hutch. The detector is not shown as it is placed downstream.

Experimental Setup

A schematic and a photograph of the experimental setup are shown in Figure 4.17.

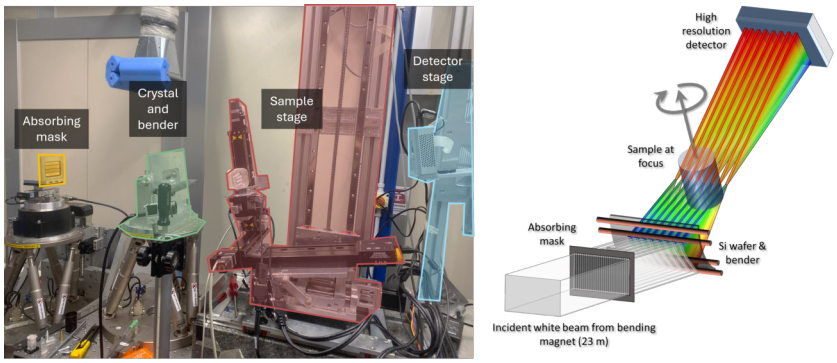

FIGURE 4.17: Photograph (left) and sketch (right) of the experimental setup with the main components highlighted.

A more detailed side-view schematic, including all motor components, is provided in Figure 4.18.

Following the beam trajectory, the first element encountered is the absorbing mask. The custom-designed mask consisted of an array of five different masks, which were tailored to be versatile and suitable for different detectors. The aperture and pitch dimensions are summarized in Table 4.5. Four of the masks featured one-dimensional apertures, while the fifth has two-dimensional circular apertures. Each one-dimensional mask is 10 mm × 60 mm, while the two-dimensional mask is 30 mm × 30 mm. A sketch of the array of masks is shown in the margin Figure xii.

The absorbing masks are fabricated from a 250 µm thick gold layer deposited on a graphite substrate of 500 µm thickness. They were mounted on a PI-L511 translation motor [Physik Instrumente 2025b], which enabled precise horizontal displacements for dithering

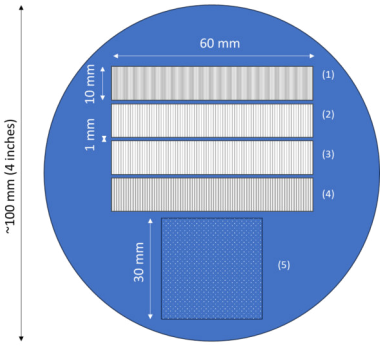

Figure xii: Sketch of the array of masks. Masks 1-4 feature vertical apertures (one-dimensional), while mask 5 has circular apertures (two-dimensional).

TABLE 4.5: Type, aperture (μm), and pitch (μm) of the five designed masks.

Mask number	Type	**Aperture (μm)**	**Pitch (μm)**
1	1D	5	60
2	1D	10	70
3	1D	25	75
4	1D	10	110
5	2D	11.5	100

during data acquisition. The motor-mask structure was mounted on a hexapod [Physik Instrumente 2025a], a six-axis precision stage that allowed fine alignment of the mask with respect to the incident beam at the beginning of each experiment.

After passing through the mask, the beam is shaped into beamlets and reaches the crystal. The distance between the mask and the crystal varied between experiments, as it does not affect imaging performance, but was typically about 30 cm.

The crystal was a 300 μm thick silicon wafer (Siltronic), mounted on a bender. Depending on the bender employed, the wafer could be bent to radii of 1.5 m, 1.0 m, 0.5 m, or 0.3 m. The crystal surface pole was oriented along ⟨110⟩ and cut at a 2.5° asymmetry angle relative to the utilized $(\bar{2}20)$ reflection. The bender structure allows a coarse tilting of the crystal to the nominal Bragg angle. Fine angular tuning was then performed using the PI hexapod, which allowed both vertical alignment of the crystal with the beam and accurate adjustment of the Bragg angle to ensure that the desired reflection was observed on the detector.

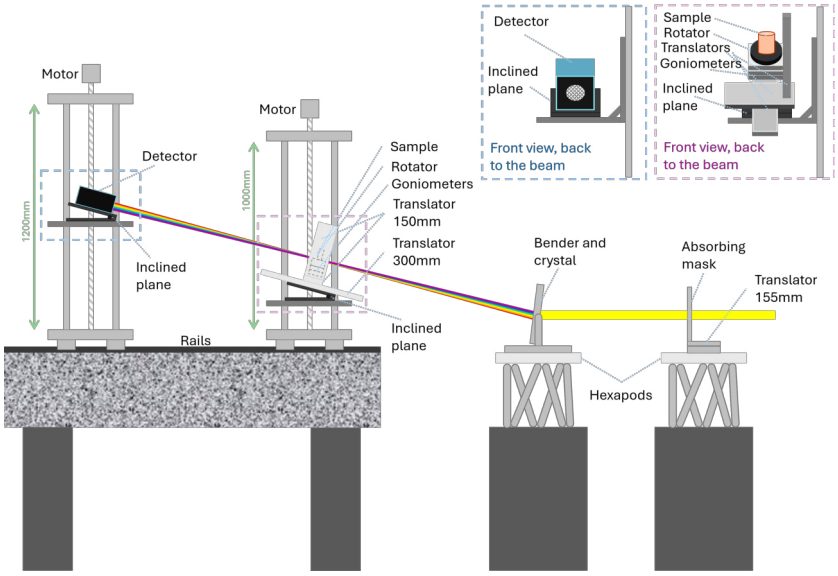

FIGURE 4.18: Detailed side-view schematic of the experimental setup, including all motor components. The front views of the sample stage and detector stage are shown at the top right of the figure.

After being diffracted by the crystal at a chosen energy spectrum, the photons reach the sample, which is placed in the focus of the convergent beam. The focus is usually nominally located at half the bending radius of the crystal; however, its exact position was determined experimentally using an ADVACAM MiniPIX detector [Advacam 2025]. This detector was mounted at sample position and was translated along the diffracted beam path until the minimum vertical beam size was found. In all measurements, the experimental focus was found within a few millimeters from its nominal position.

The sample stage was designed to provide precise positioning and flexibility for both planar radiography and tomography. From bottom to top, it consists of:

- An inclined plane, fixed at twice the chosen Bragg angle
- A 300 mm Thorlabs linear translation stage aligned with the diffracted beam, used to position the sample right in the focus [Thorlabs 2025]
- A 150 mm PI linear translation stage mounted horizontally with respect to the beam, enabling lateral alignment of the sample [Physik Instrumente 2025c]
- A 150 mm PI linear translation stage mounted vertically, used to perform vertical scanning steps of the sample during data acquisition [Physik Instrumente 2025c]
- Two Zaber goniometer stages for fine angular adjustments during the alignment for tomography [Zaber 2025a]
- A Zaber motorized rotation stage, allowing sample rotation during tomographic acquisition [Zaber 2025b]

The entire sample stage was mounted on a vertical translation tower with a travel range of 1 m. This additional degree of freedom enabled to operate flexibly across different photon energies, ensuring that the diffracted beam could always intercept the sample in the correct position.

After passing through the sample, the photons finally reach the detector. The detector is mounted on an inclined plane, fixed at twice the chosen Bragg angle, and the entire stage is supported by a second vertical translation tower with a travel range of 1.2 m. This extended range was necessary because the detector is positioned higher with respect to the sample to intercept the diffracted beam.

The detector varied across different beamtimes, as several options were evaluated and tested. In the end, the ORCA-Lightning X-ray sCMOS Camera from Hamamatsu Photonics was selected for the final experiment. The specifications of this detector will be described in later sections, when the imaging results obtained with it are presented.

Image processing

The images acquired with this setup simultaneously contain both spectral and phase-contrast information. Each raw image is of the type shown in Figure 4.19.

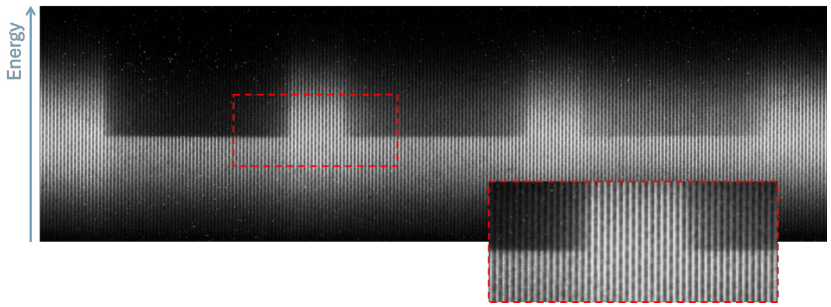

FIGURE 4.19: Example of raw image of three cuvettes filled with different dilutions of silver and water. The beamlets created by the absorbing mask for beam tracking are clearly seen, as well as the vertical energy dispersion along with the K-edge of silver.

The raw images are first corrected by dark subtraction and flat-fielding. Depending on the type of acquisition, the data was collected either in radiographic or tomographic mode. The imaging system, however, enables the acquisition of a single row at a time, roughly corresponding to the vertical dimension of the focus. For this reason, to obtain the full 3D information of the sample, a vertical scan is required.

After dark-subtraction and flat-fielding are applied, the beam tracking algorithm described in Section 4.15 is performed on the projection images. This procedure retrieves the three signal contributions, namely absorption, refraction, and dark-field, along one line of the sample, but resolved across the energy spectrum diffracted by the crystal.

The same process is repeated for each vertical step if scanning is performed, or for multiple projections in the case of tomography. For tomographic data, reconstruction is carried out on absorption and dark-field images directly, while refraction data is first integrated to recover the phase. This integration is performed using a Wiener-filter regularized phase integration algorithm, yielding integral phase projections. All resulting projections are reconstructed using standard filter back-projection with a Shepp-Logan filter, producing three tomographic volumes (absorption, phase, and dark field).

Since each slice is resolved over multiple energies, the images are calibrated in energy, and finally a spectral material decomposition algorithm (Section 2.1.2) is applied, enabling the generation of quantitative maps or volumes of the elements of interest.

Results

In this section, some results obtained during the various beamtimes that we performed are shown. As mentioned earlier, the detector changed across different beamtimes, because different options were tested.

Flower Sample

This sample was designed as a test to assess the overall performance of the imaging system and its ability to resolve absorption, refraction, and dark field contributions.

The sample consisted of two cuvettes containing silver dilutions with nominal concentrations of 3.2 mg mL^{-1} and 6.4 mg mL^{-1}, respectively, a tube filled with polymethyl methacrylate (PMMA) microspheres with a diameter of 48 µm, and some vegetable fragments. A schematic of this sample is shown in Figure 4.20.

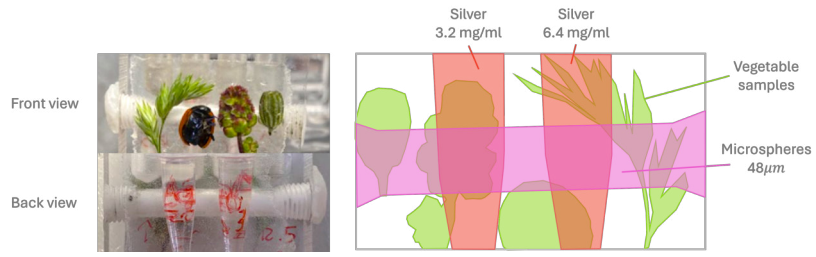

FIGURE 4.20: Photo of the front and back (left), and schematic (right) of the sample.

During this beamtime, image acquisition was performed using the Ximea CMOS camera featuring a pixel size of 3.76 µm and a active sensor area of 53 mm × 40 mm. The measurements were carried out in planar mode, with 340 vertical steps of the sample, using an exposure time of 0.5 s. The absorbing mask featured 20 µm wide apertures with a 119 µm pitch. To increase spatial sampling, six mask dithering steps were performed.

The crystal consisted of a 300 µm thick silicon wafer, bent to a radius of 0.5 m. The surface pole was oriented along ⟨110⟩ and cut at a 2.5° asymmetry angle relative to the utilized $(\bar{2}20)$ reflection. The system was tuned to diffract X-rays around the K-edge of silver (25.5 keV). The sample to detector distance was 56 cm.

The imaging results are shown in Figure 4.21.

Absorption, refraction, and dark field images were successfully retrieved from the acquired dataset. The refraction image was subsequently integrated along the horizontal direction to obtain the corresponding phase image. Some halo artifacts are visible in the phase image: these originate from outlier pixel intensities during integration. While such artifacts are usually averaged out in tomographic reconstructions, they remain visible in planar images. From the absorption images acquired around the K-edge of silver, silver

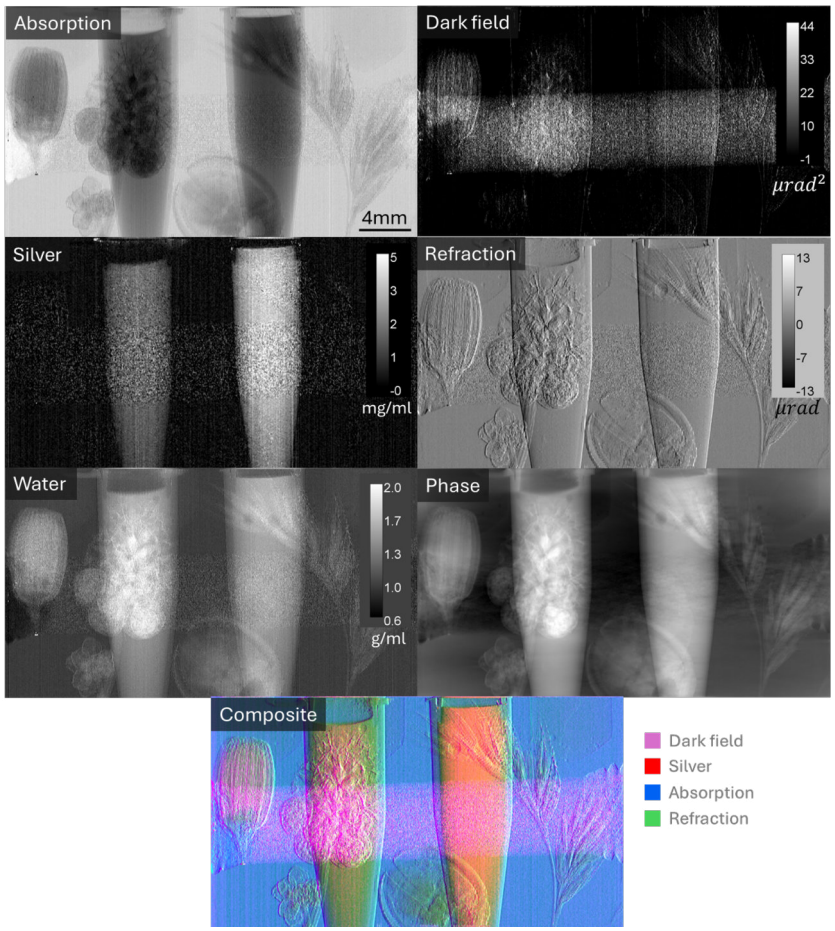

FIGURE 4.21: Absorption, dark field, refraction, and phase images, along with the silver and water maps resulting from the material decomposition algorithm. A composite map showing all the different contributions is shown.

and water density maps were obtained. Silver concentrations were quantified by selecting small regions of interest (ROIs) and measuring their mean intensities. The associated errors correspond to the standard deviations of these measurements. Results are reported in Table 4.6.

TABLE 4.6: Expected and measured densities of silver inside the cuvettes.

	Expected	**Measured**
Silver concentration (mg/mL)		
	3.2	3.5 ± 0.7
	6.4	6.7 ± 0.6

The measured values are in good agreement with the expected silver concentrations, within the estimated uncertainties. Overall, this test demonstrated that the imaging setup is capable of resolving and quantifying absorption, phase, and dark field.

Eight cuvette planar sample

This sample was designed to evaluate the system's capability to simultaneously quantify iodine and retrieve dark-field.

It consisted of four cuvettes containing iodine solutions with nominal concentrations of 7.5 mg mL^{-1}, 5.0 mg mL^{-1}, 2.5 mg mL^{-1}, and 1.0 mg mL^{-1}, and four cuvettes filled with PMMA microspheres of nominal diameters 85 µm, 48 µm, 15 µm, and 8 µm, used to generate dark-field contrast. Finally, a 200 µm polyethylene terephthalate (PET) wire and a 350 µm nylon wire were included in the sample. A schematic of this sample is shown in Figure 4.22.

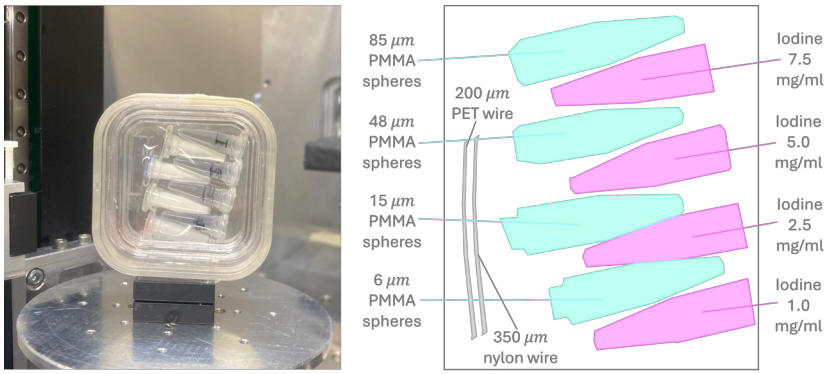

FIGURE 4.22: Photograph and schematic of the sample.

Image acquisition was performed in radiogaraphic mode using a Hamamatsu CMOS camera featuring a pixel size of 6.5 µm and an active sensor area of 2048 pixels × 2048 pixels. Owing to the large sample size (3.5 cm × 4.0 cm), three horizontal scans were required to cover its full width, while the vertical extension of the sample was acquired in 820 vertical steps of 50 µm each. The exposure time per frame was 0.125 s.

The absorbing mask featured 10 µm wide apertures with a 70 µm pitch, and seven dithering steps were performed to improve spatial sampling. The crystal used in this experiment was the same as the one used for the previous sample. The system was tuned to diffract X-rays around the K-edge of iodine (33.2 keV), and the sample to detector distance was 44 cm.

The imaging results are shown in Figure 4.23, while quantitative results are presented in Table 4.7.

The images show a successful retrieval of absorption, refraction and dark-field. The vertical-striped artifacts visible in the refraction and dark-field images are most likely caused by the stitching process used to combine the multiple scans. The absorption data was further processed using the SKES material decomposition algorithm to obtain water and iodine density maps, which were accurately discriminated.

The quantitative analysis shows good agreement between the measured and nominal iodine concentrations, with relative errors

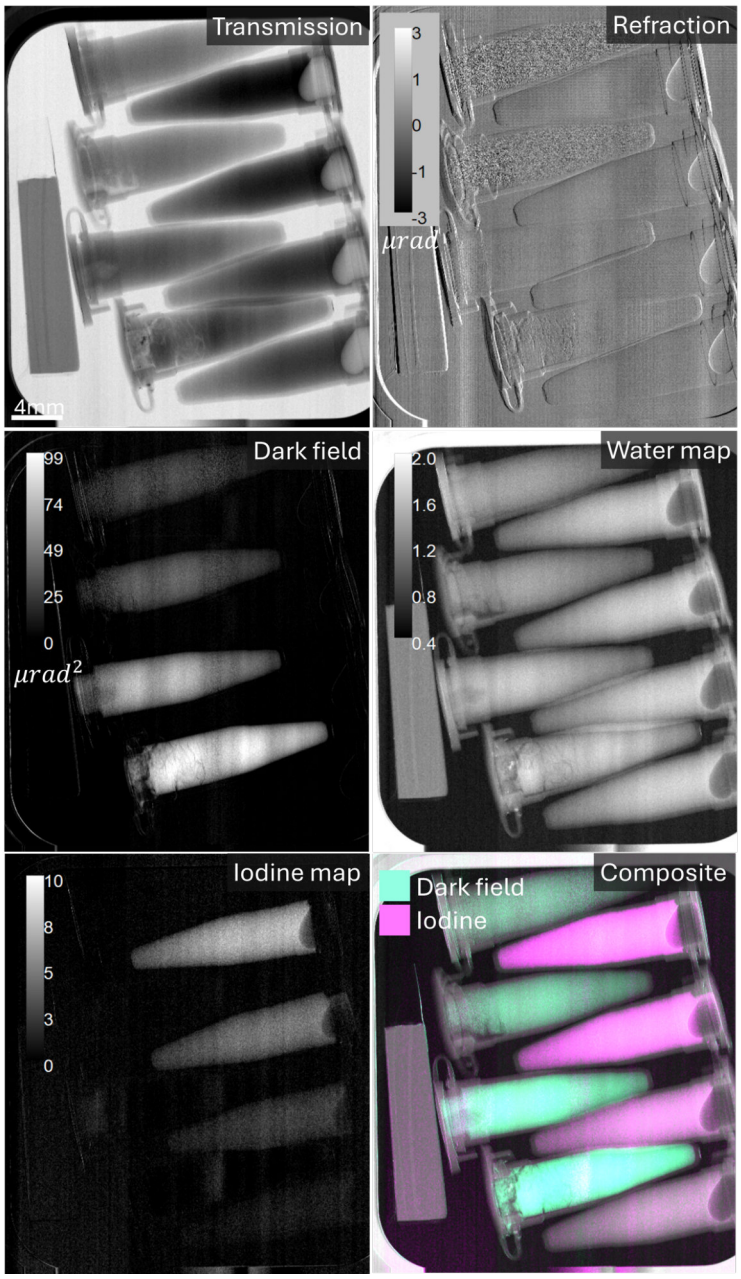

FIGURE 4.23: Absorption, dark field, refraction, and phase images, along with the iodine and water maps resulting from the material decomposition algorithm. A composite map showing iodine and dark field overlaid on the water map is shown in the bottom right.

staying below 8 %. Concerning the dark-field results, it is difficult to define a nominal reference value. However, the expected behavior can be derived from Equation 1.14. Specifically, the angular spread of the beam due to scattering scales with $N^{1/2}$, which means that its square should vary as N, which, for a fixed thickness, is proportional to p_f/R. The packing fractions of the cuvettes were determined by weighing them before and after inserting the spheres. The experimental data, plotted as a function of the ratio p_f/R, is shown in Figure 4.24.

The data is consistent with the theoretical trend. Minor deviations

TABLE 4.7: Expected and measured iodine densities for the iodine-filled cuvettes, and measured dark-field signal for the PMMA-filled cuvettes. For both datasets, the measurements are reported in order from the top to the bottom cuvette. For the dark-field, the calculated packing fractions p_f and the radii R are also reported.

			Expected	**Measured**
Iodine concentration				
(mg/mL)			7.5	7.24 ± 0.57
			5.0	4.65 ± 0.56
			2.5	2.30 ± 0.52
			1.0	1.02 ± 0.53
Dark field	p_f	$R\ (\mu m)$		
(μrad^2)	0.37	42.5	—	25.8 ± 2.0
	0.32	24	—	36.5 ± 2.9
	0.35	7.5	—	68.2 ± 3.0
	0.25	4	—	94.3 ± 4.2

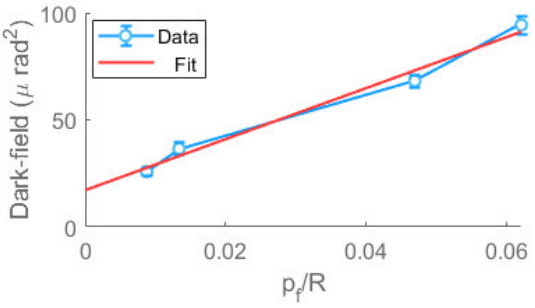

FIGURE 4.24: Dark-field signal as a function of the ratio p_f/R, with a linear fit.

from linearity may arise from slight variations of the packing fraction within each cuvette, but overall the results confirm that the system accurately captures the expected dependence of the dark-field signal on the scatterer size.

Multiple K-edge revolvers

For the first time, it was possible to simultaneously acquire six different K-edges in a single exposure, owing to the large energy bandwidth achieved by bending the crystal to a radius of 0.3 m.

Six foils made of palladium, silver, cadmium, indium, antimony, and tin, respectively, were placed in the beam to test the visibility of their K-edges. The K-edges of these six elements, as reported in Table 4.8, are all contained within an energy range of approximately 6 keV. The resulting image is shown in Figure 4.25.

The strong curvature of the crystal enabled an energy bandwidth of approximately 7.2 keV. This represents the first recorded X-ray image demonstrating the simultaneous detection of six K-edges. The visible imperfections in the image are attributed to impurities inside

the foils.

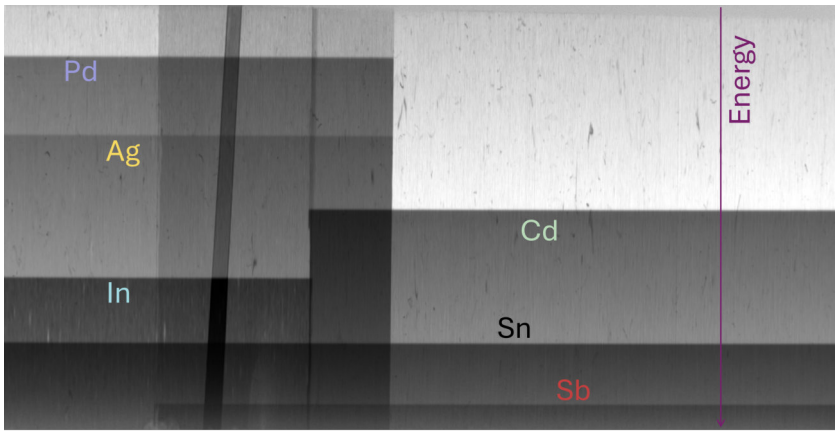

FIGURE 4.25: X-ray image of six foils made of palladium, silver, cadmium, indium, antimony, and tin. All their K-edges are visible in an energy bandwidth of 7.2 keV.

TABLE 4.8: Elements used in the revolvers and their K-edge energies.

Element	K-edge (keV)
Pd	24.4
Ag	25.5
Cd	26.7
In	27.9
Sn	29.2
Sb	30.5
I	33.2
Xe	34.6
Ba	37.4

After confirming the visibility of multiple K-edges, two plastic cylinders, each containing different elements, were prepared and imaged. Both cylinders were made of plastic and had six drilled cavities designed to contain the contrast agents.

In the first cylinder, hereafter referred to as cylinder 1, the cavities were filled with water, palladium, silver, cadmium, indium, and antimony. The second cylinder, referred to as cylinder 2, contained water, two iodine solutions at different concentrations, two barium solutions at different concentrations, and xenon. All solutions were prepared by dissolving the corresponding element salts in water to obtain the desired concentrations. Xenon, being in gaseous form, was injected into the cavity and then carefully sealed to prevent leakage. The specific concentrations, used for both cylinders, are reported in Figure 4.26.

The crystal consisted of a 400 µm thick silicon wafer, bent to a radius of 0.3 m. The surface pole was oriented along $\langle 110 \rangle$ and cut at a 2° asymmetry angle relative to the utilized $(\bar{1}11)$ reflection. Using a (111) type reflection instead of a (220) type increases the diffracted

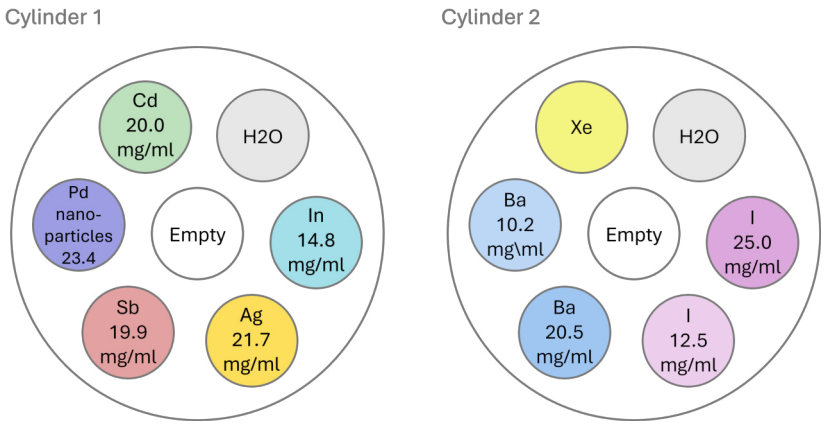

FIGURE 4.26: Schematic of the two cylinders. The concentration of each element is reported inside each circle.

energy bandwidth of a factor of $\sqrt{8/3}$, which is useful when imaging multiple K-edges.

For cylinder 1, the system was tuned to diffract X-rays within the energy range 24 keV to 30 keV, corresponding to a total bandwidth of approximately 7.2 keV. For cylinder 2, the crystal inclination was adjusted to diffract X-rays between 31 keV and 38.5 keV. In both cases, the sample to detector distance was fixed at 32 cm.

The acquisition was carried out using the ORCA-Lightning X-ray sCMOS Camera from Hamamatsu Photonics. This detector features 5.5 µm pixels on a total sensitive area of 4608 × 2592 pixels. Both revolvers were acquired in tomographic mode, with a total of 1800 projections over 180° and an exposure time of 0.32 s per projection. The images were acquired in spectral mode, meaning that the beam tracking mask was not employed, as the primary goal of this acquisition was to quantify the density of the elements.

The obtained projections were dark subtracted and flat fielded prior to reconstruction. The slices were reconstructed using a standard filter back-projection with the Shepp-Logan filter. Material decomposition was then carried out using the SKES algorithm, using water, palladium, silver, cadmium, indium, and antimony as base materials for cylinder 1, and water, iodine, xenon, and barium as base materials for cylinder 2.

Following decomposition, the concentrations within each cavity were measured by selecting a small circular ROI and repositioning it five times within the cavity. The reported density value corresponds to the mean of these measurements, while the associated uncertainty is given by the standard deviation.

The corresponding density maps and quantification results for Cylinder 1 are presented in Figure 4.27 and Table 4.9, respectively.

The results indicate a good discrimination of all elements, with the exception of antimony. During the acquisition, it was observed that the antimony salt used for preparation had poor solubility in

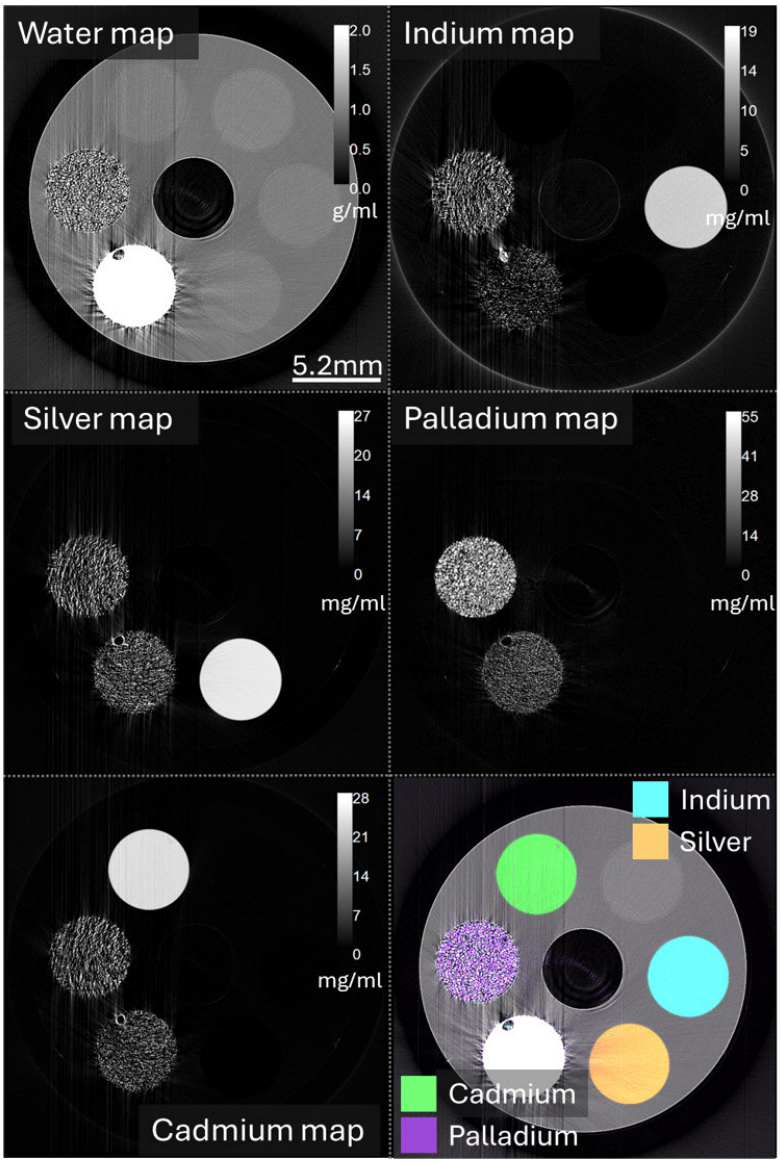

FIGURE 4.27: Density maps for cylinder 1, resulting from the SKES material decomposition algorithm. A composite image of all elements overlaid on the water map is shown in the bottom right.

TABLE 4.9: Expected and measured densities inside cylinder 1.

	Expected	**Measured**
Palladium (mg/mL)	23.4	25.35 ± 0.83
Cadmium (mg/mL)	20.0	23.04 ± 0.11
Indium (mg/mL)	14.8	14.50 ± 0.12
Silver (mg/mL)	21.7	23.26 ± 0.23
Water (g/mL)	1.0	0.982 ± 0.005

water, leading to partial precipitation and deposition inside the cavity. Since the density estimate would have been inaccurate, antimony was excluded from the material decomposition. The high absorption observed in the antimony cavity is therefore attributed to the imaging

of the deposited material.

In the water density map, the contrast window was adjusted so that the antimony cavity appears saturated: this was done solely for visualization, to enhance the visibility of the surrounding image. Nevertheless, the decomposition of the other elements yielded good quantitative results. The measured densities for palladium, cadmium, indium, silver, and water have relative errors of 8.3 %, 15.2 %, 2.0 %, 7.2 %, and 1.8 %, respectively. The higher error observed for cadmium is most likely due to errors in the preparation of the solution. The palladium appears granulated in the image because it was present as nanoparticles suspended in an aqueous medium. Some residual artifacts in the palladium and antimony cavities are visible across all decomposition maps, yielding false-positive signals; these are attributed to the granular nature of both elements. These artifacts do not indicate inaccuracies in the decomposition algorithm, but rather result from the multiple element–water interfaces created by the particulate structure of the materials, reflecting sample morphology rather than limitations of the algorithm.

A similar analysis was performed for cylinder 2, whose decomposed density maps are shown in Figure 4.28, and the quantitative results are presented in Table 4.10.

TABLE 4.10: Expected and measured densities inside cylinder 2.

	Expected	**Measured**
Iodine (mg/mL)	25.0	24.67 ± 0.13
	12.5	12.38 ± 0.07
Barium (mg/mL)	20.5	20.88 ± 0.18
	10.3	10.28 ± 0.26
Xenon (mg/mL)	-	1.85 ± 0.01
Water (g/mL)	1.0	0.996 ± 0.170

The results indicate a successful discrimination among the three contrast elements, with negligible crosstalk between the individual material maps. The measured densities are in good agreement with the expected values, confirming the robustness of the decomposition process. Relative errors of 1.3 %, 1.0 %, 1.8 %, 0.2 %, and 0.4 % were measured for the two iodine concentrations, the two barium concentrations, and water, respectively, indicating very good quantitative accuracy.

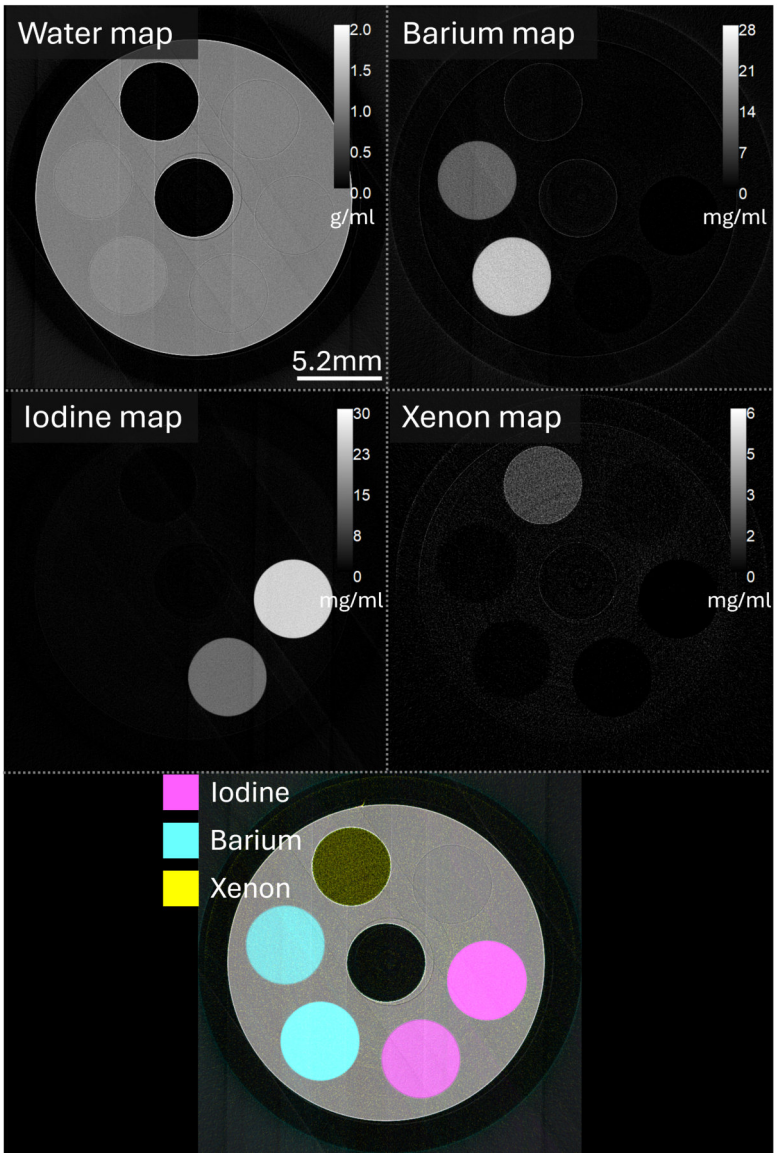

FIGURE 4.28: Density maps for cylinder 2, resulting from the SKES material decomposition algorithm. A composite image of all elements overlaid on the water map is shown in the bottom.

Multiple K-edge murine Sample

The final example of acquisition performed with this multi-modal setup is a planar radiography and a tomography of a murine sample. The goal of this experiment was to demonstrate that multiple elements can be simultaneously identified within a biological sample using the developed imaging approach.

A murine model was prepared with inflatable lungs to enable the introduction of contrast agents, and all procedures were approved by the Ethics Committee of the University of Göttingen. Because the direct injection of iodine and barium into the animal was technically challenging, two plastic tubes filled with iodine solutions and two tubes filled with barium solutions were positioned alongside the

specimen. The iodine tubes contained concentrations of 10 mg mL^{-1} and 5 mg mL^{-1}, while the barium tubes contained 60 mg mL^{-1} and 15 mg mL^{-1} respectively. These concentrations were selected to match the typical range of iodinated contrast agents administered to patients, which is approximately 15 mg mL^{-1} to 30 mg mL^{-1} [Lusic and Grinstaff 2013]. Immediately before acquisition, the sample's lungs were inflated with xenon gas, and the inflation tube was sealed to prevent leakage. A schematic of this sample is shown in Figure 4.29.

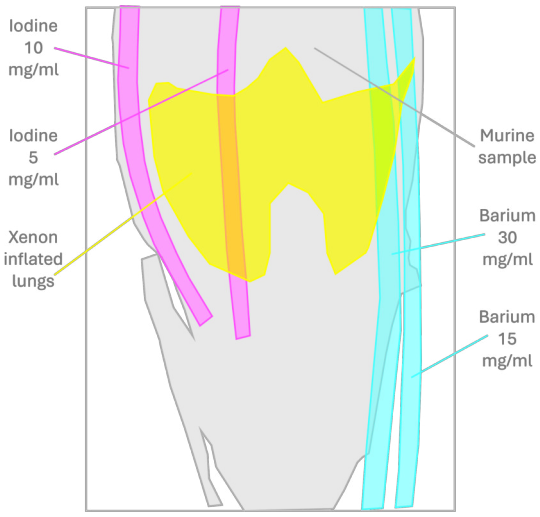

FIGURE 4.29: Schematic of the murine sample prepared for multimodal planar imaging.

The diffracting crystal and the detector used for this acquisition were the same as those described in the previous section. The crystal was tuned to diffract X-rays within the 31 keV to 38.5 keV range, allowing effective imaging of iodine, xenon, and barium K-edges.

The murine sample was first imaged in radiographic mode. Since, with this kind of setup, each exposure corresponds to a single "line" of the sample at multiple energies, a vertical scan was required to acquire the full image. The scan was performed in 800 vertical steps of 50 µm each, covering a total sample height of 4 cm. Moreover, since the sample exceeded the detector's horizontal field of view, two steps in the horizontal direction were performed to cover the entire width of the sample.

Two acquisitions were performed in radiographic mode: one spectral-only (without the beam tracking mask) and one spectral phase-contrast using the whole setup. The mask used for the spectral phase-contrast acquisition featured a 70 µm pitch, and 10 µm aperture, making 7 dithering steps necessary to image the whole sample.

For both acquisitions, the raw projections were initially preprocessed applying dark subtraction and flat fielding. Then, the spectral phase-contrast dataset was processed using the beam tracking al-

gorithm, yielding three radiographic images at multiple energies: absorption, refraction, and dark-field.

Material decomposition was then carried out on both datasets using the SKES algorithm, with water, iodine, xenon, and barium defined as base materials. The resulting decomposed projected density maps for the spectral dataset are shown in Figure 4.30, while the projected density maps for the spectral phase-contrast acquisition are presented in Figure 4.31.

Both the spectral-only and the spectral phase-contrast datasets successfully discriminated the three contrast elements. Since the acquisitions were performed in radiographic mode, the maps correspond to projected density, i.e. density multiplied by thickness.

In the spectral phase-contrast results, a strong dark field signal can be observed within the lungs of the murine model. This is expected, as the dark-field signal is strictly linked to the presence of numerous micro-structures inside the sample. The measurement of dark-field in lungs is an active area of research and is particularly promising, as it provides structural information on the micrometer scale that is typically inaccessible with conventional medical X-ray systems [Bech et al. 2013; Willer et al. 2018]. The lungs exhibit a strong signal because they are composed of many alveoli, which create a large number of air-tissue interfaces responsible for multiple scattering phenomena.

Although the dark-field signal and the xenon map may appear similar, since xenon fills the lungs, the dark-field signal can also originate from other structures within the sample. Some features visible in the dark-field image but absent in the xenon map can be observed; in particular, certain bones generate a noticeable dark-field signal.

In both acquisitions, some edge artifacts can be seen in the iodine map, probably due to a slight distortion of the sample at different energies. As discussed in the introduction to SKES, the converging and diverging geometry of the beam causes photons of different energies to pass through the sample at slightly different angles. In this experiment, the effect is especially pronounced because the sample is spatially extended and the crystal was strongly bent to achieve a wide energy bandwidth for imaging multiple K-edges.

In the spectral phase-contrast setup, transmission, refraction, and dark-field images were retrieved. It is important to note the complementarity between these signals, where different structures of the sample are highlighted. Compared to the spectral-only dataset, the density maps have a lower spatial resolution, which is expected since the horizontal spatial resolution in beam tracking images corresponds to the mask's aperture, which in this case was 10 µm. The horizontal profile plots along the plastic tubes from both barium and

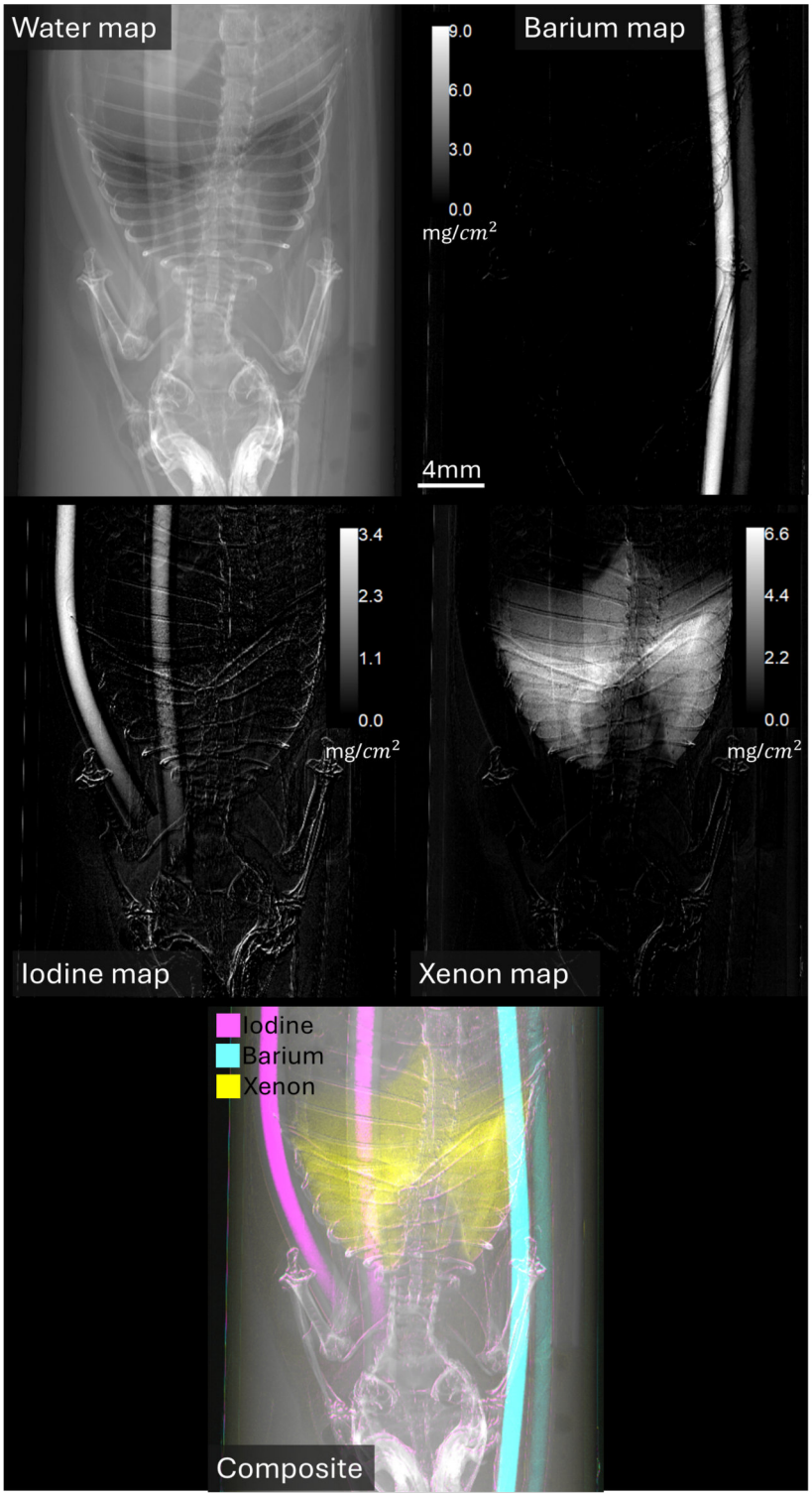

FIGURE 4.30: Decomposition results from the spectral-only dataset. Water, barium, iodine, and xenon maps are shown, along with a composite image with all contributions, where the contrast elements are overlayed on the water projected density map.

iodine projected density maps were computed and compared between spectral-only and the spectral phase-contrast setup. The plots are shown in Figure 4.32.

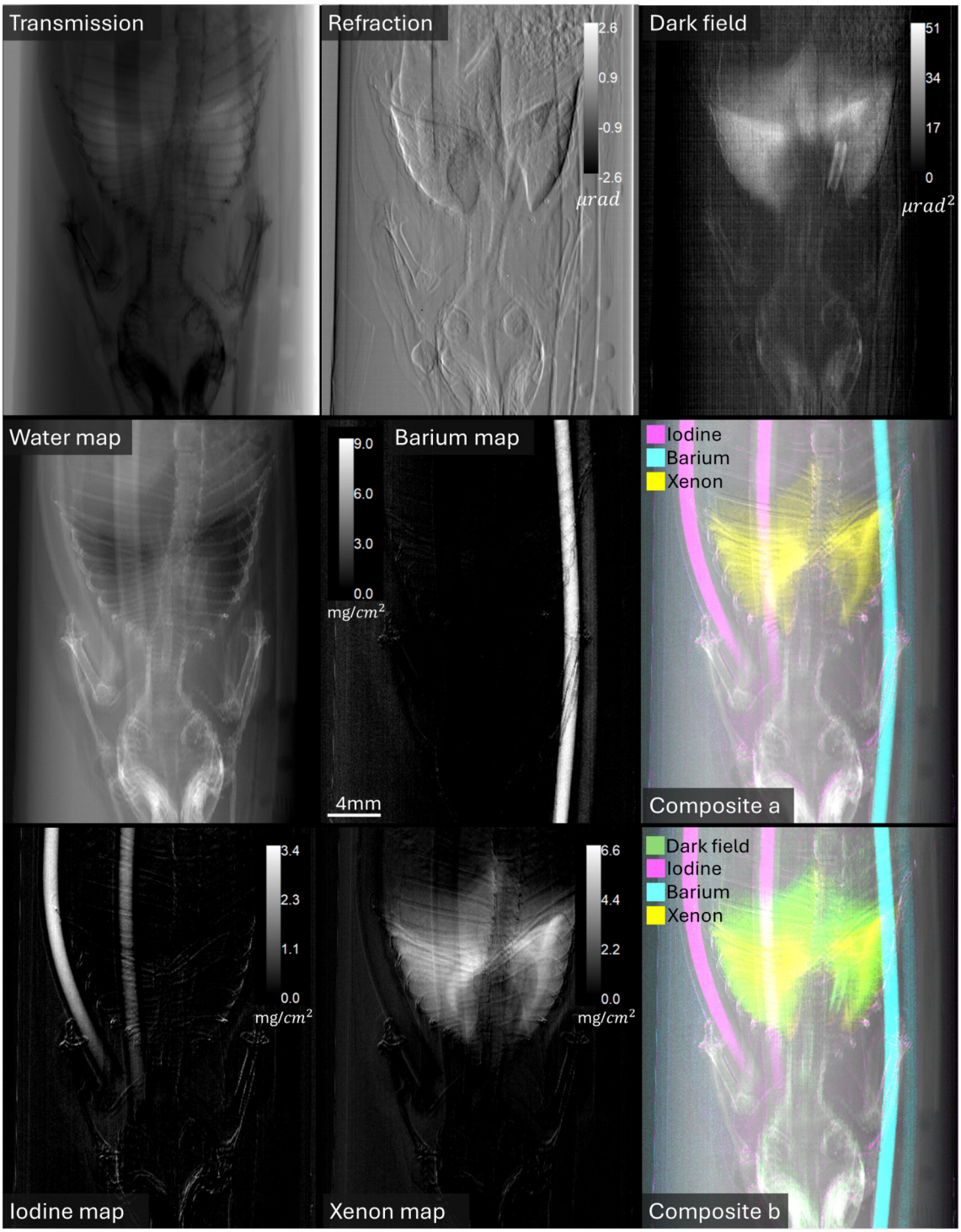

FIGURE 4.31: Decomposition results from the spectral phase-contrast dataset. Top row: transmission, refraction, and dark-field images obtained from the beam tracking algorithm. Bottom rows: water, barium, iodine, and xenon maps, along with a composite image with all contributions, where the contrast elements are overlaid on the water projected density map, and a composite image where the dark-field contribution is also added.

The plots indicate quantitative consistency between the two acquisitions. The spectral phase-contrast has a higher noise compared

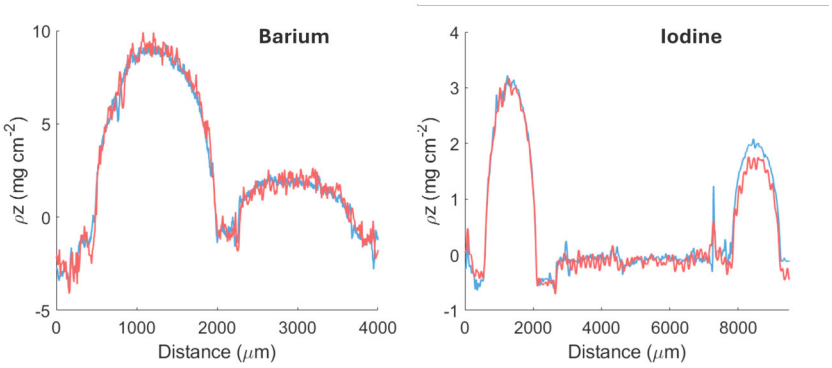

FIGURE 4.32: Horizontal profile plots along the tubes from the barium and iodine projected density maps. The profiles obtained from the spectral-only and the spectral phase-contrast setup are compared.

to the spectral-only setup, due to the lower spatial resolution and to the fact that the absorption images in the spectral-phase contrast setup are a result of a retrieval algorithm, thus are more subject to artifacts or noise amplification.

As anticipated, a tomographic scan of the same sample was also performed. In this case, a single slice of the murine sample was imaged using 1200 projections over 180°. The mask and image processing procedures were identical to those employed for the radiographic acquisition: however, since this dataset was tomographic, the projections were reconstructed using filtered back projection before performing the material decomposition. The decomposition was then applied to the reconstructed tomographic slices, yielding images that represent true volumetric density rather than projected density. Again, both a spectral-only and a spectral phase-contrast acquisition were performed. In the latter case, a spectral phase-contrast decomposition was carried out, including the phase image in the decomposition process.

The results from the spectral-only acquisition are presented in Figure 4.33.

Imaging results show an accurate discrimination of iodine, xenon, barium, and water. The iodine map shows some edge-residual artifacts, that are probably caused by the slices at different energies not being exactly the same spatially. In the xenon map, the xenon probably slightly leaked from the lungs (see brighter areas).

The quantitative measurements, reported in Table 4.11, indicate good quantitative accuracy for all elements, with relative errors being 2.1 %, 17.0 %, 6.3 %, 4.9 %, for the two iodine concentrations and the two barium dilutions respectively.

The resulting decomposed density maps and phase-contrast contributions are shown in Figure 4.34. Quantitative measurements are reported in Table 4.12.

The beam tracking dataset allowed the retrieval of absorption, refraction (differential phase), and dark-field images. Again, as men-

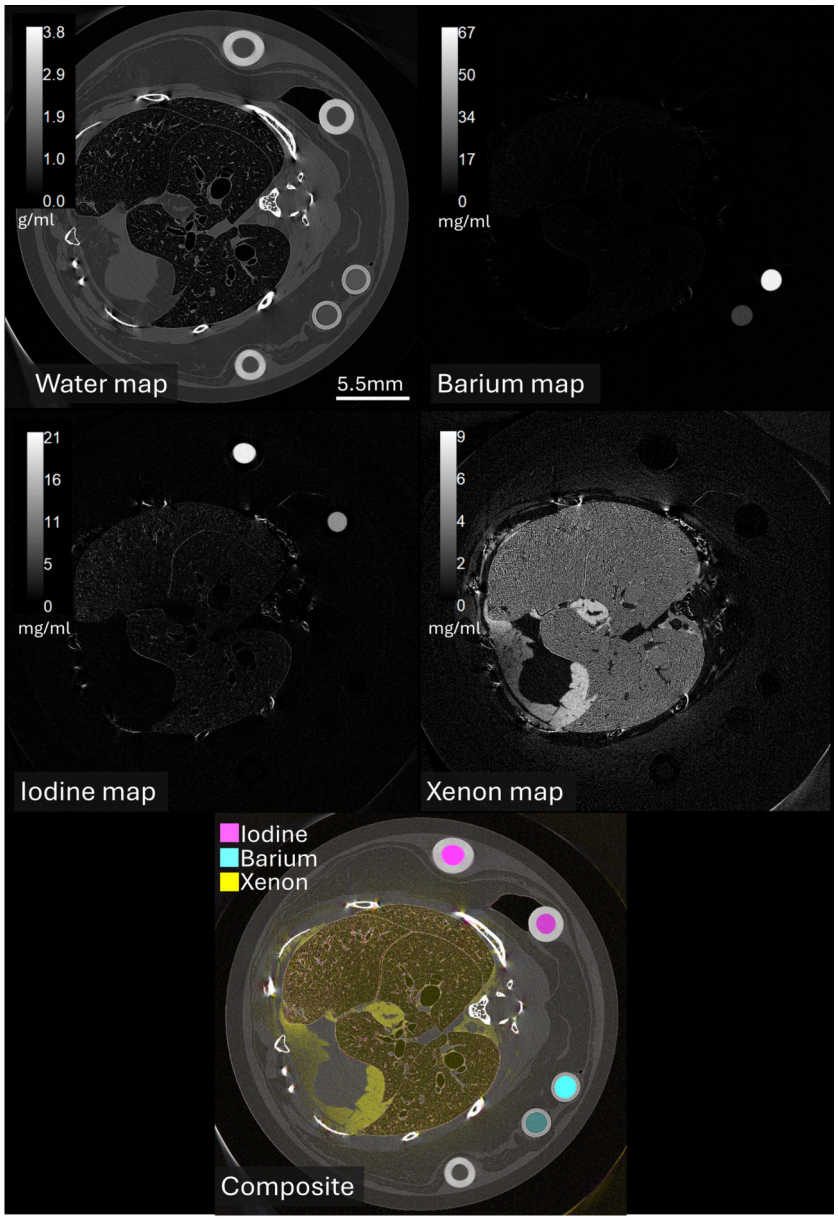

FIGURE 4.33: Decomposition results from the spectral-only dataset. Water, barium, iodine, and xenon maps are shown, along with a composite image with all contributions, where the contrast elements are overlaid on the water density map.

TABLE 4.11: Expected and measured densities in the plastic tubes for iodine and barium, and in the lungs for xenon.

	Expected	**Measured**
Iodine (mg/mL)	20.0	19.59 ± 0.11
	10.0	11.71 ± 0.07
Barium (mg/mL)	60.0	63.79 ± 0.22
	15.0	15.73 ± 0.26
Xenon (mg/mL)	-	2.86 ± 0.14

tioned for the radiographic results, the dark-field map, a strong signal from the lungs can be noted.

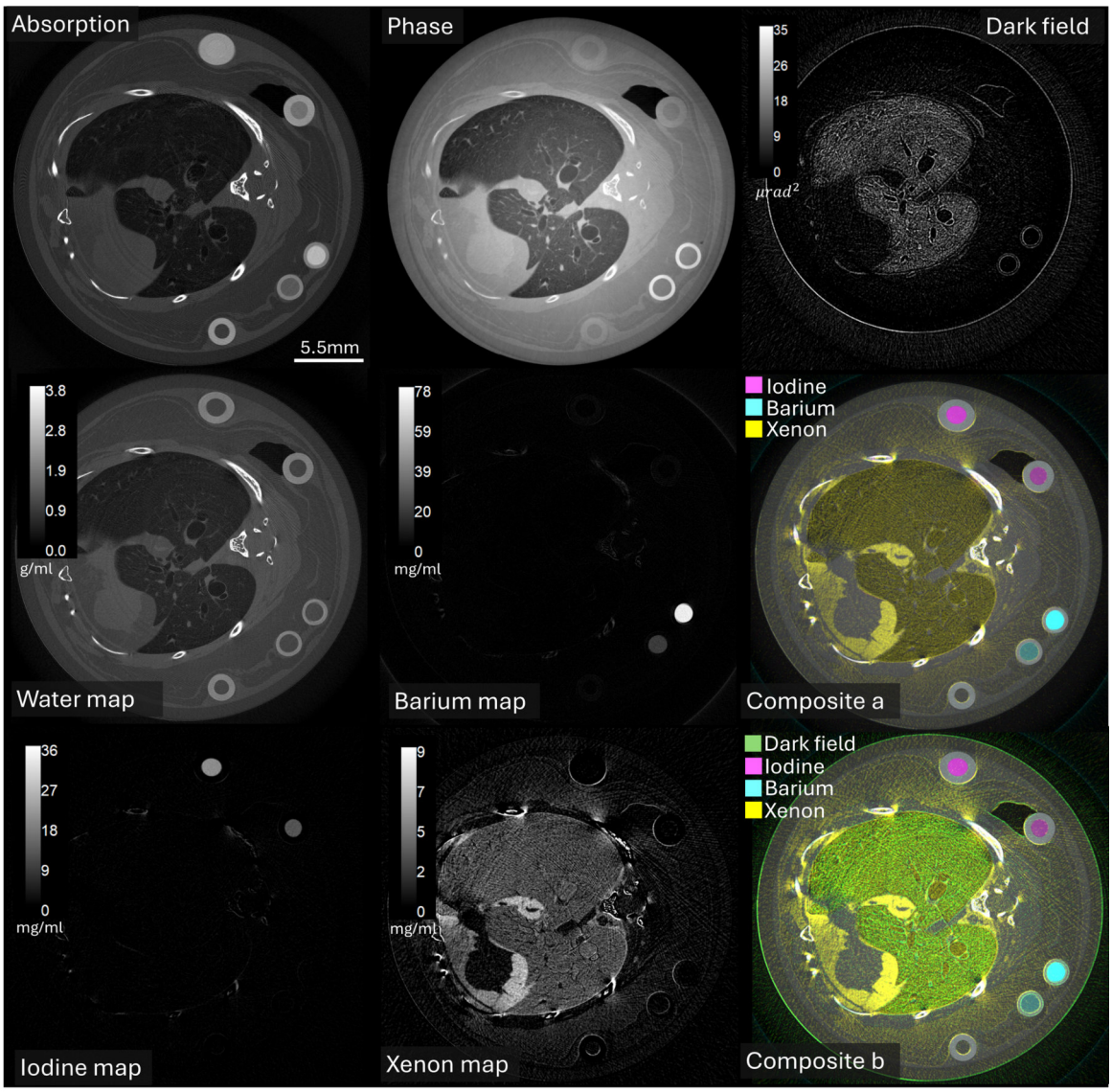

FIGURE 4.34: Decomposition results from the spectral phase-contrast dataset. Top row: absorption, refraction, and dark-field images obtained from the beam tracking algorithm. Bottom rows: water, barium, iodine, and xenon maps, along with a composite image with all contributions, where the contrast elements are overlaid on the water density map, and a composite image where the dark-field contribution is also added.

TABLE 4.12: Expected and measured densities in the plastic tubes for iodine and barium, and in the lungs for xenon.

	Expected	**Measured**
Iodine (mg/mL)	20.0	19.85 ± 0.18
	10.0	11.88 ± 0.21
Barium (mg/mL)	60.0	72.92 ± 0.34
	15.0	18.07 ± 0.16
Xenon (mg/mL)	-	2.41 ± 0.14

Iodine, xenon, and barium were successfully discriminated through a spectral phase-contrast material decomposition. The quantitative

measurements reveal good accuracy for all elements, with relative errors being 0.8 %, 18.8 %, 21.5 %, 20.5 % for the two iodine concentrations and the two barium dilutions, respectively. The quantification of iodine and barium was consistent with the results obtained from the spectral-only acquisition, although the errors were slightly higher due to the lower spatial resolution. However, the barium concentration is overestimated, which is likely due to inconsistencies in the phase image, which may have affected the decomposition accuracy.

As observed in the planar image of this sample, some edge artifacts are present in the iodine map, most likely caused by distortions resulting from the convergent geometry of the X-ray beam as it reaches the sample, which are especially pronounced because of the strong bending of the crystal in this acquisition.

Overall, the results obtained during the different beamtimes using *Setup A* show that the spectral phase-contrast imaging setup was successfully implemented and performed. The imaging system proved to be capable of simultaneously retrieving absorption, refraction, and dark-field signals while maintaining good quantitative accuracy in material decomposition across a wide range of elements and concentrations. The ability to resolve multiple K-edges within a single acquisition and to accurately discriminate different contrast agents in both test and biological samples confirms its robustness. These findings validate the potential of this spectral phase-contrast imaging tool for quantitative and structural analysis, paving the way toward its application in more complex imaging scenarios.

4.2.7 *Setup B*

This section introduces an alternative to *Setup A*, which was developed and implemented as part of this work. The corresponding results have been accepted for publication in [Perion et al. 2025b].

This work presents a multimodal dual-detector imaging setup that integrates beam tracking phase-contrast imaging and crystal-based spectral imaging.

Differently from *Setup A* described in the previous sections, this configuration achieves spectral and phase-contrast imaging on two branches, each with a dedicated detector, rather than combining both techniques on the same branch using a single detector. In this setup, X-ray phase-contrast imaging (XPCI) was performed using the beam tracking technique by introducing an absorbing mask into the beamline's standard polychromatic-beam configuration, which involves a lens-coupled detector used at 10 μm pixel size. X-ray spectral imaging (XSI) was achieved by inserting a Laue crystal in the beam to diffract X-rays around a selected energy, and detecting them with a photon-counting detector with a 60 μm pixel pitch.

Notably, the spectral setup remains fully compatible with the standard polychromatic-beam configuration.

The system was tested on a heterogeneous phantom containing silver dilutions, chalk, a toothpick, plastic microspheres, and nylon wires, as well as on a biological specimen consisting of an osteochondral sample loaded with a cationic iodinated contrast agent. A dedicated processing pipeline was developed to integrate the data from both imaging branches. The combined use of phase-contrast and spectral X-ray imaging provided absorption, phase, and dark-field images. Spectral absorption images, processed via a material decomposition algorithm, yielded quantitative maps of the contrast agent, calcium, and water. The results demonstrate the system's ability to deliver complementary morphological and compositional information with high spatial resolution and quantitative accuracy. This configuration enables quantitative, multimodal 3D imaging, providing information on absorption, phase, dark field, as well as localization and quantification of contrast agents.

Experimental Setup

A schematic and a photograph of the setup are shown in Figure 4.35. In its standard configuration, the beamline includes a sample stage and a lens-coupled detector with tunable pixel size. The sample stage consisted of a six-degree-of-freedom hexapod, a rotation stage, and two linear translation stages. The detector was a Hamamatsu Orca Flash 4.0 (model C11440-22C) with a a 6.5 µm pixel size and a sensitive area of 2048 × 2048 pixels, coupled with an optical magnification system which allows pixel size tuning [Longo et al. 2024]. For the experiment, this configuration was used for XPCI, setting the detector to a pixel size of 10 µm, resulting in a 20.5 mm × 20.5 mm field of view. This detector is particularly well suited for the phase-contrast beam tracking technique, which requires a small pixel size to accurately sample the beamlet profiles.

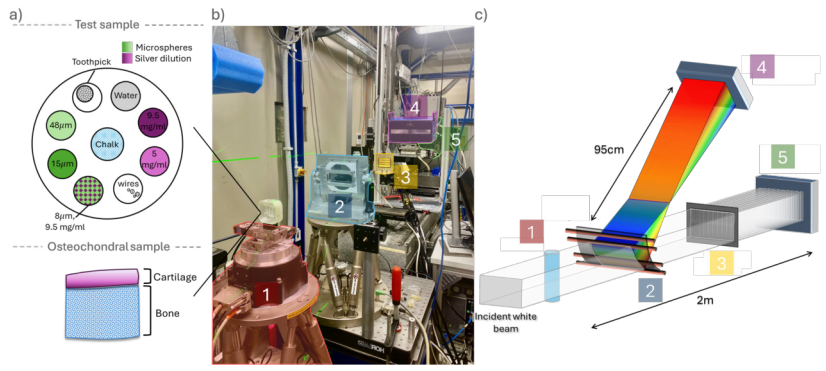

FIGURE 4.35: Photograph (b) and schematic (c) of the experimental setup. The main components are labeled as follows: (1) sample stage, (2) crystal on bender, (3) absorbing mask, (4) photon-counting detector, and (5) polychromatic-beam detector. Panel (a) displays the two samples used in the experiment.

A custom absorbing mask with a gold thickness of 250 µm was used for XPCI. The mask employed for this experiment featured 10 µm wide apertures with a 110 µm pitch. It was placed downstream of the XSI crystal, and 11 dithering steps of the mask were performed horizontally to image the entire sample. The sample to polychromatic-beam detector distance was 2 m.

Note that in this configuration, the absorbing mask is necessarily positioned downstream of the sample, as imposed by the two-branch system. While this geometry is compatible with the beam tracking technique, it is a non-ideal condition, since photons undergoing large refraction angles may be intercepted by the mask septa, effectively acting as a low-pass filter in the angular domain and reducing sensitivity to high refraction angles, with potential implications for dark-field quantitativeness. For the present experiment, however, strict quantitativeness of the dark-field signal was not required, as it was sufficient to achieve differentiation of microspheres with distinct sizes.

A Laue crystal-based XSI system was integrated into the setup. The crystal was a 300 µm thick silicon wafer (Siltronic), bent to a radius of 0.5 m using the aforementioned custom two-bar bender and mounted on a second PI hexapod. The surface pole was oriented along $\langle 110 \rangle$ and cut at a 2.5° asymmetry angle relative to the utilized $(\bar{2}20)$ reflection. The hexapod allowed to tilt the crystal to a chosen Bragg angle, and thus select the corresponding diffracted energy interval. In this work, the system was tuned to diffract X-rays around the K-edge of silver (25.5 keV) for the first sample, and iodine (33.2 keV) for the second, with an experimentally measured relative energy resolution $\Delta E/E$ of around 10^{-3}.

The diffracted beam was collected using the PIXIRAD-8 CdTe photon-counting detector [Bellazzini et al. 2013; Delogu et al. 2016], which features a 650 µm thick CdTe sensor with hexagonally arranged pixels at a 60 µm pitch over a 246 mm × 24.8 mm total active area. The detector was positioned 95 cm downstream of the crystal along the diffracted beam path and mounted on a manually adjustable tilt platform to be perpendicular to the beam. Unlike the sCMOS detector, the photon-counting detector registers individual X-ray photons, providing a high signal-to-noise ratio. This makes it ideal for noise-sensitive applications such as spectral basis material decomposition.

In summary, the entire experimental setup combined the XPCI and XSI branches as follows: the polychromatic beam first passes through the sample and then impinges on the crystal. Most of the beam is transmitted through the crystal, passes through the beam tracking absorbing mask, and is recorded by the polychromatic beam detector for XPCI. In parallel, a small fraction of photons within a selected energy interval is diffracted by the crystal at twice the Bragg angle and collected by the photon-counting detector (see Figure 4.35,

right panel).

Samples and Image Acquisition

The scanned samples included a test sample and a biological sample. The test sample was a 16 mm plastic cylinder with nine cylindrical cavities filled with the following materials: two silver dilutions (9.5 mg mL^{-1} and 5 mg mL^{-1}), nylon wires, a mixture of 8 µm polymethyl methacrylate (PMMA) microspheres and 9.5 mg mL^{-1} silver dilution, 15 µm PMMA microspheres, 48 µm PMMA microspheres, a wooden toothpick, and chalk mainly composed of $CaCO_3$ (see Figure 4.35). The silver dilutions were prepared by mixing water and silver salt $AgNO_3$ in different concentrations. This sample was specifically designed to produce measurable signals across all relevant channels: dark field (microspheres), absorption (for contrast element quantification), and phase, allowing for an evaluation of the imaging technique performance.

The biological sample was a cylindrical osteochondral plug extracted from a bovine stifle joint with a diameter of 10 mm and loaded with $CA4^+$ (10 mg cm^{-3} iodine). The sample was kept in the $CA4^+$ bath prior to imaging. $CA4^+$ is a positively-charged iodinated contrast agent with affinity for negatively charged proteoglycans in cartilage [Stewart et al. 2017]. It has been developed to improve cartilage visualization due to its short diffusion time, low required concentration, and direct correlation with the proteoglycan distribution [Fantoni et al. 2024].

Both samples were scanned in tomographic mode using continuous rotation, with 1200 projections acquired over 180°. The exposure time per projection was set to 100 ms, resulting in an acquisition time of 120 s per scan for each dithering step of the absorbing mask. While 11 dithering steps were required for the XPCI setup, only one acquisition was used for the XSI dataset.

Image processing pipeline

The image processing pipeline, which will be described in the following paragraphs, is depicted in Figure 4.36.

For the XPCI acquisition, the beam tracking projections were processed individually using a custom MATLAB script to extract absorption, refraction (differential phase) and dark-field (ultra-small-angle scattering) signals. Specifically, each beamlet was analyzed on a row-per-row basis and modeled as a Gaussian profile, from which the statistical moments were derived: 0th for absorption (intensity), 1st for refraction (spatial shift), and 2nd for dark field (broadening) [Vittoria et al. 2015b]. The refraction projections were then integrated through a Wiener-filter regularized phase integration algorithm to produce

integral phase projections [Massimi et al. 2020]. All resulting projections were reconstructed using standard filter back projection with Shepp-Logan filter, obtaining three tomographic volumes (absorption, phase, and dark field). Given that the mask aperture matched the detector pixel size, the final voxel size in the reconstructed volumes was 10 µm × 10 µm × 10 µm.

Regarding the XSI acquisition, as mentioned earlier, the beam diffracted by the crystal is energetically dispersed in the diffraction plane. As a result, energies are spatially separated along the vertical axis of the detector. Since the sample was placed before the crystal, each row of a projection simultaneously encodes information from a different vertical portion of the sample and from a different energy, making the vertical axis of each projection a convolution of spatial and spectral information. The K-edge energy was positioned approximately at the center of the detector's vertical field of view for each acquisition.

Due to the limited vertical size of the laminar synchrotron beam (approximately 4 mm), multiple vertical scans of the sample were required, which are indicated as $z_1, z_2, \ldots z_n$ in Figure 4.36. This enabled each region of the sample to be imaged at energies both above and below the K-edge of the target element for the XSI dataset.

After acquisition, a detector-specific pre-processing procedure, including flat-field normalization, was applied to the projection images [Brombal et al. 2018]. Each image was then cropped into two energy ranges: the upper half corresponded to energies above the K-edge, and the lower half to energies below it. Since multiple vertical were performed, the overlapping regions (both above and below the K-edge) were stitched together to generate complete tomographic datasets for each energy condition.

Both the above-edge and below-edge stitched projection sets were reconstructed using standard filter back projection with the Shepp-Logan filter. Taking into account the vertical magnification of the diffracted beam, the effective voxel size of the spectral datasets was 17 µm × 60 µm × 60 µm.

In order to match the XSI and XPCI datasets, the two had to be co-registered. To achieve this, a slice from the XPCI dataset was downsampled to match the spatial resolution of corresponding XSI slice. The registration transformation aligning the XSI slice to the XPCI reference was determined using ImageJ's *Rigid Transformation* registration plugin [Schneider et al. 2012]. A rigid transformation was chosen since only minor shifts or rotations were expected between the datasets, making this approach sufficient to achieve accurate alignment. The resulting transformation matrix was then applied uniformly to all slices of the XSI dataset using Matlab's *imwarp* function.

Finally, the above and below K-edge images, together with the

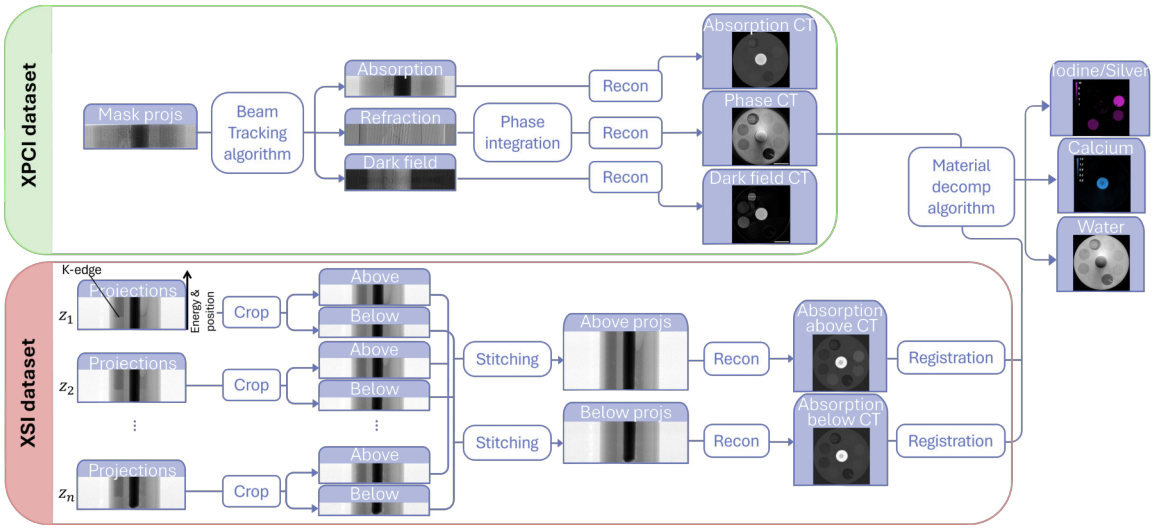

FIGURE 4.36: Image processing pipeline.

phase image, were used as inputs to the material decomposition algorithm, following the same formulation introduced in [Brombal et al. 2024]. The decomposition employed silver, calcium, and water as the basis materials for the first sample, and iodine, calcium, and water for the second. Notably, the inclusion of the phase image enabled the use of an additional basis material in the decomposition process (i.e. calcium).

Following decomposition, quantitative analysis was performed on the resulting density maps of the test sample. Circular regions-of-interest (ROIs) were selected inside the cylindrical holes, and the mean intensity across five slices was measured to estimate material concentration. The uncertainty in the measured density was defined as the standard error of the five intensity values.

Results

The XPCI polychromatic-beam setup enabled the simultaneous extraction of absorption, phase, and dark-field images, which are presented in the top row of Figure 4.37.

The complementarity between the absorption and phase information should be noted: while the holes filled with water and microspheres are nearly indistinguishable from the plastic support in the absorption image, they are clearly distinguished in the phase image. In fact, the contrast-to-noise ratio (CNR) of the water-filled hole increases from 0.006 in absorption to 4.3 in phase.

The halo artifacts visible in the phase image are common in such reconstructions and likely originate from the strong absorption of the chalk, which locally reduces beamlet intensity and weakens the algorithm's robustness. During integration, outlier pixels caused by these local instabilities can accumulate and lead to the appearance

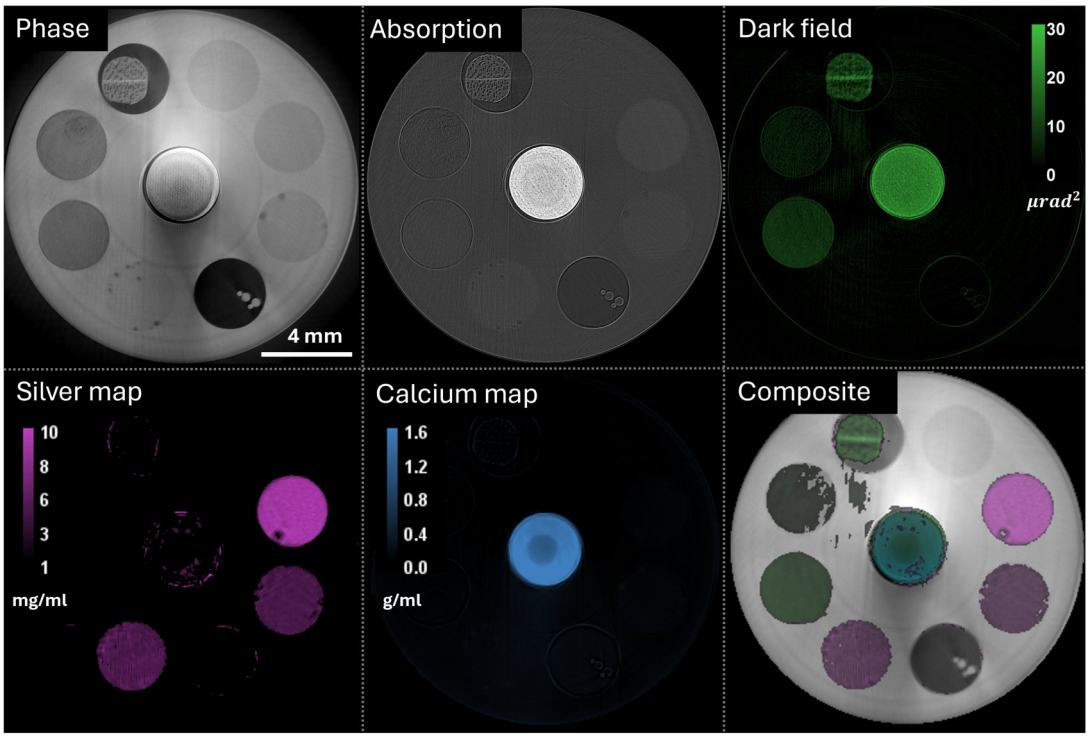

FIGURE 4.37: Test sample results. Top row: phase, absorption and dark field images obtained from the XPCI dataset. Bottom row: silver and calcium density maps, composite image of water, silver, calcium and dark-field.

of halo artifacts. Another possible cause may be the distortion of the sample due to the convergent geometry of the diffracted X-ray beam. As seen in the absorption image, the circles do not close perfectly, and similar distortions occur in the refraction signal; when integrated to recover phase, these inconsistencies can further contribute to the appearance of halo artifacts.

The dark field image differentiates the two holes containing microspheres, with the smaller microspheres generating a stronger scattering signal, as expected. In addition, both the toothpick and the chalk produce a strong dark-field signal. In contrast, the hole filled with a mixture of microspheres, silver and water did not produce any detectable signal, likely due to the similar refractive indices of water and PMMA, which suppresses dark field contrast.

The material decomposition algorithm produced the quantitative density maps of silver, calcium, and water, the first two being shown in the second row of Figure 4.37. The decomposition effectively discriminates and localizes the individual elements. Specifically, holes containing nominal silver concentrations of 9.46 mg/mL and 4.65 mg/mL were quantified as 9.11(33) mg/mL and 4.51(29) mg/mL, respectively. Both measurements are slightly underestimated relative to the nominal values, with relative differences of 3.6 % and 3.4 % respectively. This small systematic underestimation still indicates a good quantitative accuracy of the system.

It should be noted that the XPCI and XSI datasets were acquired simultaneously, thus all the images presented derive from datasets acquired during the same acquisition sequence.

Figure 4.38 presents the results obtained from the osteochondral biological sample dataset.

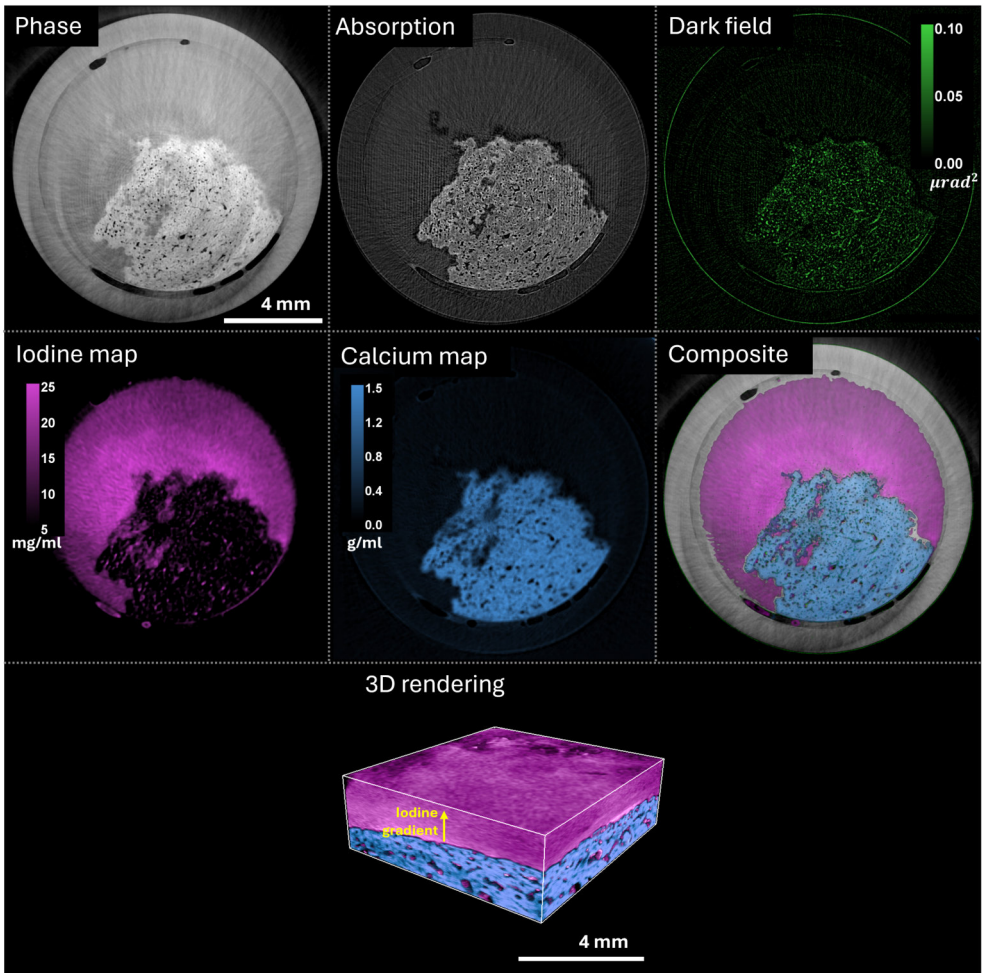

FIGURE 4.38: Osteochondral biological sample results, with all images representing the mean across five slices. Top row: phase, absorption and dark field images obtained from the XPCI dataset. Bottom row: iodine and calcium density maps, composite image of phase, iodine, calcium and dark-field, and 3D rendering of calcium and iodine decompositions.

The top row shows the XPCI results, namely phase, absorption and dark-field images. Given the tissue composition, which is primarily bone and cartilage, phase and absorption yield similar morphological contrast. The dark-field shows peaks of signal corresponding to specific air-bone interfaces within the subchondral bone.

The material decomposition was performed using iodine, calcium, and water as basis materials: the iodine and calcium maps are shown in the bottom row of Figure 4.38. The decomposition effectively separated the iodine-loaded cartilage from the subchondral bone, allowing quantitative discrimination between the two. In the calcium map, the subchondral bone's features are effectively distinguished,

and the measured intensity values are in good agreement with typical bovine bone densities [Fursey 1975]. In the iodine map, an intensity gradient can be observed, decreasing from the deep cartilage, which is rich in proteoglycans, to the superficial layer (see yellow arrow in Figure 4.38, bottom right). This behaviour is consistent with previous published studies [Honkanen et al. 2020; Fantoni et al. 2024].

Conclusions

In conclusion, this work presents a dual-detector system that enables the simultaneous acquisition of high-resolution μCT data, providing both structural and compositional information. Phase, absorption, and dark-field images were obtained using the beam tracking XPCI technique on the standard polychromatic-beam configuration of the beamline, while spectral data were acquired with a crystal-based system coupled with a photon-counting detector. The spectral data were processed through a material decomposition algorithm that incorporates phase information to produce quantitative maps of selected elements or compounds. The ability to localize and quantify specific materials, such as contrast agents, or to resolve specific fine structures within complex samples is of significant relevance and was demonstrated in this work. The presented results highlight the potential of simultaneous XPCI and XSI imaging for multimodal 3D imaging with quantitative accuracy.

Conclusions

This thesis was dedicated to the development and optimization of spectral and phase-contrast X-ray imaging techniques, with the goal of advancing their performance and exploring their applicability. Although the work covered different imaging modalities and setups, all contributions are unified by two main objectives: first, to refine spectral and phase-contrast methods individually; and second, to investigate whether- and how-their combination could lead to a unified imaging approach with enhanced capabilities.

The individual optimization of spectral and phase-contrast techniques was primarily carried out in laboratory settings. On the spectral side, X-ray imaging was explored using energy-resolving photon-counting detectors for dual- and multi-energy micro-CT. These experiments demonstrated the capability to discriminate and quantify multiple contrast agents, specifically iodine and gold, within a sample. Gold nanoparticles are emerging as a CT contrast agent due to their high X-ray absorption, low toxicity, high biocompatibility, and their specificity in targeting tumors. However, their visualization in laboratory settings may be challenging because the high K-edge of gold (80.7 keV) lies beyond the optimal flux range of conventional X-ray sources. Despite this limitation, the results confirmed the effectiveness of spectral imaging for multi-material differentiation and quantitative analysis. More broadly, these experiments highlighted the advantage of combining spectral sensitivity with micro-CT, enabling the simultaneous acquisition of anatomical and compositional information within a single scan.

Further individual optimization was pursued during a six-month research period in Grenoble, where phase-contrast imaging using speckle- and membrane-based techniques was investigated in detail. Through the study of these approaches and the LCS algorithm, an optimized membrane-stepping approach was conceived to improve image quality without increasing experimental complexity. This approach represents just an initial, but promising, step toward more efficient phase-contrast acquisitions which can be further refined in the future, with its potential impact extending beyond laboratory settings to synchrotron facilities. Regarding phase-contrast imaging, the beam tracking retrieval algorithm was refined and tested across a wide range of datasets and detector types, which confirmed its robustness.

Building on these individual developments, efforts were then directed toward the realization of simultaneous spectral and phase-contrast imaging. A first combined experiment was performed at the

synchrotron on human biological samples, with the goal of simultaneously mapping structural and compositional information. In the context of virtual histology, phase-contrast imaging is essential for visualizing soft tissues that would otherwise be poorly visible using conventional attenuation-based methods. At the same time, pathologists seem to show interest in determining both the localization and concentration of iodine inside thyroid tissue. While conventional histology remains the gold standard for tissue pathology due to its accessibility and high biochemical specificity, X-ray virtual histology offers complementary advantages: it can, on one side, produce three-dimensional, non-destructive data and, when combined with spectral techniques, enable elemental quantification within tissues. This combined spectral phase-contrast experiment allowed us to produce both high-resolution virtual histology images and quantitative maps of iodine and calcium content.

The core contribution of this work was the development of a crystal-based beam tracking imaging setup. This required extensive characterization and optimization of the crystal properties, as well as the assessment of their impact on imaging performance. This whole development process led to successful imaging outcomes, first validated on test samples designed to mimic key contributions, i.e. contrast element quantification, scattering and phase, and later successfully applied to biological samples as well. The unification of beam tracking phase-contrast imaging with crystal-based spectral imaging is undeniably complex, and for many applications the required effort may not be advantageous, particularly when similar results can be obtained at synchrotron facilities using simple propagation-based phase-contrast at multiple monochromatic energies. Nevertheless, the use of optical elements for phase-contrast imaging, such as the absorbing masks used in this work, enables access to the dark-field signal, which is of growing interest within the community and cannot be retrieved using propagation-based methods. Similarly, crystal-based spectral imaging is inherently more complex to implement than most alternative spectral techniques, and for many routine applications this additional complexity is not justified. However, the developments presented in this thesis demonstrate that the technique is still worth pursuing, as it offers capabilities that are difficult to achieve with alternative approaches. First, the ability to acquire multiple energies simultaneously makes this approach highly attractive for time-critical or motion-sensitive applications, such as in vivo planar imaging, where sequential energy scans are impractical. Second, the intrinsically high energy resolution of bent crystals, which is in the order of a few tens of electronvolts, enables enhanced sensitivity to low concentrations of contrast agents, opening the door to quantitative imaging in cases where photon-counting detectors, which are

restricted to an energy resolution of 1-2 keV, do not provide sufficient energy resolution. These considerations suggest that crystal-based beam tracking imaging may find valuable applications in niche and specific scenarios and could in the future prove to be well suited for new application domains.

Several results of this thesis have been published in different scientific journals, including *Applied Physics Letters*, *Journal of Physics D: Applied Physics*, *Physics in Medicine & Biology*, and *Journal of instrumentation*.

Overall, this work advanced the individual optimization of spectral and phase-contrast imaging techniques and explored their integration into a unified imaging framework. While the results represent a step forward toward high-resolution, quantitative X-ray imaging with potential applications in biomedical diagnostics and materials science, significant challenges remain. Further methodological development and deeper investigation of suitable applications will be necessary to fully exploit the potential of these techniques and address complex scientific questions.

APPENDIX

A

Crystal bending uniformity measurements

Measurements of the crystal's curvature uniformity were performed at the Optical Metrology Laboratory of Elettra synchrotron. The goal was to measure the effective crystal bending radius and verify its consistency with the bender's nominal value. Moreover, the reproducibility of the crystal mounting was assessed by comparing measurements of the crystal's bending radius performed before and after dismounting and remounting the crystal on the bender. Assessing reproducibility is particularly important since in imaging experiments the same crystal is often mounted on different benders, hence having a reliable curvature is essential for a consistent performance.

The crystal used for this measurement was a 300 µm thick silicon wafer. The surface pole was oriented along [110] and cut at a 2.5 deg angle relative to the utilized $(\bar{2}20)$ reflection. All measurements were performed with the crystal mounted on the bender with a 0.5 m curvature (see Section 4.2.1).

The measurements were initially performed with ZYGO DynaFiz Laser Interferometer to get a qualitative overview of the crystal's curvature. This interferometer uses a frequency-stabilized HeNe laser (632.8 nm) as coherent light source and is typically used to evaluate surface figures (e.g. flatness, sphericity). Unfortunately, measurements with this interferometer did not produce any quantitative value of the radius because a calibration was needed. Nevertheless, owing to the large beam size of the instrument, a fairly wide image of the crystal's curvature was acquired consisting in about 100 mm × 15 mm. The results are shown in Figure A.1.

The results show that the crystal exhibits a reasonably uniform curvature over a length of approximately 40 mm. Although the full crystal width is 100 mm, this level of uniformity is sufficient considering that the field of view of our imaging system is governed by the detector, which has a sensitive area of 30 mm × 16.8 mm check!!!.

Further measurements were performed with ZYGO Nexview 3D

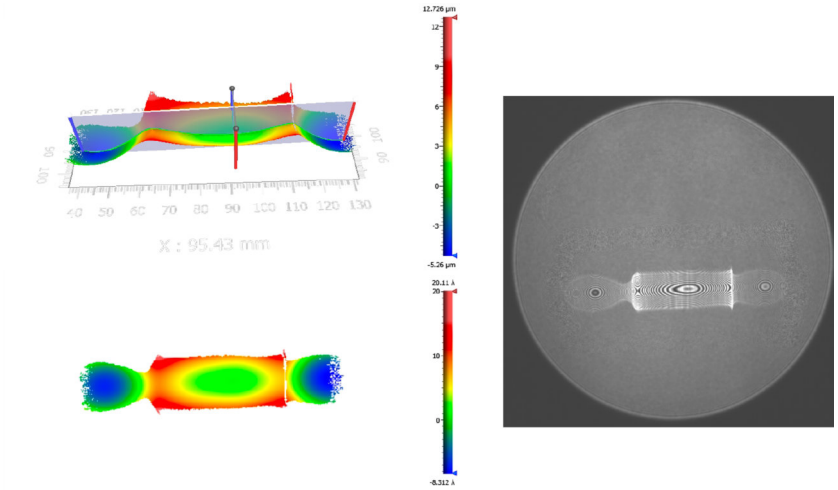

FIGURE A.1: Images of the crystal's curvature obtained from the ZYGO DynaFiz Laser Interferometer. Left: 3D (top) and 2D (bottom) view of the crystal's curvature. The vertical scales are arbitrary as the system was not calibrated. Right: interferometric image of the curvature

Optical Profiler. This instrument, based on coherence scanning interferometry, allowed a precise determination of the bending radius of the crystal both before and after dismounting and remounting it on the bender. The measurements were performed on an area of about 1 mm × 1 mm located near the center of the crystal. Results are shown in Figure A.2.

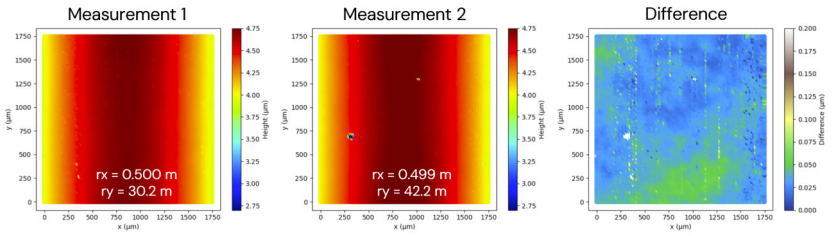

FIGURE A.2: Images of the crystal's curvature obtained from the ZYGO Nexview 3D Optical Profiler. Measurement 1 and Measurement 2 correspond to the scans performed before and after dismounting and remounting the crystal, respectively. On the right, the difference map between Measurement 1 and 2 images is shown.

For Measurement 1, the bending radius was determined to be 0.499 m, in agreement with the nominal value of 0.5 m. A secondary curvature was also detected in the perpendicular direction, with a radius of 42.2 m. This minor curvature does not affect impact imaging performance. After dismounting and remounting the crystal on the same bender, Measurement 2 was performed. The measured radius of 0.500 m confirmed the reproducibility of the bending system. Again, a curvature along the perpendicular direction was observed, this time with a radius of 30.2 m. A difference between the two measurements reveals no significant differences, except for some defects of the crystal. The mean of the difference image is 0.036 µm, ranging from 0.0 µm to 1.9 µm (defects).

B

Simulation

b.1 CONTRIBUTIONS TO ENERGY RESOLUTION

A crystal, even one that satisfies the magic condition (see Section 2.1.6), does not produce perfectly monochromatic X-rays. Instead, the diffracted photons contain a range of energies that determines the energy resolution of the monochromator [Qi et al. 2021].

There are multiple individual contributions to the energy resolution, whose sum gives the ultimate energy resolution of the monochromator.

1. **Lattice d-spacing**: The lattice spacing (d-spacing) inside the crystal is not uniform because of the crystal bending. As a result, photons that are diffracted and exit the crystal at the same point will have an energy spread due to this non-uniformity, described by:

$$\left(\frac{\Delta E}{E}\right)_1 = \frac{T}{R}(\cos^2\chi - \nu\sin^2\chi)$$

where T is the thickness of the crystal, R is its bending radius, χ is the asymmetry angle, and ν is the Poisson ratio.

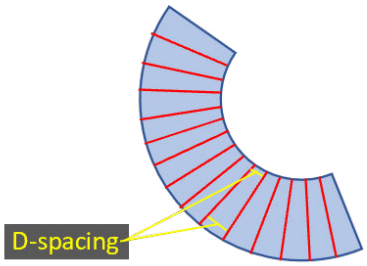

Figure: d-spacing variation due to crystal bending

2. **Finite X-ray source distance**: The X-ray source is not infinitely far away, which causes photons to strike the crystal at slightly different angles. This angular spread contributes to the total energy spread, as given by:

$$\left(\frac{\Delta E}{E}\right)_2 = \frac{T}{p}\frac{\cos^2\theta_B}{\cos(\chi - \theta_B)}$$

where p is the X-ray source to crystal distance, and θ_B is the Bragg angle.

3. **Darwin width**: The Darwin width is an intrinsic property of the crystal and is a fundamental contributor to the energy spread. It is calculated as:

$$\left(\frac{\Delta E}{E}\right)_3 = \frac{w_D}{\tan\theta_B}$$

where the Darwin width w_D is:

$$w_D = 2.12\ \lambda^2\ r_e\ \frac{F}{\pi a^3 \sin(2\theta_B)}$$

with λ being the photon's wavelength, r_e the classical electron radius, F the structure factor of the crystal, and a the lattice parameter.

4. **Source size**: The X-ray source size is never infinitely small, and it contributes to the energy resolution according to the following equation:

$$\left(\frac{\Delta E}{E}\right)_4 = \frac{S}{p\tan\theta_B}$$

where S is the source size.

5. **Lifetime broadening:** This contribution is intrinsic and not linked to the experimental setup (crystal, source, or detector). It arises from the natural width of the transition, even in the absence of any external broadening mechanisms. When an atom is in an excited state, it has a finite lifetime before it decays. According to Heisenberg's uncertainty principle $\Delta E \Delta t \geq \hbar/2$, the finite lifetime leads to an uncertainty in the energy, which results in a natural energy width. This ranges from fractions of electronvolts for light elements to hundreds of electronvolts for heavier ones.

$$\left(\frac{\Delta E}{E}\right)_5$$

6. **Detector spatial resolution**: In addition to the contributions listed above, the detector's spatial resolution can also have a significant impact on the overall energy resolution. The main limitations are the pixel size and the point spread function. In order for the detector not to influence the energy resolution, its spatial resolution should be less than the spatial extension of the energy spread when it reaches the detector. Since the diffracted beam diverges, there will always be a distance where the above condition is matched.

The first two contributions to the energy resolution are directional. Therefore, their combined contribution to the total energy resolution must be considered jointly. Assuming that the source size follows a Gaussian distribution and is uncorrelated with the angular distribution, the third, fourth, and fifth contributions can be added in quadrature. The overall energy resolution can therefore be expressed as follows:

$$\left(\frac{\Delta E}{E}\right) = \sqrt{\left[\left(\frac{\Delta E}{E}\right)_1 + \left(\frac{\Delta E}{E}\right)_2\right]^2 + \left(\frac{\Delta E}{E}\right)_3^2 + \left(\frac{\Delta E}{E}\right)_4^2 + \left(\frac{\Delta E}{E}\right)_5^2}$$

b.2 BENT CRYSTAL MODEL

In the simulation, a model of the bent crystal was implemented to calculate the diffraction angle of an incident photon. The known parameters are: α, the angle of emission of the photon from the source; F_1, the distance from the source to the crystal; θ_B, the Bragg angle; χ, the asymmetry angle; d, the lattice d-spacing; T, the crystal thickness; ν, the Poisson ratio; and R, the bending radius of the crystal.

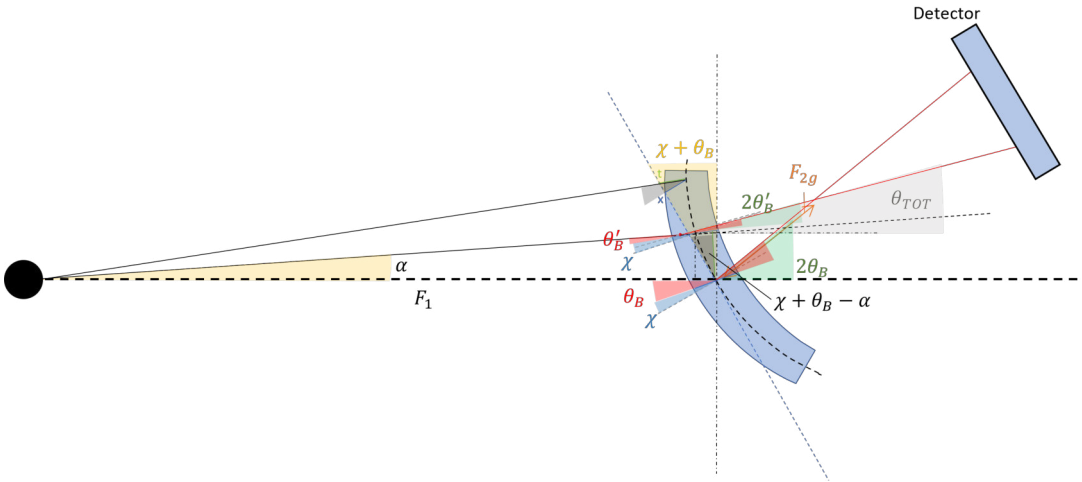

FIGURE B.1: Sketch of the simulation geometry.

The center of the circular arc that describes the crystal curvature is defined as:

$$x_c = R\cos\theta_B \qquad y_c = R\sin\theta_B$$

The intersection of the photon trajectory with the curved crystal is found by solving the quadratic equation $Ax^2 + Bx + C = 0$:

$$x_{crystal} = \frac{-B - \sqrt{B^2 - 4AC}}{2A} \qquad y_{crystal} = \tan\alpha\ (x_{crystal} + F_1)$$

where

- $A = 1 + \tan\alpha^2$
- $B = \tan\alpha\ (\tan\alpha\ 2F_1 - 2y_c) - 2x_c$
- $C = x_c^2 + y_c^2 + (\tan\alpha\ F_1)^2 - 2y_c \tan\alpha\ F_1 - (R - T/\cos\chi)^2$

The angular coefficient of the crystal plane with respect to the horizontal is calculated as m, and the coordinates of center of the plane (where T = 0) are:

$$x_{prov} = x_{crystal} - \frac{T}{\cos\chi}\cos m \qquad y_{prov} = y_{crystal} - \frac{T}{\cos\chi}\sin m$$

If the crystal is bent, the local crystal plane is tilted according to the bending:

$$\gamma = \arctan\left(\frac{\sqrt{x_{prov}^2 + y_{prov}^2}}{R}\right)$$

leading to a corrected Bragg angle θ and total diffraction angle θ_{tot}:

$$\theta = \theta_B - \alpha - sign(y_{prov})\gamma \qquad \theta_{tot} = 2\theta + \alpha;$$

This is the total diffraction angle relative to the horizontal, following the law of reflection. The polychromatic focal distance is then calculated as

$$F_{2p} = \frac{R\sin(2\theta)}{2\sin(\chi+\theta) + \cos(\chi+\theta)\sin(2\chi)(1+\nu)}$$

and the energy of the diffracted photon as:

$$E = \frac{12.398419 \times 10^{-10}}{2d\sin\theta}$$

where $12.398419 \times 10^{-10}$ is hc in eV m.

The final output parameters are $x_{crystal}$ and $y_{crystal}$, the coordinates where the photon hits the crystal; θ_{tot}, the total diffraction angle; E, the energy of the diffracted photon; and F_{2p}, the polychromatic focal distance.

Bibliography

A. Brooks, Rodney and Giovanni Di Chiro (1978).
"Split-detector computed tomography: a preliminary report". In: *Radiology* 126.1, pp. 255–257. (Cit. on p. 20).

Advacam (2025).
MiniPIX TPX3. Accessed: October 24, 2025. (Visited on 10/24/2025) (cit. on p. 97).

Albers, Jonas, S Pacilé, M Andrea Markus, M Wiart, G Vande Velde, G Tromba, and Christian Dullin (2018).
"X-ray-based 3D virtual histology—adding the next dimension to histological analysis". In: *Molecular Imaging and Biology* 20.5, pp. 732–741. (Cit. on p. 70).

Alturkistani, Hani A, Faris M Tashkandi, and Zuhair M Mohammedsaleh (2015).
"Histological stains: a literature review and case study". In: *Global journal of health science* 8.3, p. 72. (Cit. on p. 70).

Alvarez, Robert E and Albert Macovski (1976).
"Energy-selective reconstructions in x-ray computerised tomography". In: *Physics in Medicine & Biology* 21.5, p. 733. (Cit. on pp. 20, 45).

Bassey, B, M Martinson, N Samadi, G Belev, Cahit Karanfil, P Qi, and D Chapman (2016).
"Multiple energy synchrotron biomedical imaging system". In: *Physics in Medicine & Biology* 61.23, p. 8180. (Cit. on pp. 28, 33).

Bech, Martin, A Tapfer, A Velroyen, A Yaroshenko, B Pauwels, J Hostens, P Bruyndonckx, A Sasov, and F Pfeiffer (2013).
"In-vivo dark-field and phase-contrast x-ray imaging". In: *Scientific reports* 3.1, p. 3209. (Cit. on p. 110).

Behling, Rolf and Florian Grüner (2018).
"Diagnostic X-ray sources—present and future". In: *Nuclear Instruments and Methods in Physics Research Section A: Accelerators, Spectrometers, Detectors and Associated Equipment* 878, pp. 50–57. (Cit. on p. 14).

Beister, Marcel, Daniel Kolditz, and Willi A Kalender (2012).
"Iterative reconstruction methods in X-ray CT". In: *Physica medica* 28.2, pp. 94–108. (Cit. on p. 13).

Bellazzini, R, A Brez, G Spandre, M Minuti, M Pinchera, Pasquale Delogu, PL De Ruvo, and A Vincenzi (2015).
"PIXIE III: a very large area photon-counting CMOS pixel ASIC for sharp X-ray spectral imaging". In: *Journal of Instrumentation* 10.01, p. C01032. (Cit. on p. 52).

Bellazzini, R, Gloria Spandre, Alessan Brez, M Minuti, M Pinchera, and P Mozzo (2013).
"Chromatic X-ray imaging with a fine pitch CdTe sensor coupled to a large area photon counting pixel ASIC". In: *Journal of Instrumentation* 8.02, p. C02028. (Cit. on p. 118).

Berger, M.J., J.H. Hubbell, S.M. Seltzer, J. Chang, J.S. Coursey, R. Sukumar, D.S. Zucker, and Olsen K. (2010).
XCOM: Photon Cross Section Database (version 1.5). [Online]. Tech. rep. National Institute of Standards and Technology, Gaithersburg, MD. (Cit. on p. 23).

Berujon, Sebastien, Hongchang Wang, and Kawal Sawhney (2012).
"X-ray multimodal imaging using a random-phase object". In: *Physical Review A—Atomic, Molecular, and Optical Physics* 86.6, p. 063813. (Cit. on p. 37).

Bharti, Amardeep and Navdeep Goyal (2019).
"Fundamental of synchrotron radiations". In: *Synchrotron Radiation-Useful and Interesting Applications*. IntechOpen. (Cit. on p. 14).

Born, Max and Emil Wolf (2013).
Principles of optics: electromagnetic theory of propagation, interference and diffraction of light. Elsevier. (Cit. on p. 10).

Brahme, Anders (2014).
Comprehensive biomedical physics. Newnes. (Cit. on p. 12).

Brombal, Luca, Fulvia Arfelli, Francesco Brun, Vittorio Di Trapani, Marco Endrizzi, Ralf H Menk, Paola Perion, Luigi Rigon, Mara Saccomano, Giuliana Tromba, et al. (2024).
"Edge-illumination spectral phase-contrast tomography". In: *Physics in Medicine & Biology* 69.7, p. 075027. (Cit. on pp. 46, 56, 121).

Brombal, Luca, Fulvia Arfelli, Ralf Hendrik Menk, Luigi Rigon, and Francesco Brun (2023).
"Pepi lab: a flexible compact multi-modal setup for x-ray phase-contrast and spectral imaging". In: *Scientific Reports* 13.1, p. 4206. (Cit. on p. 51).

Brombal, Luca, Sandro Donato, Francesco Brun, Pasquale Delogu, Viviana Fanti, Piernicola Oliva, Luigi Rigon, Vittorio Di Trapani, Renata Longo, and Bruno Golosio (2018).
"Large-area single-photon-counting CdTe detector for synchrotron radiation computed tomography: a dedicated pre-processing procedure". In: *Synchrotron Radiation* 25.4, pp. 1068–1077. (Cit. on p. 120).

Brombal, Luca, L Rigon, F Arfelli, RH Menk, and F Brun (2022).
"A Geant4 tool for edge-illumination X-ray phase-contrast imaging". In: *Journal of Instrumentation* 17.01, p. C01043. (Cit. on p. 54).

Bushberg, Jerrold T, J Anthony Seibert, Edwin M Leidholdt, John M Boone, and LR Frank (1994).
"The essential physics of medical imaging". In: *AJR-American Journal of Roentgenology* 163.6, pp. 1338–1338. (Cit. on pp. 5, 6, 15).

Butler, Anthony PH, Jochen Butzer, Nanette Schleich, Nicholas J Cook, Nigel G Anderson, Nicola Scott, Niels de Ruiter, Raphael Grasset, Lukas Tlustos, and Philip H Butler (2011).
"Processing of spectral X-ray data with principal components analysis". In: *Nuclear Instruments and Methods in Physics Research Section A: Accelerators, Spectrometers, Detectors and Associated Equipment* 633, S140–S142. (Cit. on p. 24).

Camattari, Riccardo, Vincenzo Guidi, Valerio Bellucci, and Andrea Mazzolari (2015).
"Thequasi-mosaic'effect in crystals and its applications in modern physics". In: *Applied Crystallography* 48.4, pp. 977–989. (Cit. on p. 81).

Chapman, Dean, W Thomlinson, RE Johnston, D Washburn, E Pisano, N Gmür, Z Zhong, R Menk, Fulvia Arfelli, and D Sayers (1997).
"Diffraction enhanced x-ray imaging". In: *Physics in Medicine & Biology* 42.11, p. 2015. (Cit. on p. 37).

Chubar, Oleg and P Elleaume (1998).
"Accurate and efficient computation of synchrotron radiation in the near field region". In: *proc. of the EPAC98 Conference*. Vol. 1177. (Cit. on p. 80).

Chung, Hye Rim (2014).
"Iodine and thyroid function". In: *Annals of pediatric endocrinology & metabolism* 19.1, pp. 8–12. (Cit. on p. 70).

Clauser, JF and MW Reinsch (1992).
"New theoretical and experimental results in Fresnel optics with applications to matter-wave and X-ray interferometry". In: *Applied Physics B* 54.5, pp. 380–395. (Cit. on p. 37).

D'Avanzo, Alessandra, Patrick Treseler, Philip HG Ituarte, Mariwil Wong, Leanne Streja, Francis S Greenspan, Allan E Siperstein, Quan-Yang Duh, and Orlo H Clark (2004).
"Follicular thyroid carcinoma: histology and prognosis". In: *Cancer: Interdisciplinary International Journal of the American Cancer Society* 100.6, pp. 1123–1129. (Cit. on p. 70).

Delogu, Pasquale, P Oliva, R Bellazzini, A Brez, PL De Ruvo, M Minuti, M Pinchera, G Spandre, and A Vincenzi (2016).
"Characterization of Pixirad-1 photon counting detector for X-ray imaging". In: *Journal of Instrumentation* 11.01, P01015. (Cit. on p. 118).

Di Trapani, V, A Bravin, F Brun, D Dreossi, R Longo, A Mittone, L Rigon, and P Delogu (2020).
"Characterization of the acquisition modes implemented in Pixirad-1/Pixie-III X-ray Detector: Effects of charge sharing correction on spectral resolution and image quality". In: *Nuclear Instruments and Methods in Physics Research Section A: Accelerators, Spectrometers, Detectors and Associated Equipment* 955, p. 163220. (Cit. on p. 54).

Di Trapani, V, L Brombal, and F Brun (2022).
"Multi-material spectral photon-counting micro-CT with minimum residual decomposition and self-supervised deep denoising". In: *Optics Express* 30.24, pp. 42995–43011. (Cit. on pp. 24, 53).

Donath, Tilman, Dubravka Šišak Jung, Max Burian, Valeria Radicci, Pietro Zambon, Andrew N Fitch, Catherine Dejoie, Bingbing Zhang, Marie Ruat, Michael Hanfland, et al. (2023).
"EIGER2 hybrid-photon-counting X-ray detectors for advanced synchrotron diffraction experiments". In: *Synchrotron Radiation* 30.4, pp. 723–738. (Cit. on p. 59).

Donato, Sandro, LM Arana Peña, D Bonazza, V Formoso, R Longo, G Tromba, and L Brombal (2022).
"Optimization of pixel size and propagation distance in X-ray phase-contrast virtual histology". In: *Journal of Instrumentation* 17.05, p. C05021. (Cit. on p. 88).

Dubsky, Stephen (2021).
"Synchrotron-Based Dynamic Lung Imaging". In: *Molecular Imaging*. Elsevier, pp. 359–371. (Cit. on p. 16).

Elleaume, H, AM Charvet, S Corde, F Esteve, and JF Le Bas (2002).
"Performance of computed tomography for contrast agent concentration measurements with monochromatic x-ray beams: comparison of K-edge versus temporal subtraction". In: *Physics in Medicine & Biology* 47.18, p. 3369. (Cit. on p. 29).

Elleaume, H, S Fiedler, F Esteve, B Bertrand, AM Charvet, P Berkvens, G Berruyer, T Brochard, G Le Duc, C Nemoz, et al. (2000).
"First human transvenous coronary angiography at the European SynchrotronRadiation Facility". In: *Physics in Medicine & Biology* 45.9, p. L39. (Cit. on p. 29).

Endrizzi, Marco (2018).
"X-ray phase-contrast imaging". In: *Nuclear instruments and methods in physics research section A: Accelerators, spectrometers, detectors and associated equipment* 878, pp. 88–98. (Cit. on p. 3).

Esposito, Michela, Lorenzo Massimi, Ian Buchanan, Joseph D Ferrara, Marco Endrizzi, and Alessandro Olivo (2022).
"A laboratory-based, low-energy, multi-modal x-ray microscope with user-defined resolution". In: *Applied Physics Letters* 120.23. (Cit. on p. 43).

Excelitas Technologies Corp. (2019).
PCO edge. Accessed: October 24, 2025. (Visited on 10/24/2025) (cit. on p. 71).

Faby, Sebastian, Joscha Maier, David Simons, Heinz-Peter Schlemmer, Michael Lell, and Marc Kachelrieß (2015).
"A photon counting detector model based on increment matrices to simulate statistically correct detector signals". In: *Medical Imaging 2015: Physics of Medical Imaging*. Vol. 9412. SPIE, pp. 1219–1227. (Cit. on p. 27).

Fantoni, Simone, Francesco Brun, Paolo Cardarelli, Fabio Baruffaldi, Virginia Cristofori, Angelo Taibi, Claudio Trapella, and Luca Brombal (2024).
"Quantitative spectral micro-CT of a CA4+ loaded osteochondral sample with a tabletop system". In: *The European Physical Journal Plus* 139.8, p. 735. (Cit. on pp. 119, 124).

Flohr, Thomas G, Cynthia H McCollough, Herbert Bruder, Martin Petersilka, Klaus Gruber, Christoph Süβ, Michael Grasruck, Karl Stierstorfer, Bernhard Krauss, Rainer Raupach, et al. (2006).
"First performance evaluation of a dual-source CT (DSCT) system". In: *European radiology* 16, pp. 256–268. (Cit. on p. 20).

Fredenberg, Erik (2018).
"Spectral and dual-energy X-ray imaging for medical applications". In: *Nuclear Instruments and Methods in Physics Research Section A: Accelerators, Spectrometers, Detectors and Associated Equipment* 878, pp. 74–87. (Cit. on p. 20).

Frohn, Jasper, Diana Pinkert-Leetsch, Jeannine Missbach-Güntner, Marius Reichardt, Markus Osterhoff, Frauke Alves, and Tim Salditt (2020).
"3D virtual histology of human pancreatic tissue by multiscale phase-contrast X-ray tomography". In: *Synchrotron Radiation* 27.6, pp. 1707–1719. (Cit. on p. 70).

Fursey, GAJ (1975).
"A note on the density of bovine limb bones". In: *Animal Science* 21.2, pp. 195–198. (Cit. on p. 124).

Gänz, Peter, Steffen Kieß, and Sven Simon (2022).
"Single shot x-ray speckle tracking phase contrast imaging with a low brilliance lab source". In: *e-Journal of Nondestructive Testing Proceedings*. (Cit. on p. 58).

Goodman, Joseph W (2005).
Introduction to Fourier optics. Roberts and Company publishers. (Cit. on p. 88).

Graves, WS, J Bessuille, P Brown, S Carbajo, V Dolgashev, K-H Hong, E Ihloff, B Khaykovich, H Lin, Krishna Murari, et al. (2014).
"Compact x-ray source based on burst-mode inverse Compton scattering at 100 kHz". In: *Physical Review Special Topics-Accelerators and Beams* 17.12, p. 120701. (Cit. on p. 14).

Greaves, George Neville, A Lindsay Greer, Roderic S Lakes, and Tanguy Rouxel (2011).
"Poisson's ratio and modern materials". In: *Nature materials* 10.11, pp. 823–837. (Cit. on p. 35).

Gruner, Sol M, Mark W Tate, and Eric F Eikenberry (2002).
"Charge-coupled device area X-ray detectors". In: *Review of Scientific Instruments* 73.8, pp. 2815–2842. (Cit. on p. 92).

Gureyev, Timur E, S Mayo, SW Wilkins, D Paganin, and Andrew W Stevenson (2001).
"Quantitative in-line phase-contrast imaging with multienergy x rays". In: *Physical Review Letters* 86.25, p. 5827. (Cit. on p. 38).

Hainfeld, JF, DN Slatkin, TM Focella, and HM Smilowitz (2006).
"Gold nanoparticles: a new X-ray contrast agent". In: *The British journal of radiology* 79.939, pp. 248–253. (Cit. on p. 53).

Hallouard, François, Nicolas Anton, Philippe Choquet, André Constantinesco, and Thierry Vandamme (2010).
"Iodinated blood pool contrast media for preclinical X-ray imaging applications–a review". In: *Biomaterials* 31.24, pp. 6249–6268. (Cit. on p. 53).

Heitler, Walter (1984).
The quantum theory of radiation. Courier Corporation. (Cit. on p. 5).

Hemberg, Oscar, M Otendal, and HM Hertz (2003).
"Liquid-metal-jet anode electron-impact x-ray source". In: *Applied Physics Letters* 83.7, pp. 1483–1485. (Cit. on p. 14).

Hiriyannaiah, Harish P (1997).
"X-ray computed tomography for medical imaging". In: *IEEE signal Processing magazine* 14.2, pp. 42–59. (Cit. on p. 13).

Honkanen, Miitu KM, Annina EA Saukko, Mikael J Turunen, Rubina Shaikh, Mithilesh Prakash, Goran Lovric, Antti Joukainen, Heikki Kröger, Mark W Grinstaff, and Juha Töyräs (2020).
"Synchrotron microCT reveals the potential of the dual contrast technique for quantitative assessment of human articular cartilage composition". In: *Journal of Orthopaedic Research®* 38.3, pp. 563–573. (Cit. on p. 124).

Hounsfield, Godfrey N (1973).
"Computerized transverse axial scanning (tomography): Part 1. Description of system". In: *The British journal of radiology* 46.552, pp. 1016–1022. (Cit. on p. 3).

How, Ying Ying, David M Paganin, and Kaye S Morgan (2023).
"On the quantification of sample microstructure using single-exposure x-ray dark-field imaging via a single-grid setup". In: *Scientific Reports* 13.1, p. 11001. (Cit. on p. 9).

Inc., The MathWorks (2022).
MATLAB version: 9.13.0 (R2022b). Natick, Massachusetts, United States. (Cit. on p. 71).

Jacobson, Bertil (1953).
"Dichromatic absorption radiography. Dichromography". In: *Acta radiologica* 6, pp. 437–452. (Cit. on p. 20).

Ji, Xu, Ran Zhang, Ke Li, and Guang-Hong Chen (2020).
"Dual energy differential phase contrast CT (DE-DPC-CT) imaging". In: *IEEE transactions on medical imaging* 39.11, pp. 3278–3289. (Cit. on p. 45).

Kalender, Willi A, WH Perman, JR Vetter, and Ernst Klotz (1986).
"Evaluation of a prototype dual-energy computed tomographic apparatus. I. Phantom studies". In: *Medical physics* 13.3, pp. 334–339. (Cit. on p. 20).

Kharfi, Faycal (2013).
Imaging and Radioanalytical Techniques in Interdisciplinary Research: Fundamentals and Cutting Edge Applications. BoD–Books on Demand. (Cit. on p. 11).

Lee, Do Hyung, Young Hen Lee, Hyung Suk Seo, Ki Yeol Lee, Sang-il Suh, Inseon Ryoo, Sung-Hye You, Byungjun Kim, and Kyung-Sook Yang (2019).
"Dual-energy CT iodine quantification for characterizing focal thyroid lesions". In: *Head & neck* 41.4, pp. 1024–1031. (Cit. on p. 70).

Leng, Shuai, Maria Shiung, Songtao Ai, Mingliang Qu, Terri J Vrtiska, Katharine L Grant, Bernhard Krauss, Bernhard Schmidt, John C Lieske, and Cynthia H McCollough (2015).
"Feasibility of discriminating uric acid from non–uric acid renal stones using consecutive spatially registered low-and high-energy scans obtained on a conventional CT scanner". In: *American Journal of Roentgenology* 204.1, pp. 92–97. (Cit. on p. 20).

Lewis, R (1997).
"Medical applications of synchrotron radiation x-rays". In: *Physics in medicine & biology* 42.7, p. 1213. (Cit. on p. 16).

Lioliou, G, C Navarrete-León, A Astolfo, S Savvidis, D Bate, M Endrizzi, CK Hagen, and A Olivo (2023).
"A laboratory-based beam tracking x-ray imaging method achieving two-dimensional phase sensitivity and isotropic resolution with unidirectional undersampling". In: *Scientific Reports* 13.1, p. 8707. (Cit. on p. 43).

Longo, Elena, Adriano Contillo, Lorenzo D'Amico, Marko Prašek, Giulia Saccomano, Nicola Sodini, Christian Dullin, Diego Dreossi, and Giuliana Tromba (2024).
"SYRMEP beamline: state of the art, upgrades and future prospects". In: *The European Physical Journal Plus* 139.10, p. 880. (Cit. on pp. 94, 117).

Lusic, Hrvoje and Mark W Grinstaff (2013).
"X-ray-computed tomography contrast agents". In: *Chemical reviews* 113.3, pp. 1641–1666. (Cit. on p. 109).

Magnin, Clara, Laurene Quenot, Dan Mihai Cenda, Blandine Lantz, Bertrand Faure, and Emmanuel Brun (2025).
"On the optimisation of the geometric pattern for structured illumination based X-ray phase contrast and dark field imaging: A simulation study and its experimental validation". In: *arXiv preprint arXiv:2504.10665*. (Cit. on pp. 39, 58, 63).

Martinson, Mercedes, Nazanin Samadi, Bassey Bassey, Ariel Gomez, and Dean Chapman (2015).
"Phase-preserving beam expander for biomedical X-ray imaging". In: *Synchrotron Radiation* 22.3, pp. 801–806. (Cit. on p. 29).

Massimi, Lorenzo, Ian Buchanan, Alberto Astolfo, Marco Endrizzi, and Alessandro Olivo (2020).
"Fast, non-iterative algorithm for quantitative integration of X-ray differential phase-contrast images". In: *Optics Express* 28.26, pp. 39677–39687. (Cit. on p. 120).

Mayo, Sheridan C, Peter Robert Miller, SW Wilkins, Timothy J Davis, D Gao, Timur Eugenievich Gureyev, David Paganin, DJ Parry, A Pogany, and Andrew W Stevenson (2002).
"Quantitative X-ray projection microscopy: phase-contrast and multi-spectral imaging". In: *Journal of microscopy* 207.2, pp. 79–96. (Cit. on p. 16).

Mayo, Sheridan and Marco Endrizzi (2019).
"X-ray phase contrast methods". In: *Handbook of Advanced Nondestructive Evaluation*. Springer, pp. 1053–1093. (Cit. on p. 8).

Mechlem, Korbinian, Thorsten Sellerer, Manuel Viermetz, Julia Herzen, and Franz Pfeiffer (2019).
"Spectral differential phase contrast x-ray radiography". In: *IEEE transactions on medical imaging* 39.3, pp. 578–587. (Cit. on p. 45).

Menk, Ralf Hendrik, Elisabeth Schültke, Christopher Hall, Fulvia Arfelli, Alberto Astolfo, Luigi Rigon, Adam Round, Khalid Ataelmannan, Sarah Rigley MacDonald, and Bernhard HJ Juurlink (2011). "Gold nanoparticle labeling of cells is a sensitive method to investigate cell distribution and migration in animal models of human disease". In: *Nanomedicine: Nanotechnology, Biology and Medicine* 7.5, pp. 647–654. (Cit. on p. 53).

Modregger, Peter, Daniel Lübbert, Peter Schäfer, and Rolf Köhler (2007). "Spatial resolution in Bragg-magnified X-ray images as determined by Fourier analysis". In: *physica status solidi (a)* 204.8, pp. 2746–2752. (Cit. on p. 63).

Morgan, Kaye S and David M Paganin (2019). "Applying the Fokker–Planck equation to grating-based x-ray phase and dark-field imaging". In: *Scientific reports* 9.1, p. 17465. (Cit. on pp. 41, 61).

Morgan, Kaye S, David M Paganin, and Karen KW Siu (2012). "X-ray phase imaging with a paper analyzer". In: *Applied Physics Letters* 100.12. (Cit. on pp. 37, 39, 58).

Nardroff, Robert von (1926). "Refraction of x-rays by small particles". In: *Physical Review* 28.2, p. 240. (Cit. on p. 9).

Navarrete-León, Carlos, Adam Doherty, Alberto Astolfo, Charlotte K Hagen, Peter Munro, Alessandro Olivo, and Marco Endrizzi (2023). "Two-directional beam-tracking for phase-sensitive X-ray tomography with laboratory sources". In: *AIP Conference Proceedings*. Vol. 2990. 1. AIP Publishing LLC, p. 050001. (Cit. on p. 58).

Nicolas, Christophe and Catalin Miron (2012). "Lifetime broadening of core-excited and-ionized states". In: *Journal of Electron Spectroscopy and Related Phenomena* 185.8-9, pp. 267–272. (Cit. on p. 77).

Nugent, KA, TE Gureyev, DF Cookson, D Paganin, and ZNMN Barnea (1996). "Quantitative phase imaging using hard x rays". In: *Physical review letters* 77.14, p. 2961. (Cit. on p. 38).

O'Shea, Patrick G and Henry P Freund (2001). "Free-electron lasers: Status and applications". In: *Science* 292.5523, pp. 1853–1858. (Cit. on p. 14).

Olivo, Alessandro and Robert Speller (2007). "A coded-aperture technique allowing x-ray phase contrast imaging with conventional sources". In: *Applied Physics Letters* 91.7. (Cit. on p. 37).

Ou, Xiangyu, Xue Chen, Xianning Xu, Lili Xie, Xiaofeng Chen, Zhongzhu Hong, Hua Bai, Xiaowang Liu, Qiushui Chen, Lin Li, et al. (2021). "Recent development in x-ray imaging technology: Future and challenges". In: *Research*. (Cit. on p. 16).

Paganin, DM and KS Morgan (2019). *X-ray Fokker–Planck equation for paraxial imaging Sci*. (Cit. on pp. 41, 62).

Paganin, David (2006). *Coherent X-ray optics*. 6. Oxford University Press. (Cit. on p. 16).

Paganin, David, Sheridan C Mayo, Tim E Gureyev, Peter R Miller, and Steve W Wilkins (2002). "Simultaneous phase and amplitude extraction from a single defocused image of a homogeneous object". In: *Journal of microscopy* 206.1, pp. 33–40. (Cit. on p. 38).

Panahifar, Arash, Nazanin Samadi, Treena M Swanston, L Dean Chapman, and David ML Cooper (2016).
"Spectral K-edge subtraction imaging of experimental non-radioactive barium uptake in bone". In: *Physica medica* 32.12, pp. 1765–1770. (Cit. on p. 20).

Panta, Raj Kumar, Stephen T Bell, JL Healy, Raja Aamir, Chrstopher J Bateman, Mahdieh Moghiseh, APH Butler, and NG Anderson (2018).
"Element-specific spectral imaging of multiple contrast agents: a phantom study". In: *Journal of Instrumentation* 13.02, T02001. (Cit. on p. 20).

Pavlov, Konstantin M, Heyang Li, David M Paganin, Sebastien Berujon, Hélène Rougé-Labriet, and Emmanuel Brun (2020).
"Single-shot x-ray speckle-based imaging of a single-material object". In: *Physical Review Applied* 13.5, p. 054023. (Cit. on p. 58).

Perion, P, F Arfelli, Ralf Hendrik Menk, and L Brombal (2024a).
"Spectral micro-CT for simultaneous gold and iodine detection, and multi-material identification". In: *Journal of Instrumentation* 19.04, p. C04023. (Cit. on pp. 51, 52).

Perion, P, L Brombal, F Brun, L Sbuelz, S Donato, RH Menk, and F Arfelli (2025a).
"Spectral phase-contrast X-ray imaging with high-resolution detectors". In: *Journal of Instrumentation* 20.06, p. C06056. (Cit. on p. 86).

Perion, P, L Brombal, P Delogu, V di Trapani, P Oliva, and F Arfelli (2024b).
"A high sensitivity wide bandwidth spectral system for multiple K-edge imaging". In: *Journal of Physics D: Applied Physics* 57.35, p. 355402. (Cit. on pp. 19, 33).

Perion, Paola, Luca Brombal, Paolo Cardarelli, Sandro Donato, Simone Fantoni, Ralf Hendrik Menk, Luca Sbuelz, and Fulvia Arfelli (2025b).
"A Dual-Detector X-ray -CT System for simultaneous Spectral and Phase contrast Imaging". In: *Applied Physics Letters* 127. (Cit. on p. 116).

Pfeiffer, Franz, Timm Weitkamp, Oliver Bunk, and Christian David (2006).
"Phase retrieval and differential phase-contrast imaging with low-brilliance X-ray sources". In: *Nature physics* 2.4, pp. 258–261. (Cit. on p. 37).

Physik Instrumente (2025a).
High-Precision Hexapods. Accessed: October 24, 2025. (Visited on 10/24/2025) (cit. on p. 96).

— (2025b).
L-511 High Precision Linear Stage. Accessed: October 24, 2025. (Visited on 10/24/2025) (cit. on p. 95).

— (2025c).
L-836 Linear Stage. Accessed: October 24, 2025. (Visited on 10/24/2025) (cit. on p. 97).

Qi, Peng, Xianbo Shi, Nazanin Samadi, and Dean Chapman (2019).
"Focusing and energy dispersion properties of a cylindrically bent asymmetric Laue crystal". In: *Advances in X-Ray/EUV Optics and Components XIV*. Vol. 11108. SPIE, pp. 30–38. (Cit. on p. 29).

— (2021).
"Bent Laue crystal anatomy: new insights into focusing and energy-dispersion properties". In: *Applied Crystallography* 54.2, pp. 409–426. (Cit. on pp. 29, 32, 34, 77, 133).

Quénot, Laurène, Hélène Rougé-Labriet, Sylvain Bohic, Sebastien Berujon, and Emmanuel Brun (2021).
"Implicit tracking approach for X-ray phase-contrast imaging with a random mask and a conventional system". In: *Optica* 8.11, pp. 1412–1415. (Cit. on pp. 41, 61).

Radon, Johann (2005).
"1.1 über die bestimmung von funktionen durch ihre integralwerte längs gewisser mannigfaltigkeiten". In: *Classic papers in modern diagnostic radiology* 5.21, p. 124. (Cit. on p. 12).

Rajendran, Kishore, Martin Petersilka, André Henning, Elisabeth R Shanblatt, Bernhard Schmidt, Thomas G Flohr, Andrea Ferrero, Francis Baffour, Felix E Diehn, Lifeng Yu, et al. (2022).
"First clinical photon-counting detector CT system: technical evaluation". In: *Radiology* 303.1, pp. 130–138. (Cit. on p. 20).

Rebuffi, Luca and Manuel Sanchez del Rio (2017).
"OASYS (OrAnge SYnchrotron Suite): an open-source graphical environment for x-ray virtual experiments". In: *Advances in Computational Methods for X-Ray Optics IV*. Vol. 10388. SPIE, pp. 169–177. (Cit. on p. 80).

Rio, Manuel Sanchez del, Niccolo Canestrari, Fan Jiang, and Franco Cerrina (2011).
"SHADOW3: a new version of the synchrotron X-ray optics modelling package". In: *Synchrotron Radiation* 18.5, pp. 708–716. (Cit. on p. 80).

Roessl, E and R Proksa (2007).
"K-edge imaging in x-ray computed tomography using multi-bin photon counting detectors". In: *Physics in Medicine & Biology* 52.15, p. 4679. (Cit. on p. 53).

Röntgen, Wilhelm Conrad (1896a).
Eine neue Art von Strahlen: II. Mittheilung. 2. Vol. 2. Stahel. (Cit. on p. 3).

— (1896b).
"On a new kind of rays". In: *Science* 3.59, pp. 227–231. (Cit. on p. 3).

Russo, Paolo (2017).
Handbook of X-ray imaging: physics and technology. CRC press. (Cit. on p. 13).

Samadi, Nazanin, Mercedes Martinson, Bassey Bassey, Ariel Gomez, George Belev, and Dean Chapman (2016).
"An energy dispersive bent Laue monochromator for K-edge subtraction imaging". In: *AIP Conference Proceedings*. Vol. 1741. 1. AIP Publishing. (Cit. on pp. 29, 34, 35).

Savatović, Sara, Davis Laundon, Fabio De Marco, Mirko Riedel, Jörg U Hammel, Madleen Busse, Murielle Salomé, Lorella Pascolo, Irene Zanette, Rohan M Lewis, et al. (2025).
"High-resolution X-ray phase-contrast tomography of human placenta with different wavefront markers". In: *Scientific reports* 15.1, p. 2131. (Cit. on p. 58).

Schaff, Florian, Kaye S Morgan, James A Pollock, Linda CP Croton, Stuart B Hooper, and Marcus J Kitchen (2020).
"Material decomposition using spectral propagation-based phase-contrast x-ray imaging". In: *IEEE Transactions on Medical Imaging* 39.12, pp. 3891–3899. (Cit. on p. 45).

Schneider, Caroline A, Wayne S Rasband, and Kevin W Eliceiri (2012).
"NIH Image to ImageJ: 25 years of image analysis". In: *Nature methods* 9.7, pp. 671–675. (Cit. on p. 120).

Scott, Anna E, Dragos M Vasilescu, Katherine AD Seal, Samuel D Keyes, Mark N Mavrogordato, James C Hogg, Ian Sinclair, Jane A Warner, Tillie-Louise Hackett, and Peter M Lackie (2015).
"Three dimensional imaging of paraffin embedded human lung tissue samples by micro-computed tomography". In: *PloS one* 10.6, e0126230. (Cit. on p. 70).

Sedigh Rahimabadi, Pooria, Mehdi Khodaei, and Kaveenga R Koswattage (2020).
"Review on applications of synchrotron-based X-ray techniques in materials characterization". In: *X-Ray Spectrometry* 49.3, pp. 348–373. (Cit. on p. 16).

Snigirev, Anatoly, Irina Snigireva, V Kohn, S Kuznetsov, and I Schelokov (1995). "On the possibilities of x-ray phase contrast microimaging by coherent high-energy synchrotron radiation". In: *Review of scientific instruments* 66.12, pp. 5486–5492. (Cit. on p. 37).

Sorrenti, Salvatore, Enke Baldini, Daniele Pironi, Augusto Lauro, Valerio D'Orazi, Francesco Tartaglia, Domenico Tripodi, Eleonora Lori, Federica Gagliardi, Marianna Praticò, et al. (2021). "Iodine: Its role in thyroid hormone biosynthesis and beyond". In: *Nutrients* 13.12, p. 4469. (Cit. on p. 70).

Sousa, Fernanda, Subhra Mandal, Chiara Garrovo, Alberto Astolfo, Alois Bonifacio, Diane Latawiec, Ralf Hendrik Menk, Fulvia Arfelli, Sabine Huewel, Giuseppe Legname, et al. (2010). "Functionalized gold nanoparticles: a detailed in vivo multimodal microscopic brain distribution study". In: *Nanoscale* 2.12, pp. 2826–2834. (Cit. on p. 53).

Stewart, Rachel C, Amit N Patwa, Hrvoje Lusic, Jonathan D Freedman, Michel Wathier, Brian D Snyder, Ali Guermazi, and Mark W Grinstaff (2017). "Synthesis and preclinical characterization of a cationic iodinated imaging contrast agent (CA4+) and its use for quantitative computed tomography of ex vivo human hip cartilage". In: *Journal of medicinal chemistry* 60.13, pp. 5543–5555. (Cit. on p. 119).

Taguchi, Katsuyuki and Jan S Iwanczyk (2013). "Vision 20/20: single photon counting x-ray detectors in medical imaging". In: *Medical physics* 40.10, p. 100901. (Cit. on p. 20).

Teague, Michael Reed (1983). "Deterministic phase retrieval: a Green's function solution". In: *Journal of the Optical Society of America* 73.11, pp. 1434–1441. (Cit. on p. 41).

Thomlinson, William, Helene Elleaume, Liisa Porra, and P Suortti (2018). "K-edge subtraction synchrotron X-ray imaging in bio-medical research". In: *Physica Medica* 49, pp. 58–76. (Cit. on p. 20).

Thorlabs (2025). *300 mm Linear Translation Stage*. Accessed: October 24, 2025. (Visited on 10/24/2025) (cit. on p. 97).

Töpperwien, Mareike, Martin Krenkel, Daniel Vincenz, Franziska Stöber, Anja M Oelschlegel, Jürgen Goldschmidt, and Tim Salditt (2017). "Three-dimensional mouse brain cytoarchitecture revealed by laboratory-based x-ray phase-contrast tomography". In: *Scientific reports* 7.1, p. 42847. (Cit. on p. 70).

Tromba, G, R Longo, A Abrami, F Arfelli, A Astolfo, P Bregant, F Brun, K Casarin, V Chenda, D Dreossi, et al. (2010). "The SYRMEP Beamline of Elettra: clinical mammography and bio-medical applications". In: *AIP Conference Proceedings*. Vol. 1266. 1. American Institute of Physics, pp. 18–23. (Cit. on p. 94).

Van Aarle, Wim, Willem Jan Palenstijn, Jeroen Cant, Eline Janssens, Folkert Bleichrodt, Andrei Dabravolski, Jan De Beenhouwer, K Joost Batenburg, and Jan Sijbers (2016). "Fast and flexible X-ray tomography using the ASTRA toolbox". In: *Optics express* 24.22, pp. 25129–25147. (Cit. on p. 57).

Vittoria, Fabio A, Marco Endrizzi, Paul C Diemoz, Anna Zamir, Ulrich H Wagner, Christoph Rau, Ian K Robinson, and Alessandro Olivo (2015a). "X–ray absorption, phase and dark–field tomography through a beam tracking approach". In: *Scientific reports* 5.1, p. 16318. (Cit. on p. 42).

Vittoria, Fabio A, Gibril KN Kallon, Dario Basta, Paul C Diemoz, Ian K Robinson, Alessandro Olivo, and Marco Endrizzi (2015b).
"Beam tracking approach for single–shot retrieval of absorption, refraction, and dark–field signals with laboratory x–ray sources". In: *Applied Physics Letters* 106.22. (Cit. on pp. 37, 119).

Vries, Anke de, Ewald Roessl, Esther Kneepkens, Axel Thran, Bernhard Brendel, Gerhard Martens, Roland Proska, Klaas Nicolay, and Holger Grüll (2015).
"Quantitative spectral K-edge imaging in preclinical photon-counting x-ray computed tomography". In: *Investigative radiology* 50.4, pp. 297–304. (Cit. on p. 20).

Wen, Harold H, Eric E Bennett, Rael Kopace, Ashley F Stein, and Vinay Pai (2010).
"Single-shot x-ray differential phase-contrast and diffraction imaging using two-dimensional transmission gratings". In: *Optics letters* 35.12, pp. 1932–1934. (Cit. on p. 37).

Wilkins, SW, T Ei Gureyev, D Gao, A Pogany, and AW Stevenson (1996).
"Phase-contrast imaging using polychromatic hard X-rays". In: *Nature* 384.6607, pp. 335–338. (Cit. on pp. 9, 37, 38).

Wilkins, SW, Ya I Nesterets, TE Gureyev, SC Mayo, A Pogany, and AW Stevenson (2014).
"On the evolution and relative merits of hard X-ray phase-contrast imaging methods". In: *Philosophical Transactions of the Royal Society A: Mathematical, Physical and Engineering Sciences* 372.2010, p. 20130021. (Cit. on p. 3).

Willemink, Martin J, Mats Persson, Amir Pourmorteza, Norbert J Pelc, and Dominik Fleischmann (2018).
"Photon-counting CT: technical principles and clinical prospects". In: *Radiology* 289.2, pp. 293–312. (Cit. on p. 92).

Willer, Konstantin, Alexander A Fingerle, Lukas B Gromann, Fabio De Marco, Julia Herzen, Klaus Achterhold, Bernhard Gleich, Daniela Muenzel, Kai Scherer, Martin Renz, et al. (2018).
"X-ray dark-field imaging of the human lung—A feasibility study on a deceased body". In: *PloS one* 13.9, e0204565. (Cit. on p. 110).

Willmott, Philip (2019).
An introduction to synchrotron radiation: techniques and applications. John Wiley & Sons. (Cit. on p. 14).

Xie, Bingqing, Ting Su, Valérie Kaftandjian, Pei Niu, Feng Yang, Marc Robini, Yuemin Zhu, and Philippe Duvauchelle (2019).
"Material decomposition in X-ray spectral CT using multiple constraints in image domain". In: *Journal of Nondestructive Evaluation* 38, pp. 1–9. (Cit. on p. 24).

Zaber (2025a).
Goniometer Stage. Accessed: October 24, 2025. (Visited on 10/24/2025) (cit. on p. 97).

— (2025b).
Rotary Stage. Accessed: October 24, 2025. (Visited on 10/24/2025) (cit. on p. 97).

Zanette, Irene, Tunhe Zhou, Anna Burvall, Ulf Lundström, Daniel H Larsson, M Zdora, P Thibault, Franz Pfeiffer, and Hans M Hertz (2014).
"Speckle-based x-ray phase-contrast and dark-field imaging with a laboratory source". In: *Physical review letters* 112.25, p. 253903. (Cit. on pp. 40, 41).

Zdora, Marie-Christine (2018).
"State of the art of X-ray speckle-based phase-contrast and dark-field imaging". In: *Journal of Imaging* 4.5, p. 60. (Cit. on pp. 39, 40, 58, 86).

Zdora, Marie-Christine, Pierre Thibault, Tunhe Zhou, Frieder J Koch, Jenny Romell, Simone Sala, Arndt Last, Christoph Rau, and Irene Zanette (2017). "X-ray phase-contrast imaging and metrology through unified modulated pattern analysis". In: *Physical review letters* 118.20, p. 203903. (Cit. on p. 41).

Zhu, Ying, N Samadi, M Martinson, B Bassey, Z Wei, G Belev, and D Chapman (2014). "Spectral K-edge subtraction imaging". In: *Physics in Medicine & Biology* 59.10, p. 2485. (Cit. on pp. 21, 33, 75).

Ziegler, E, J Hoszowska, T Bigault, L Peverini, JY Massonnat, and R Hustache (2004). "The ESRF BM05 metrology beamline: Instrumentation and performance upgrade". In: *AIP Conference Proceedings*. Vol. 705. 1. American Institute of Physics, pp. 436–439. (Cit. on p. 71).